Benchmark for Neutronic Analysis of Sodium-cooled Fast Reactor Cores with Various Fuel Types and Core Sizes

OECD

BETTER POLICIES FOR BETTER LIVES

NEA

NUCLEAR ENERGY AGENCY

Organisation de Coopération et de Développement Économiques
Organisation for Economic Co-operation and Development

25-Feb-2016
_____

English - Or. English

OECD Nuclear Energy Agency
Steering Committee for Nuclear Energy

Nuclear Science Committee

Benchmark for Neutronic Analysis of Sodium-cooled Fast Reactor Cores with Various Fuel Types and Core Sizes

This document exists only in pdf.

yukio.nakahara@oecd.org

JT03390630

Benchmark for Neutronic Analysis of Sodium-cooled Fast Reactor Cores with Various Fuel Types and Core Sizes

ORGANISATION FOR ECONOMIC CO-OPERATION AND DEVELOPMENT

The OECD is a unique forum where the governments of 34 democracies work together to address the economic, social and environmental challenges of globalisation. The OECD is also at the forefront of efforts to understand and to help governments respond to new developments and concerns, such as corporate governance, the information economy and the challenges of an ageing population. The Organisation provides a setting where governments can compare policy experiences, seek answers to common problems, identify good practice and work to co-ordinate domestic and international policies.

The OECD member countries are: Australia, Austria, Belgium, Canada, Chile, the Czech Republic, Denmark, Estonia, Finland, France, Germany, Greece, Hungary, Iceland, Ireland, Israel, Italy, Japan, Korea, Luxembourg, Mexico, the Netherlands, New Zealand, Norway, Poland, Portugal, the Slovak Republic, Slovenia, Spain, Sweden, Switzerland, Turkey, the United Kingdom and the United States. The European Commission takes part in the work of the OECD.

OECD Publishing disseminates widely the results of the Organisation's statistics gathering and research on economic, social and environmental issues, as well as the conventions, guidelines and standards agreed by its members.

NUCLEAR ENERGY AGENCY

The OECD Nuclear Energy Agency (NEA) was established on 1 February 1958. Current NEA membership consists of 31 countries: Australia, Austria, Belgium, Canada, the Czech Republic, Denmark, Finland, France, Germany, Greece, Hungary, Iceland, Ireland, Italy, Japan, Korea, Luxembourg, Mexico, the Netherlands, Norway, Poland, Portugal, Russia, the Slovak Republic, Slovenia, Spain, Sweden, Switzerland, Turkey, the United Kingdom and the United States. The European Commission also takes part in the work of the Agency.

The mission of the NEA is:

– to assist its member countries in maintaining and further developing, through international co-operation, the scientific, technological and legal bases required for a safe, environmentally friendly and economical use of nuclear energy for peaceful purposes;

– to provide authoritative assessments and to forge common understandings on key issues, as input to government decisions on nuclear energy policy and to broader OECD policy analyses in areas such as energy and sustainable development.

Specific areas of competence of the NEA include the safety and regulation of nuclear activities, radioactive waste management, radiological protection, nuclear science, economic and technical analyses of the nuclear fuel cycle, nuclear law and liability, and public information.

The NEA Data Bank provides nuclear data and computer program services for participating countries. In these and related tasks, the NEA works in close collaboration with the International Atomic Energy Agency in Vienna, with which it has a Co-operation Agreement, as well as with other international organisations in the nuclear field.

This document and any map included herein are without prejudice to the status of or sovereignty over any territory, to the delimitation of international frontiers and boundaries and to the name of any territory, city or area.

Corrigenda to OECD publications may be found online at: *www.oecd.org/publishing/corrigenda*.
© OECD 2016

Foreword

There is a strong incentive to design reactors with improved safety performance while preserving a sustainable source of energy at a rather low cost. The Generation IV International Forum (GIF) has defined the following key research goals for advanced Sodium-cooled Fast Reactors (SFR):

- improved safety performance, specifically, a demonstration of favourable transient behaviour under accident conditions;

- improved economic competitiveness;

- demonstration of flexible management of nuclear materials, in particular, waste reduction through minor actinide burning.

Sodium fast reactors offer the most promising type of reactors to achieve such Generation IV goals at a reasonable time scale given the experience accumulated over the years. However, it is recognised that new regulations and safety rules as they exist worldwide are requiring improved safety performance. In particular, one of the foremost GIF objectives is to design cores that can passively avoid core damage when the control rods fail to scram in response to postulated accident initiators (e.g. inadvertent reactivity insertion or loss of coolant flow). The analysis of such unprotected transients depends primarily on the physical properties of the fuel and the reactivity feedback coefficients of the core. Under the auspices of the Working Party on Scientific Issues of Reactor Systems (WPRS), an Expert Group Task Force was formed to investigate Sodium Fast Reactor core Feed-back and Transient response (SFR-FT) in order to identify recent progress in this field. The work was focused on a shared analysis of the feedback and transient behaviour of the next generation SFR concepts.

In order to achieve these goals, it was decided to start with a series of benchmarks on which the different participants could compare their abilities to calculate the nominal performance characteristics and the global safety parameters. The work concentrated on two different core sizes: two large size cores (3600 MW thermal) and two medium size cores (1000 MW thermal) and three types of fuel: oxide, carbide and metal. The "expert group" provided initial core descriptions for both size cores [1] in September 2011. The comparative study concentrated on the following items:

- neutronic characterisation of global parameters (k-effective, power and flux distributions, sodium void effect, Doppler, etc.);

- feedback coefficient evaluation, discussion and agreement on corresponding calculation methodology.

The present report summarises the results obtained by the WPRS for the benchmark exercise.

Eleven (11) organisations contributed to this benchmark: Argonne National Laboratory (ANL), Commissariat à l'énergie atomique et aux énergies alternatives (CEA of Cadarache), Commissariat à l'énergie atomique et aux énergies alternatives (CEA of Saclay), Centre for Energy Research (CER-EK), Italian National Agency for New Technologies, Energy and Sustainable Economic

3

Development (ENEA), Helmholtz Zentrum Dresden Rossendorf (HZDR), Institute of Nuclear Technology and Energy Systems (IKE), Japan Atomic Energy Agency (JAEA), Karlsruhe Institute of Technology (KIT), Centre d'Étude de l'énergie Nucléaire (SCK•CEN), and University of Illinois (UIUC). The contributors applied different calculation methodologies with deterministic or stochastic neutronic codes, different nuclear evaluation neutron data library files and different assumptions for the fuel and control rod assembly modelling. For the four SFR cores, the neutronic parameters such as the k-effective, beta effective, Doppler coefficient, sodium void worth, control rods worth, the power map and the isotopic content were obtained at the beginning and end of the equilibrium cycle.

The use of different methodologies, evaluation neutron data library files, computation codes, and applied approximations lead to a wide spread of numerical results which deserved to be explained. Hence, the main work has focused on the analysis of these apparent discrepancies.

In this report, differences in the results obtained from participants using various methodologies and tools were systematically analysed and the origins of the discrepancies were identified. Differences in the evaluation neutron data library files employed explain a large part - between 500 and 1 200 pcm – of the discrepancy obtained on the k-effective. The remaining part of the differences is explained by the homogeneous assumption used to model the fuel and control rod subassemblies, by the different computation methodologies, treatment of fission products, and the neutron energy group structure employed by the participants.

Some remaining inconsistencies with the results of some participants could not be investigated within the framework of this benchmark and still need to be understood. Discrepancies between "best estimate" deterministic and Monte-Carlo results need to be investigated in depth in order to identify remaining bias. Beyond this important task, the detailed review of modelling effects performed in this report paved the way for important recommendations on general neutronic schemes that need to be adopted for accurate reactivity effect evaluation for sodium-cooled fast reactors using deterministic codes:

- heterogeneous spatial description of subassembly for cross-section generation;

- fine group (few thousand group) energy description for self-shielding effects;

- specific treatment in order to take into account spatial self-shielding effect on control rod cross-section.

Despite apparent discrepancies explained in this report, calculated feedback coefficients and kinetic constants for performing transient analyses yielded satisfactory agreement for the four investigated SFR cores and limited bias on transient studies is anticipated.

Work has not yet started on transient behaviours under accident conditions, as this report is only the first step in a rather long series of studies. Recently, the International Atomic Energy Agency (IAEA) produced guidance on the use of deterministic safety analysis (DSA) for the design and licensing of nuclear power plants (NPPs): *Deterministic Safety Analysis for Nuclear Power Plants Specific Safety Guide*. Since the early days of civil nuclear power, the conservative approach has been used and is still widely used today. However, the desire to utilise current understanding of important phenomena and to maximise the economic potential of NPPs without compromising their safety has led many countries to use best-estimate codes and data together with an evaluation of the uncertainties.

The additional series of studies to be conducted in addition to what has already been achieved within the SFR-FT Expert Group will be performed in a SFR section of the Uncertainty Analysis in Modeling (UAM) activities of the WPRS and will cover the following items:

- Based on the results obtained in the previous step, transient calculations will be performed on a few selected cases for the principal unprotected transients unprotected transient overpower (UTOP), unprotected loss of flow (ULOF), unprotected loss of heat sink (ULOHS) and the core behaviours characterised using a matrix classification. The work should provide insights into the ability of these cores to withstand unprotected transients.

- The final report should make recommendations to improve safety taking into account the "state of the art" of past and recent studies performed for sodium-cooled fast reactors. This work will incorporate various parameters such as minor actinide management or fuel types (oxide, carbide, nitride and metal) and will be built on bibliography that would focus on core transient behaviours.

Acknowledgements

Table of contents

List of figures

List of tables

1. Introduction

One of the foremost Generation IV International Forum (GIF) objectives is to design nuclear reactor cores that can passively avoid damage of the reactor when control rods fail to scram in response to postulated accident initiators (e.g. inadvertent reactivity insertion or loss of coolant flow). The analysis of such unprotected transients depends primarily on the physical properties of the fuel and the reactivity feedback coefficients of the core. Within the activities of the Working Party on Scientific Issues of Reactor Systems (WPRS), the Sodium Fast Reactor core Feed-back and Transient response (SFR-FT) Task Force was proposed [1] to evaluate core performance characteristics of several Generation IV Sodium-cooled Fast Reactor (SFR) concepts.

A set of four numerical benchmark cases was initially developed with different core sizes and fuel types in order to perform neutronic characterisation, evaluation of the feedback coefficients and transient calculations. Two "large" SFR core designs were proposed by CEA: those generate 3 600 MW(th) and employ oxide and carbide fuel technologies. Two "medium" SFR core designs proposed by ANL complete the set. These medium SFR cores generate 1 000 MW(th) and employ oxide and metallic fuel technologies.

The present report summarises the results obtained by the WPRS for the neutronic characterisation benchmark exercise proposed. The benchmark definition is detailed in Chapter 2. Eleven institutions contributed to this benchmark: Argonne National Laboratory (ANL), Commissariat à l'énergie atomique et aux énergies alternatives (CEA of Cadarache), Commissariat à l'énergie atomique et aux énergies alternatives (CEA of Saclay), Centre for Energy Research (CER-EK), Italian National Agency for New Technologies, Energy and Sustainable Economic Development (ENEA), Helmholtz Zentrum Dresden Rossendorf (HZDR), Institute of Nuclear Technology and Energy Systems (IKE), Japan Atomic Energy Agency (JAEA), Karlsruhe Institute of Technology (KIT), Centre d'Étude de l'énergie Nucléaire (SCK•CEN), and University of Illinois (UIUC). The contributors applied different calculation methodologies as described in Chapter 3. For the four SFR cores modelled, the neutronics parameters such as the k-effective, beta effective, Doppler coefficient, sodium void worth, control rods worth, power map and isotopic content were obtained at the beginning and end of the equilibrium cycle. The results obtained by the various institutions are summarised in Chapter 4. The variations in the results obtained are analysed in Chapter 5 in order to understand the origin of differences and derive adequate recommendations. Finally, the conclusions of the study are provided in Chapter 6.

2. Benchmark definition

L. Buiron, D. Blanchet, T.K. Kim, N.E. Stauff, T.A. Taiwo

Four SFR benchmark core concepts were proposed in the WPRS SFR Task Force: Two large size cores by CEA generating a thermal power of 3600 MW(th) and two medium size cores by ANL generating a thermal power of 1000 MW(th). The detailed descriptions of the cores were described in [1] and reported in this chapter.

2.1 Cores description

2.1.1 Large size cores

For the large core, two 3600 MWth concepts have been provided by CEA [2,3]. Both are based on medium power density that leads to low reactivity swing during the operation cycle. Both concepts employ Oxide Strengthened Steel (ODS) cladding with helium bond.

The oxide core (MOX-3600) is based on the "fat pin with small wire" concept that enables self-breeding without fertile blanket. The resulting core exhibits an average burn-up around 100 GWd/tHM for a corresponding cycle length of 410 equivalent full power days with one fifth reloading scheme.

The carbide core (CAR-3600) was designed to fit a very low linear rate to give an enhanced margin to fuel melting. The core exhibits an average burn-up close to 70 GWd/t determined by the fuel-cladding mechanical interaction limit.

As both cores show low reactivity swing, they share the same basic design (pin definition) for primary and secondary control systems. The operation conditions are specified in Table 2.1.

Table 2.1. Nominal conditions

Reactor power (MWth)	3600
Core inlet temperature (°C)	395
Core outlet temperature (°C)	545
Average core structure temperature (°C) (structure, absorber and coolant medium)	470
Average fuel temperature (°C)	1227 (oxide core) /987 (carbide core)

2.1.1.1 Large-size carbide core (CAR-3600)

The 3600 MWth SFR carbide core [3] layout is presented in Figure 2.1. The core consists of 487 fuel, 270 radial reflector and 27 control subassemblies. The core is divided into inner and outer core zones, which are composed of 286 and 201 fuel assemblies, respectively. Two independent safety-grade reactivity control subsystems are used. The primary control system consists of six control subassemblies in the inner core and 12 control subassemblies at the interface between the inner and the outer zone. The secondary system contains nine control

subassemblies located between the 7th and 8th row. Although the core is surrounded by various materials, a vacuum boundary condition (i.e. no-return current) is used for neutronic modelling.

Figure 2.1. Radial core layout of 3600 MWth carbide core
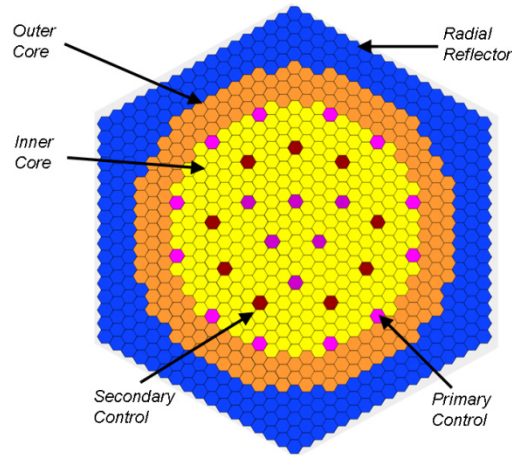
The fuel subassembly consists of a hexagonal wrapper tube that contains a triangular arrangement of helium bonded fuel pins with helical wire wrap spacers. The hexagonal wrapper tube is made of EM10-like steel. The volume of wire wrap spacers is included in the volume of the cladding by means of radius increase in order to simplify the pin description. The fuel pin consists of (U,Pu)C pellets with oxide strengthened steel (ODS) cladding and wire wrap. The fuel density is smeared to account for swelling during irradiation. In the present case, it is assumed that all fuel slugs are in contact with the cladding at the beginning of cycle for simplicity. The fuel subassembly characteristics are summarised in Table 2.2. All the values are given at operating conditions.

Table 2.2. Parameters of fuel subassembly for 3600 MWth carbide core

	Unit	Operating state
Overall length of subassembly: • Lower gas plenum • Lower axial reflector • Active core height • Upper gas plenum • Upper axial reflector	cm	301.70 80.45 30.17 100.56 10.05 80.45
Subassembly pitch, cm	cm	20.9889
Subassembly duct outer flat-to-flat distance	cm	20.2641
Subassembly duct wall thickness	cm	0.4525
Number of fuel pins		469
Outer radius of cladding	cm	a) 0.3954
Inner radius of cladding	cm	0.3470
Fuel slug radius	cm	0.3319

a) Cladding outer radius is increased to compensate for the smearing of the wire-wrap.

The axial description of the fuel subassembly is presented in Figure 2.2. The axial pin design is based on a central one-meter active zone surrounded by two gas plena. The upper one accounts for the top of the pin and has a limited dimension. The axial reflector at the bottom of the active zone is composed of steel pellets located in the pin. The same composition is used also for upper axial reflector for simplicity. The volume fraction of each axial part of the fuel subassembly is presented in Table 2.3.

Figure 2.2. Schematic axial description of fuel subassembly of 3600 MWth carbide core
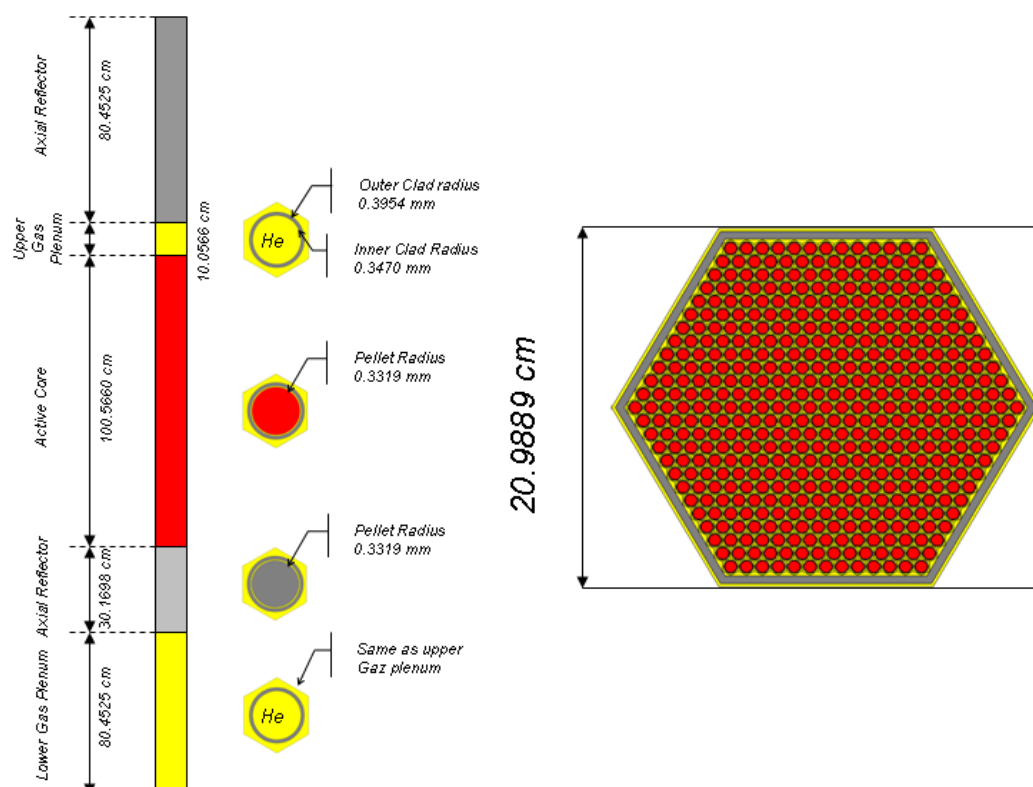
Table 2.3. Volume fraction of fuel subassembly for 3600 MWth carbide core

	Fuel	Sodium	ODS	EM10
Fuel	42.63	31.48	13.90	8.16
Axial reflector	-	31.48	13.90	50.79
Upper gas plenum	-	31.48	13.90	8.16
Lower gas plenum	-	31.48	13.90	8.16

2.1.1.2 Oxide core (MOX-3600)

The 3600 MWth SFR oxide core [2] layout is presented in Figure 2.3. The core consists of 453 fuel, 330 radial reflector and 33 control subassemblies. The core is divided into inner and outer core zones, which are composed of 225 and 228 fuel assemblies, respectively. Two independent safety-grade reactivity control subsystems are used. The primary control system

consists of six control subassemblies in the inner core and 18 control subassemblies at the interface between the inner and the outer zone. The secondary system contains nine control subassemblies located in the 7th row. Although the core is surrounded by various materials, a vacuum boundary condition (i.e. no-return current) is used for neutronic modelling.

Figure 2.3. Radial core layout of 3600 MWth oxide core
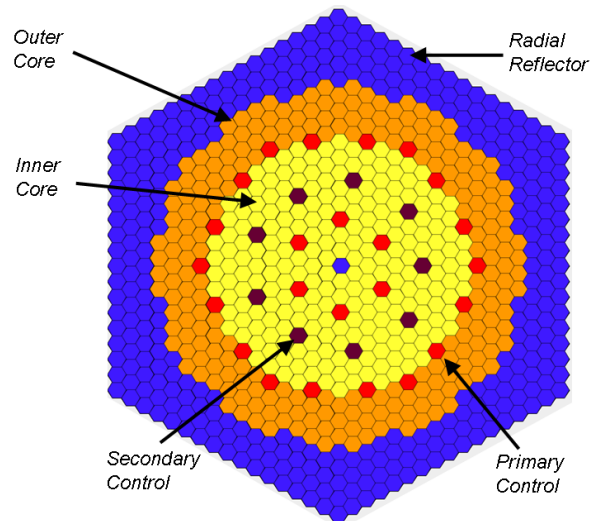
Table 2.4. Parameters of the fuel subassembly of 3600 MWth oxide core

	Unit	Operating state
Overall length of subassembly	cm	311.16
• Lower gas plenum		89.91
• Lower axial reflector		30.17
• Active core height		100.56
• Upper gas plenum		10.05
• Upper axial reflector		80.45
Subassembly pitch	cm	21.2205
Subassembly duct outer flat-to-flat distance	cm	20.7468
Subassembly duct wall thickness	cm	0.4525
Number of fuel pins		271
Outer radius of cladding	cm	a) 0.5419
Inner radius of cladding	cm	0.4893
Fuel slug radius	cm	0.4742

a) Cladding outer radius is increased to compensate for the smearing of the wire-wrap.

The fuel subassembly consists of a hexagonal wrapper tube that contains a triangular arrangement of helium bonded fuel pins with helical wire wrap spacers. The hexagonal wrapper tube is made of EM10-like steel. The volume of wire wrap spacers is included in the volume of the cladding by means of radius increase in order to simplify the pin description. The fuel pin consists of (U,Pu)O$_2$ pellets with oxide strengthened steel (ODS) cladding and wire wrap. The fuel subassembly characteristics are summarised in Table 2.4. All the values are given at operating conditions.

Figure 2.4. Schematic axial description of the fuel subassembly of 3600 MWth oxide core
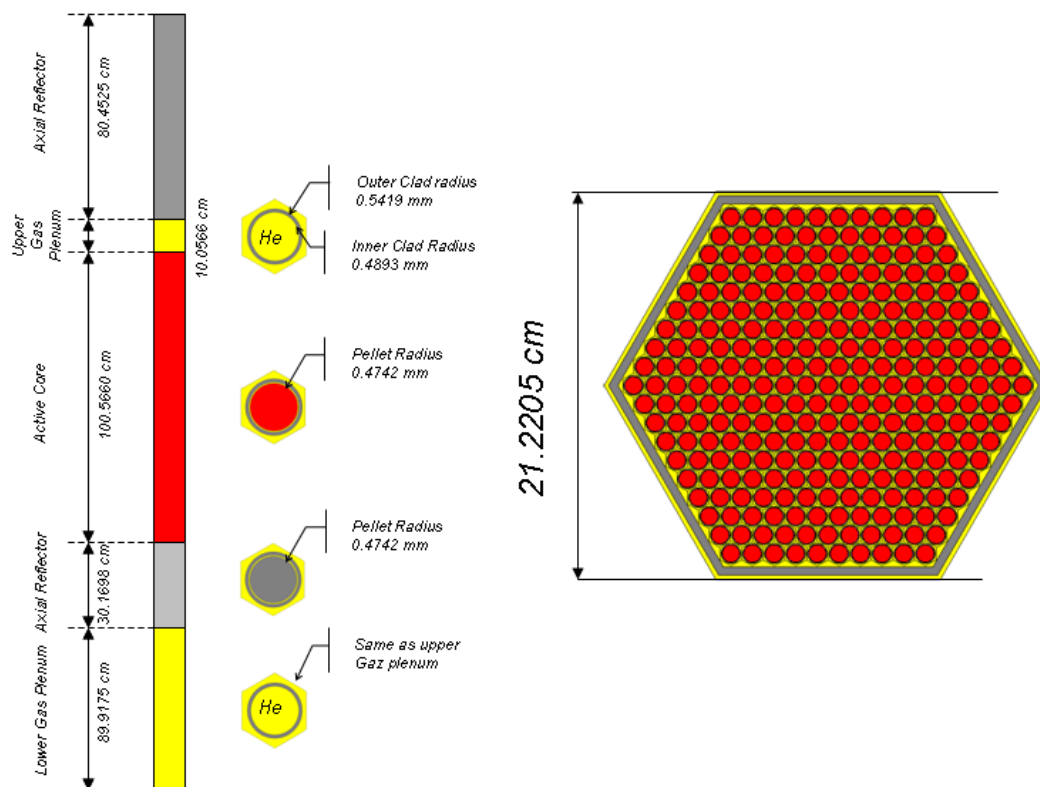
The axial description of the fuel subassembly is presented in Figure 2.4. The axial pin design is based on a central one-meter active zone surrounded by two gas plena. The upper one accounts for the top of the pin and has a limited dimension. The axial reflector at the bottom of the active zone is composed of steel pellets located in the pin. The same composition is used also for upper axial reflector for simplicity. The volume fraction of each axial part of the fuel subassembly is presented in Table 2.5.

Table 2.5. Volume fraction (%) of fuel subassembly of 3600 MWth oxide core

	Fuel	Sodium	ODS	EM10
Fuel	45.63	27.74	11.85	8.14
Axial reflector	-	27.74	11.85	51.50
Upper gas plenum	-	27.74	11.85	8.14
Lower gas plenum	-	27.74	11.85	8.14

2.1.1.3 Control rod design

Both cores used the same control rod description for primary and secondary control systems. The control rod consists of hexagonal lattice of sodium bonded boron carbide pins with wire wrap spacers inside several ducts. The volume of wire wrap spacers is included in the volume of the cladding by means of radius increase in order to simplify the pin description. Due to a low reactivity swing, the primary system uses natural boron carbide, while the secondary system uses enriched ^{10}B boron carbide. The duct and cladding structure used the EM10 material. The primary control subassembly characteristics are summarised in Table 2.6 and illustrated in Figure 2.5. The secondary control subassembly characteristics are summarised in Table 2.7 and illustrated in Figure 2.6.

Table 2.6. Primary control rod characteristics of 3600 MWth cores

	Unit	"Carbide core"	"Oxide core"
Subassembly pitch	cm	20.9889	21.2205
Sodium gap width inter assembly	cm	0.7248	0.4737
Subassembly duct flat-to-flat width	cm	20.2641	20.7468
Wrapper tube thickness	cm	0.4525	0.4525
Outer flat-to-flat internal duct width	cm	15.6883	15.6883
Inner flat-to-flat internal duct width	cm	15.2860	15.2860
Number of pins	cm	37	37
Outer cladding diameter	cm	2.2953	2.2953
Inner cladding diameter	cm	2.0948	2.0948
Pellet diameter	cm	1.8404	1.8404
Pellet material	cm	B$_4$C (natural)	B$_4$C (natural)

Table 2.7. Secondary control rod characteristics of 3600 MWth cores

	Unit	"Carbide core"	"Oxide core"
Subassembly pitch	cm	20.9889	21.2205
Sodium gap width inter assembly	cm	0.7248	0.4737
Subassembly duct flat-to-flat width	cm	20.2641	20.7468
Wrapper tube thickness	cm	0.4525	0.4525
Internal duct outer diameter	cm	14.8838	14.8838
Internal duct inner diameter	cm	14.4815	14.4815
Number of pins	cm	55	55
Outer cladding diameter	cm	1.6443	1.6443
Inner cladding diameter	cm	1.5417	1.5417
Pellet diameter	cm	1.4079	1.4079
Pellet material	cm	B$_4$C (90% ^{10}B)	B$_4$C (90% ^{10}B)

Figure 2.5. Primary control rod description of 3600 MWth cores
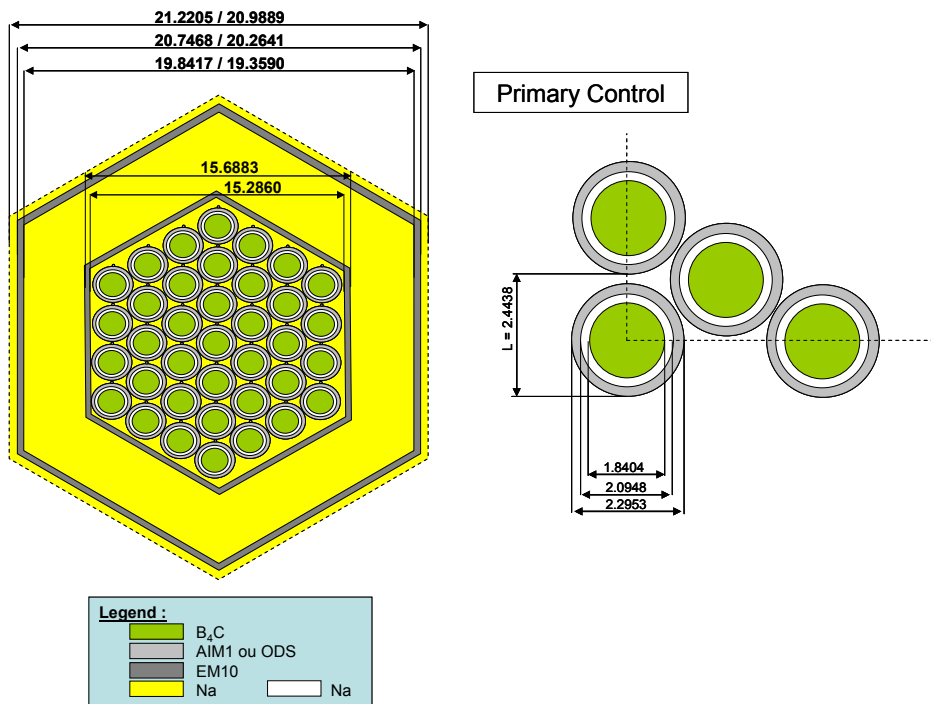
Figure 2.6. Secondary control rod description of 3600 MWth cores
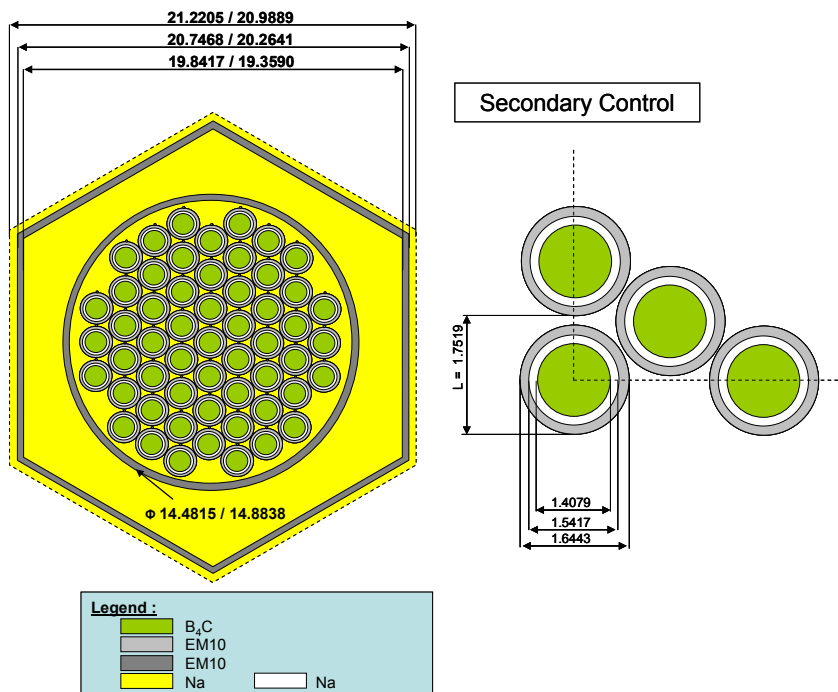
Table 2.8. Volume fraction of primary and secondary subassembly of 3600 MWth cores (%)

	Primary control		Secondary control	
	Carbide	Oxide	Carbide	Oxide
B₄C	25.80	25.24	22.44	21.96
Coolant	56.07	56.83	64.96	65.52
Structure (EM10)	18.13	17.93	12.60	12.52

2.1.1.4 Material description

▪ 2.1.1.4.1 Fuel materials

Data for the nominal operating condition are presented and were calculated by accounting for the effects of thermal expansion and irradiation swelling from the fuel fabrication state. The homogenised compositions of the fuel subassembly are given for both beginning and end of cycle for each core for hot conditions. Here, the subassembly is divided into five axial concentration sets for each different initial Pu contents (inner core and outer core). Fission product isotopes were replaced by a representative isotope (Mo) in terms of equivalent absorption, and only one averaged value is available for each active zone (inner and outer).

The averaged pin compositions per zone are given for hot condition from Tables 2.9 to 2.12. For each core, both the beginning and end of equilibrium cycle (BOC and EOC) number densities are given. Number densities lower than 10^{-10} atoms/barn have been omitted. Here, ^{242g}Am stands for the ground state of ^{242}Am.

Table 2.9. Number densities of inner core fuel pin, 3600 MWth carbide core, BOC (atoms/barn-cm)

Nuclide	Upper boundary from active core bottom (cm)				
	20.11	40.22	60.33	80.44	100.55
C	2.6385E-02	2.6385E-02	2.6385E-02	2.6385E-02	2.6385E-02
^{234}U	1.1919E-06	1.1668E-06	1.1555E-06	1.1735E-06	1.2112E-06
^{235}U	4.6799E-05	4.4631E-05	4.3713E-05	4.5174E-05	4.8320E-05
^{236}U	2.8136E-06	3.1423E-06	3.3299E-06	3.0230E-06	2.4244E-06
^{238}U	2.2303E-02	2.2143E-02	2.2084E-02	2.2177E-02	2.2382E-02
^{237}Np	2.5168E-06	3.4681E-06	3.7208E-06	3.3324E-06	2.2640E-06
^{239}Np	3.5946E-06	4.4531E-06	4.7916E-06	4.2607E-06	3.1154E-06
^{238}Pu	1.0646E-04	1.0306E-04	1.0175E-04	1.0383E-04	1.0844E-04
^{239}Pu	1.8140E-03	1.8594E-03	1.8745E-03	1.8508E-03	1.7942E-03
^{240}Pu	1.0229E-03	1.0161E-03	1.0165E-03	1.0155E-03	1.0185E-03
^{241}Pu	2.4210E-04	2.3422E-04	2.3224E-04	2.3519E-04	2.4351E-04
^{242}Pu	3.4136E-04	3.3784E-04	3.3674E-04	3.3844E-04	3.4252E-04
^{241}Am	3.7572E-05	3.6180E-05	3.5616E-05	3.6509E-05	3.8462E-05
^{242g}Am	1.0156E-08	1.1575E-08	1.2270E-08	1.1142E-08	8.7856E-09
^{242m}Am	6.9199E-07	7.7557E-07	8.1635E-07	7.4933E-07	6.0460E-07
^{243}Am	1.4205E-05	1.6267E-05	1.7351E-05	1.5594E-05	1.2110E-05
^{242}Cm	1.0156E-08	1.1575E-08	1.2270E-08	1.1142E-08	8.7856E-09
^{243}Cm	1.6209E-06	1.8567E-06	1.9718E-06	1.7856E-06	1.3992E-06
^{244}Cm	4.3067E-08	5.3407E-08	6.0550E-08	4.9215E-08	3.0944E-08
^{245}Cm	1.0655E-06	1.4363E-06	1.6492E-06	1.3185E-06	7.7138E-07
^{246}Cm	2.7855E-08	4.4683E-08	5.5003E-08	3.9501E-08	1.7550E-08
Mo	1.3400E-03	1.3400E-03	1.3400E-03	1.3400E-03	1.3400E-03

**Table 2.10. Number densities of outer core fuel pin, 3600 MWth
carbide core, BOC (atoms/barn-cm)**

Nuclide	Upper boundary from active core bottom (cm)				
	20.11	40.22	60.33	80.44	100.55
C	2.6385E-02	2.6385E-02	2.6385E-02	2.6385E-02	2.6385E-02
^{234}U	2.2313E-06	2.1245E-06	2.0828E-06	2.1405E-06	2.2687E-06
^{235}U	3.6556E-05	3.3005E-05	3.1658E-05	3.3521E-05	3.7812E-05
^{236}U	3.8682E-06	4.4412E-06	4.7031E-06	4.3381E-06	3.5850E-06
^{238}U	1.9613E-02	1.9319E-02	1.9211E-02	1.9359E-02	1.9697E-02
^{237}Np	4.0477E-06	5.6298E-06	6.0470E-06	5.4769E-06	3.7682E-06
^{239}Np	3.0567E-06	3.9393E-06	4.2728E-06	3.8143E-06	2.7851E-06
^{238}Pu	1.2031E-04	1.1288E-04	1.1019E-04	1.1390E-04	1.2263E-04
^{239}Pu	2.1078E-03	2.1362E-03	2.1436E-03	2.1335E-03	2.1019E-03
^{240}Pu	1.2520E-03	1.2386E-03	1.2385E-03	1.2384E-03	1.2492E-03
^{241}Pu	2.7216E-04	2.5863E-04	2.5524E-04	2.5984E-04	2.7437E-04
^{242}Pu	4.0896E-04	4.0010E-04	3.9726E-04	4.0115E-04	4.1086E-04
^{241}Am	5.2029E-05	4.8117E-05	4.6701E-05	4.8656E-05	5.3279E-05
^{242g}Am	1.3235E-08	1.5409E-08	1.6296E-08	1.5069E-08	1.2281E-08
^{242m}Am	1.3674E-06	1.5394E-06	1.6065E-06	1.5130E-06	1.2836E-06
^{243}Am	2.6522E-05	3.1778E-05	3.4010E-05	3.0910E-05	2.4305E-05
^{242}Cm	2.3638E-06	2.7689E-06	2.9338E-06	2.7054E-06	2.1894E-06
^{243}Cm	1.0326E-07	1.3838E-07	1.5726E-07	1.3092E-07	8.5277E-08
^{244}Cm	3.2259E-06	4.8143E-06	5.5901E-06	4.5164E-06	2.6306E-06
^{245}Cm	1.3656E-07	2.5044E-07	3.1218E-07	2.2707E-07	9.9197E-08
^{246}Cm	3.0878E-09	7.2444E-09	9.7807E-09	6.3131E-09	1.9680E-09
Mo	1.8258E-03	1.8258E-03	1.8258E-03	1.8258E-03	1.8258E-03

**Table 2.11. Number densities of inner core fuel pin, 3600 MWth
oxide core, BOC (atoms/barn-cm)**

Nuclide	Upper boundary from active core bottom (cm)				
	20.11	40.22	60.33	80.44	100.55
O	4.2825E-02	4.2825E-02	4.2825E-02	4.2825E-02	4.2825E-02
^{234}U	1.7602E-06	1.6854E-06	1.6555E-06	1.7055E-06	1.8159E-06
^{235}U	3.3412E-05	3.0308E-05	2.9137E-05	3.1106E-05	3.5674E-05
^{236}U	4.0736E-06	4.5416E-06	4.7679E-06	4.3769E-06	3.5242E-06
^{238}U	1.8692E-02	1.8418E-02	1.8322E-02	1.8479E-02	1.8833E-02
^{237}Np	3.7863E-06	5.1775E-06	5.5220E-06	4.9657E-06	3.3888E-06
^{239}Np	3.5878E-06	4.5073E-06	4.8411E-06	4.2905E-06	3.0633E-06
^{238}Pu	9.4366E-05	8.8933E-05	8.6992E-05	9.0233E-05	9.7746E-05
^{239}Pu	1.8178E-03	1.8701E-03	1.8845E-03	1.8611E-03	1.7967E-03
^{240}Pu	1.0177E-03	1.0093E-03	1.0108E-03	1.0077E-03	1.0089E-03
^{241}Pu	2.1797E-04	2.0709E-04	2.0474E-04	2.0843E-04	2.1989E-04
^{242}Pu	3.2651E-04	3.1969E-04	3.1762E-04	3.2097E-04	3.2894E-04
^{241}Am	4.0395E-05	3.7459E-05	3.6419E-05	3.8152E-05	4.2233E-05
^{242g}Am	1.2900E-08	1.4609E-08	1.5317E-08	1.4098E-08	1.1216E-08
^{242m}Am	1.2243E-06	1.3387E-06	1.3853E-06	1.3029E-06	1.0866E-06
^{243}Am	2.4048E-05	2.7848E-05	2.9501E-05	2.6690E-05	2.0522E-05
^{242}Cm	2.2643E-06	2.5789E-06	2.7086E-06	2.4860E-06	1.9640E-06
^{243}Cm	1.0596E-07	1.3294E-07	1.4828E-07	1.2228E-07	7.5767E-08
^{244}Cm	3.2454E-06	4.5321E-06	5.1600E-06	4.1266E-06	2.3121E-06
^{245}Cm	1.4745E-07	2.4624E-07	2.9876E-07	2.1432E-07	8.9736E-08
^{246}Cm	3.4906E-09	7.2920E-09	9.5184E-09	6.0399E-09	1.8114E-09
Mo	2.7413E-03	2.7413E-03	2.7413E-03	2.7413E-03	2.7413E-03

Table 2.12. Number densities of outer core fuel pin, 3600 MWth oxide core, BOC (atoms/barn-cm)

Nuclide	Upper boundary from active core bottom (cm)				
	20.11	40.22	60.33	80.44	100.55
O	4.2825E-02	4.2825E-02	4.2825E-02	4.2825E-02	4.2825E-02
^{234}U	2.0797E-06	1.9802E-06	1.9413E-06	1.9951E-06	2.1146E-06
^{235}U	3.4073E-05	3.0762E-05	2.9508E-05	3.1243E-05	3.5243E-05
^{236}U	3.6055E-06	4.1395E-06	4.3836E-06	4.0434E-06	3.3415E-06
^{238}U	1.8281E-02	1.8006E-02	1.7906E-02	1.8044E-02	1.8359E-02
^{237}Np	3.7727E-06	5.2474E-06	5.6362E-06	5.1048E-06	3.5123E-06
^{239}Np	2.8490E-06	3.6717E-06	3.9825E-06	3.5552E-06	2.5959E-06
^{238}Pu	1.1214E-04	1.0521E-04	1.0271E-04	1.0616E-04	1.1430E-04
^{239}Pu	1.9646E-03	1.9910E-03	1.9980E-03	1.9885E-03	1.9591E-03
^{240}Pu	1.1670E-03	1.1545E-03	1.1543E-03	1.1543E-03	1.1643E-03
^{241}Pu	2.5367E-04	2.4106E-04	2.3790E-04	2.4218E-04	2.5573E-04
^{242}Pu	3.8118E-04	3.7292E-04	3.7027E-04	3.7390E-04	3.8295E-04
^{241}Am	4.8494E-05	4.4849E-05	4.3528E-05	4.5350E-05	4.9660E-05
^{242g}Am	1.2336E-08	1.4363E-08	1.5189E-08	1.4045E-08	1.1447E-08
^{242m}Am	1.2745E-06	1.4348E-06	1.4973E-06	1.4102E-06	1.1964E-06
^{243}Am	2.4720E-05	2.9619E-05	3.1700E-05	2.8811E-05	2.2654E-05
^{242}Cm	2.2032E-06	2.5808E-06	2.7345E-06	2.5216E-06	2.0406E-06
^{243}Cm	9.6244E-08	1.2898E-07	1.4657E-07	1.2203E-07	7.9484E-08
^{244}Cm	3.0067E-06	4.4873E-06	5.2103E-06	4.2096E-06	2.4519E-06
^{245}Cm	1.2729E-07	2.3343E-07	2.9097E-07	2.1164E-07	9.2458E-08
^{246}Cm	2.8780E-09	6.7522E-09	9.1163E-09	5.8843E-09	1.8343E-09
Mo	2.9100E-03	2.9100E-03	2.9100E-03	2.9100E-03	2.9100E-03

- 2.1.1.4.2 Structure, coolant and absorber materials

Both cores used the same cladding, duct and absorber materials composition. Table 2.13 and Table 2.14 present the number densities at nominal operation condition to be used in this benchmark.

Table 2.13. Structure and coolant material number densities of 3600 MWth cores (atoms/barn)

Element	Duct (EM10)	Cladding (ODS)	Coolant (Na)
Na			2.1924E-02
C	3.8254E-04	3.5740E-04	
O		3.9924E-04	
Si	4.9089E-04		
Ti	1.9203E-05	5.3824E-04	
Cr	7.5122E-03	1.7753E-02	
Fe	7.3230E-02	5.3872E-02	
Ni	3.9162E-04	3.6588E-04	
Mo	4.7925E-04		
Mn	4.1817E-04	2.3441E-04	
P		2.7718E-05	
Al		9.1482E-03	
Co		2.1852E-04	
Cu		1.0135E-04	
Y		2.6616E-04	

Table 2.14. Absorber material number densities of 3600 MWth cores (atoms/barn)

Element	Primary control	Secondary control
C	2.70E-02	2.70E-02
^{10}B	2.32E-02	9.81E-02
^{11}B	8.49E-02	9.91E-03

2.1.2 Medium size cores

The numerical benchmark specification for the 1000 MWth medium-size benchmark cores, which were developed from the reference Advanced Burner Reactor (ABR) core concept [4] with a ternary metallic fuel and a mixed-oxide fuel, is presented in this section. The ABR core concepts having 1000 MWth power rating were developed for study of future fast reactor design options under the Global Nuclear Energy Partnership (GNEP) Program. Compact core concepts with a transuranics (TRU) conversion ratio of ~0.7 were developed for a one-year cycle length with 90% capacity factor. Conventional or reasonably proven materials were utilised in the ABR core concepts so that the core stays within current fast reactor technology knowledge base. The benchmark has been developed for a core using ternary metallic alloy fuel.

Data is provided for the nominal operating condition of the ABR core using fuel compositions associated with the equilibrium cycle. The ABR equilibrium cycle was determined by recycling all discharged TRU with an external make-up TRU feed recovered from LWR used nuclear fuel.

2.1.2.1 Medium-size metallic core (MET-1000)

Figure 2.7 shows the radial core layout of the 1000 MWth medium-size metallic benchmark core. The core consists of 180 driver, 114 radial reflector, 66 radial shield and 19 control subassemblies. The core is divided into inner and outer core zones, which are composed of 78 and 102 driver assemblies, respectively. Two independent safety-grade reactivity control subsystems are used. The primary control system consists of three control subassemblies in the fourth row and 12 control subassemblies in the seventh row. The secondary system contains four control subassemblies located at the core centre and in the fourth row. Although the core is surrounded by various materials, a vacuum boundary condition (i.e. no-return current) is imposed in the benchmark.

The nominal power is 1000 MWth and the core inlet and bulk outlet temperatures are 355°C and 510°C, respectively. The core temperature distribution is dependent on the power distribution, but uniform temperature values in the coolant, structural materials, and fuel have been assumed in this benchmark problem for simplicity. Table 2.15 contains data for the nominal operating condition.

Figure 2.7. Radial core layout of 1000 MWth metallic-fuel core

Inner core (78)

Outer core (102)

Reflector (114)

P Primary control (15)

S Secondary control (4)

Shield (66)

Total (379)
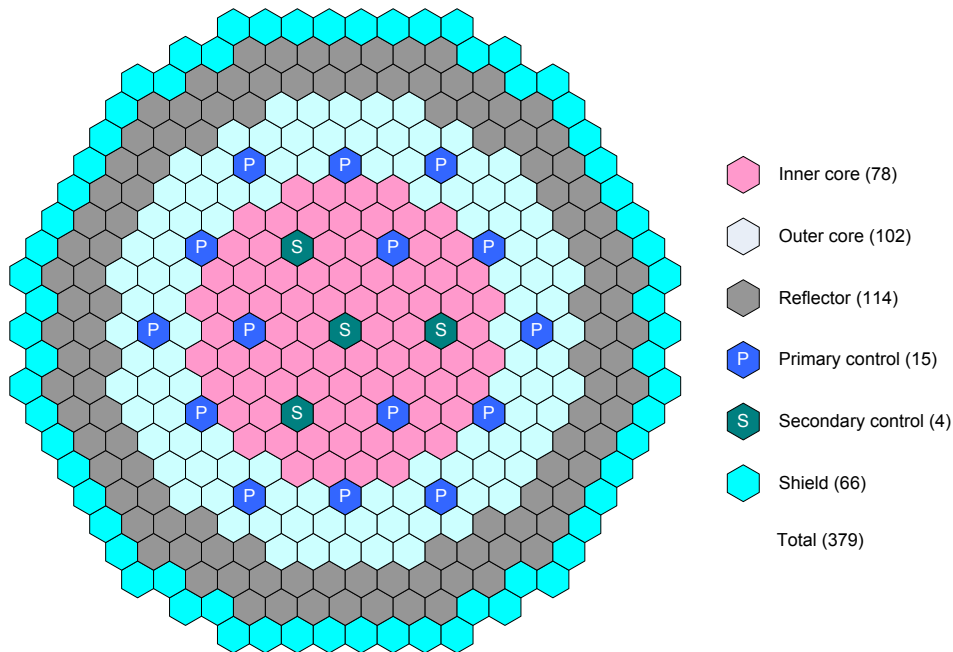
Table 2.15. Nominal operating condition of 1000 MWth metallic core

	Unit	Value
Reactor power	MW-thermal	1000.0
Coolant temperature	°C	432.5
Average core structural temperature	°C	432.5
Average fuel temperature	°C	534.0

The design parameters of the driver, radial reflector, radial shield, and control subassemblies are provided in Tables 2.16 to 2.19, respectively. Data for the nominal operating condition are presented and were calculated by accounting for the effects of thermal expansion and irradiation swelling from the fuel fabrication state.

At the fabrication state, the fuel pin and control rod are helically wrapped with wire for accommodating the coolant flow. Here, the wire-wrap has been smeared with the cladding in order to simplify the cladding geometry. As a result, the outer radii of the fuel and control rod claddings are slightly increased to compensate for the smeared wire-wrap.

For accommodating irradiation induced swelling, the smeared density of the fresh fuel is 75% and bond sodium is used to fill the gap between the metallic fuel slug and cladding. Although fresh and burned fuels co-exist at the beginning of the equilibrium cycle (BOC), it is assumed that all fuel slugs contact the cladding, the fuel slug grows 5% by the effect of irradiation swelling, and the bond sodium is displaced to the lower part of the upper gas plenum.

Figures 2.8 to 2.11 show the schematics of the driver, radial reflector, radial shield, and control subassemblies, respectively, and the volume fractions at the nominal operating condition are provided in Table 2.20. For all subassemblies, the duct and cladding is made of HT-9. Subassembly characteristics are described from Tables 2.16 to 2.19.

Each driver subassembly contains 271 fuel pins arranged in a triangular pitch array. The fuel and coolant volume fractions are 39% and 35%, respectively. The sodium volume fraction in the lower part of the gas plenum increases to 74% because of the displaced bond sodium and the helium gas in the gas plenum is ignored. The lower structure is assumed to be a homogeneous mixture of sodium (70%) and SS-316 (30%), and the lower reflector consists of 271 solid HT-9 pins. For simplicity, the upper structure is assumed to be identical to the lower reflector.

The reflector subassembly contains 91 solid HT-9 pins arranged in a triangular pitch array. The shield subassembly consists of 19 thick HT-9 tubes (cladding) containing boron carbide pellets. Natural boron (19.1% atomic fraction) is used with 81% smeared B_4C pellet density. The control subassembly consists of two ducts: interior and outer ducts. The outer duct is identical to the driver subassembly duct. The external dimension of the interior duct is smaller than that of the outer duct to allow free motion within the outer duct. Seven control rods are contained in the interior duct. The control rod consists of a HT-9 tube containing boron carbide pellets. Enriched boron (65% atomic fraction) is used with 85% smeared B_4C pellet density. For simplicity of the depletion model, all structural materials including boron are assumed to be non-depleted. In this benchmark, it is assumed that the lower structure, lower reflector and upper structure of the reflector, shield and control subassemblies are identical to those of the driver subassembly.

Table 2.16. Parameters for driver subassembly of 1000 MWth metallic core

	Unit	Operating state
Overall length of subassembly	cm	480.20
• Lower structure		35.76
• Lower reflector		125.16
• Active core height		85.82
• Replaced bond sodium		20.06
• Gas plenum		101.01
• Upper structure		112.39
Subassembly pitch, cm	cm	16.2471
Subassembly duct outer flat-to-flat distance	cm	15.8123
Subassembly duct wall thickness	cm	0.3966
Number of fuel pins		271
Outer radius of cladding	cm	a) 0.3857
Inner radius of cladding	cm	0.3236
Fuel slug radius	cm	0.3236

a) Cladding outer radius has been slightly increased to
   compensate for the smearing of the wire-wrap with the cladding.

Table 2.17. Parameters for radial reflector subassembly of 1000 MWth metallic core

	Unit	Operating state
Overall length of subassembly	cm	480.20
• Lower structure		35.76
• Lower reflector		125.16
• Radial reflector		206.89
• Upper structure		112.39
Subassembly pitch, cm	cm	16.2471
Subassembly duct outer flat-to-flat distance	cm	15.8123
Subassembly duct wall thickness	cm	0.3966
Number of fuel pins		91
Rod radius	cm	0.7757

Table 2.18. Parameters for shielding subassembly of 1000 MWth metallic core

	Unit	Operating state
Overall length of subassembly	cm	480.20
• Lower structure		35.76
• Lower reflector		125.16
• Radial shield		206.89
• Upper structure		112.39
Subassembly pitch, cm	cm	16.2471
Subassembly duct outer flat-to-flat distance	cm	15.8123
Subassembly duct wall thickness	cm	0.3966
Number of fuel pins		19
Outer radius of cladding	cm	1.6794
Inner radius of cladding	cm	1.4277
Absorber radius	cm	1.4277

Table 2.19. Parameters for control assembly of 1000 MWth metallic core

	Unit	Operating state
Overall length of subassembly	cm	480.20
• Lower structure		35.76
• Lower reflector		125.16
• Absorber		86.75
• Empty duct		232.53
Subassembly pitch, cm	cm	16.2471
Subassembly duct outer flat-to-flat distance	cm	15.8123
Subassembly duct wall thickness	cm	0.3966
Interior duct outer flat-to-flat distance	cm	14.2140
Interior duct wall thickness	cm	0.3966
Number of fuel pins		7
Outer radius of cladding	cm	a) 2.3606
Inner radius of cladding	cm	2.2890
Absorber radius	cm	2.2890

a) Cladding outer radius is increased to compensate
   for the smearing of the wire-wrap.

Figure 2.8. Schematics of driver subassembly of 1000 MWth metallic core

Section A-A

Fuel pin

Duct
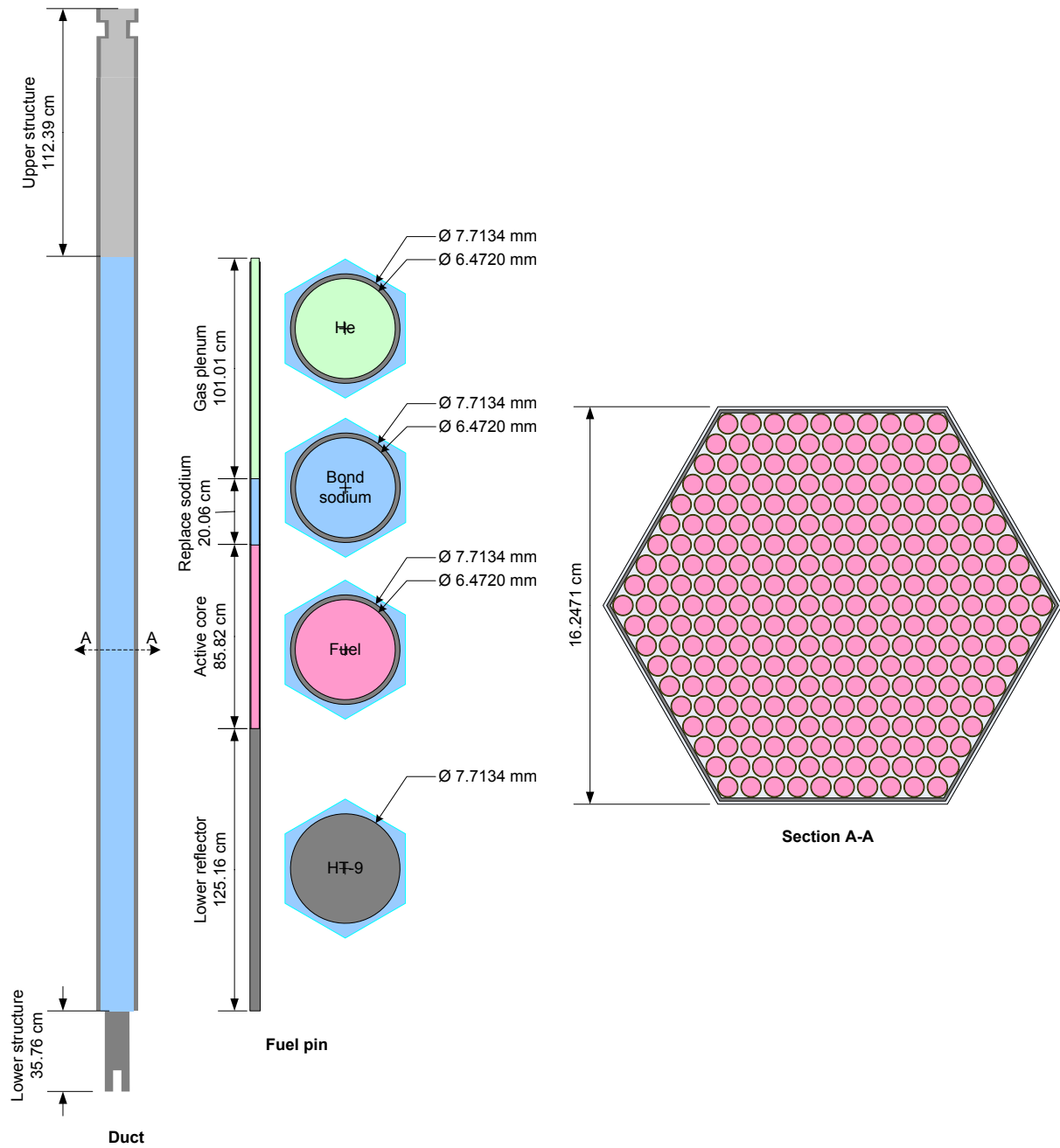
Figure 2.9. Schematics of radial reflector subassembly of 1000 MWth metallic core

Upper structure
112.39 cm

Radial reflector
206.89 cm

A   A

Ø 15.513 mm

HT-9

16.2471 cm

Reflector rod

Section A-A

Lower reflector
125.16 cm

Lower structure
35.76 cm

Duct
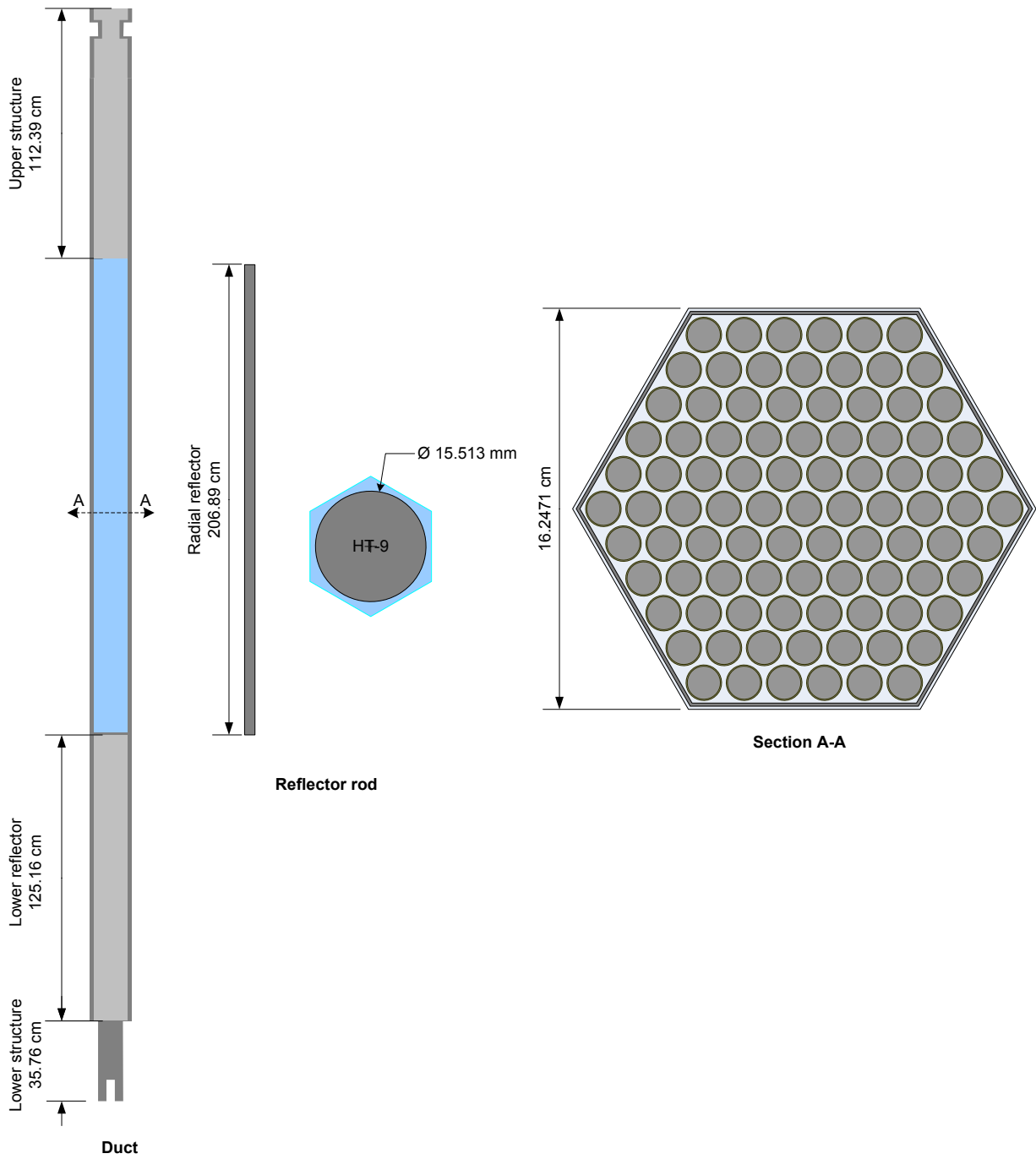
Figure 2.10. Schematics of radial shield subassembly of 1000 MWth metallic core

Upper structure
112.39 cm

Shield rod
206.89 cm

Ø 33.5875 mm

Ø 28.5549 mm

Shield

16.2471 cm

Section A-A

Shield rod

Lower reflector
125.16 cm

Lower structure
35.76 cm

Duct
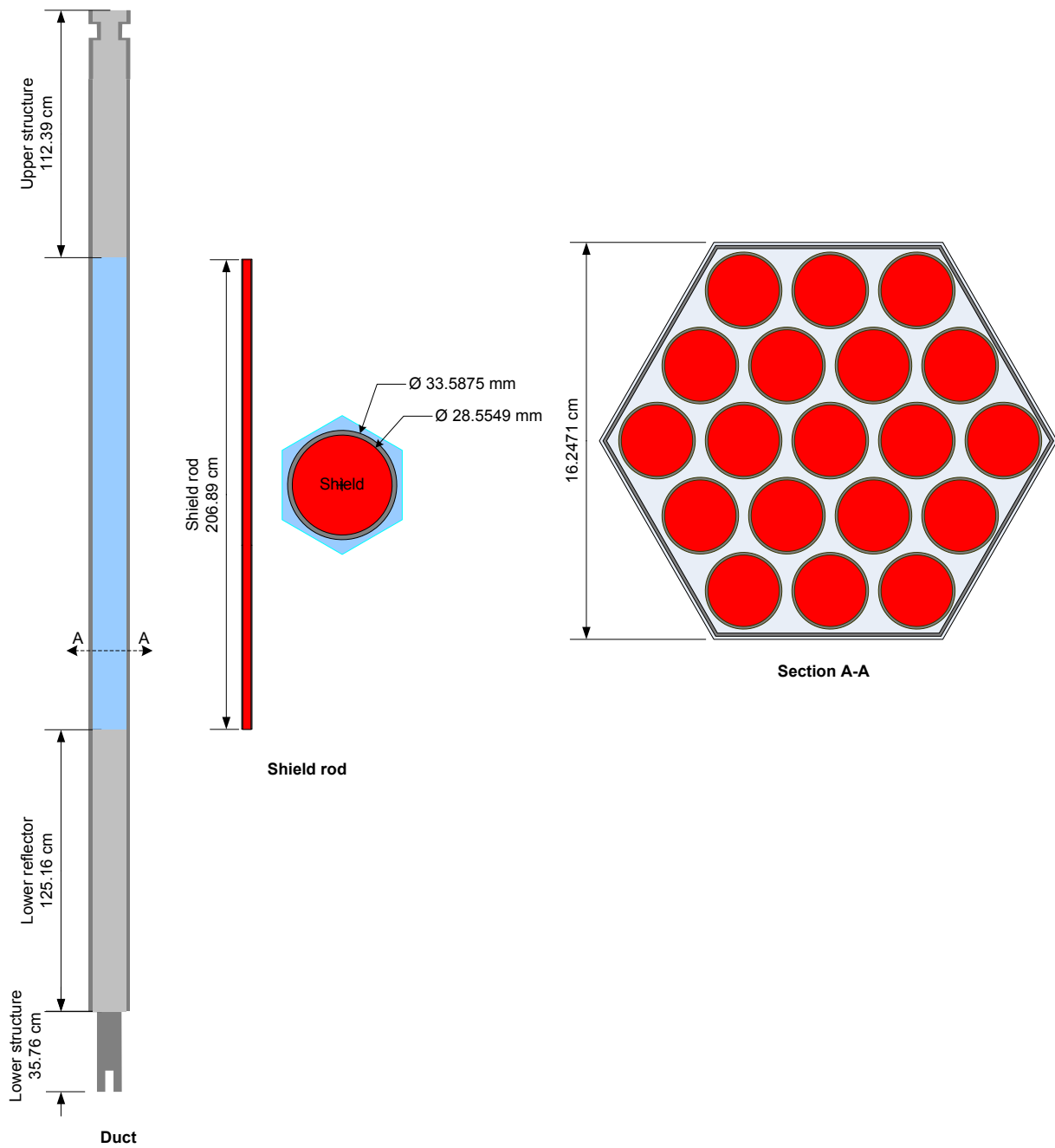
Figure 2.11. Schematics of control subassembly of 1000 MWth metallic core

Empty duct
146.71 cm

Control absorber
86.75 cm

Empty duct
85.82 cm
(active core)

Lower reflector
125.16 cm

Lower structure
35.56 cm

**Control Rod Assembly
(when fully withdrawn)**

Ø 47.2126 mm
Ø 45.7801 mm

Absorber

Subassembly duct
Interior duct

Section A-A
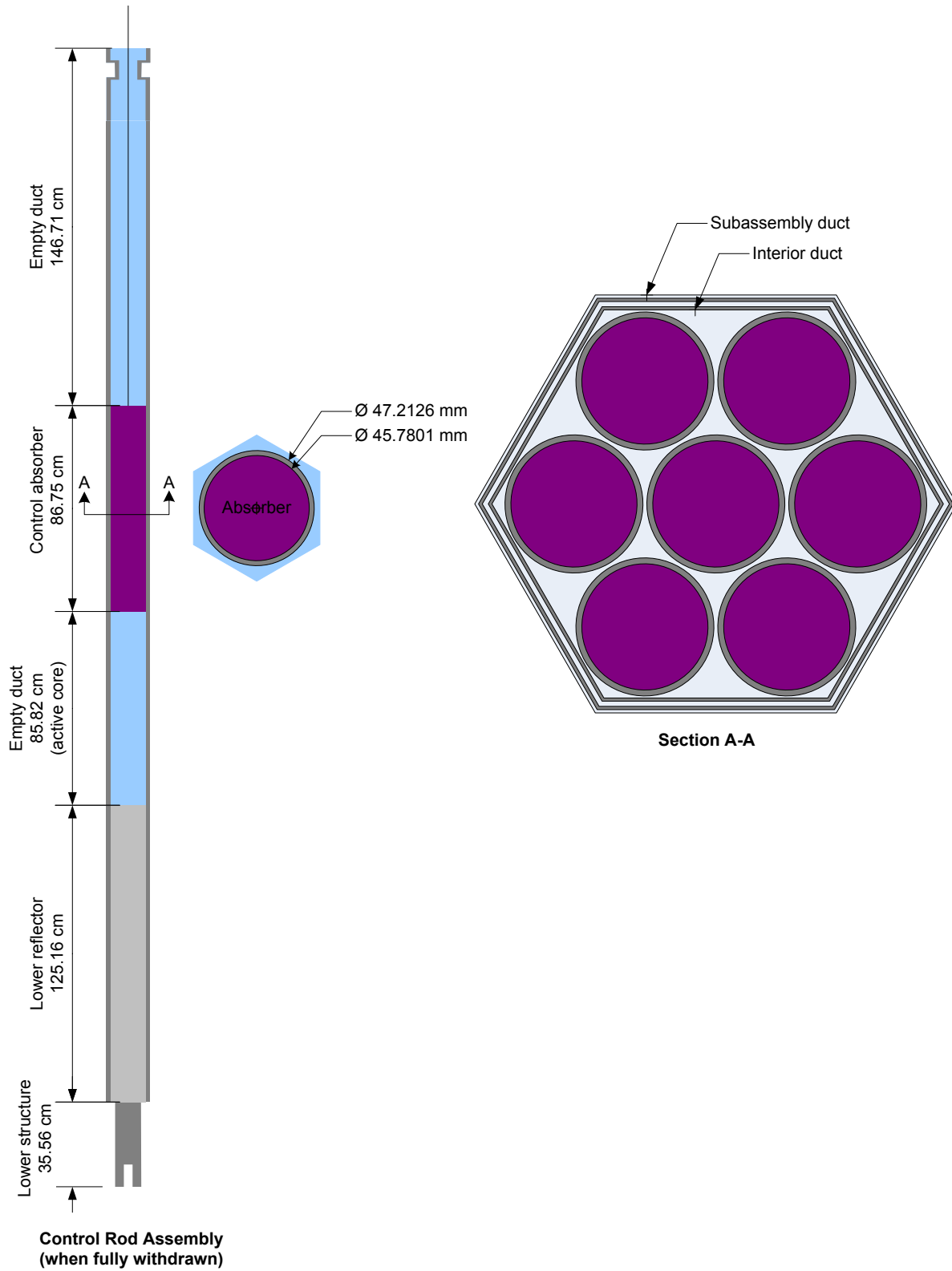
Table 2.20. Volume fractions of 1000 MWth metallic core (%)

Region		Coolant	HT-9	Fuel	Natural B$_4$C	Enriched B$_4$C
Lower structure		Homogeneous mixture of 30% SS-316 and 70% Sodium				
Lower reflector		35.34	64.66			
Upper structure		35.34	64.66			
Driver	Active core	35.34	25.66	39.00		
	Displaced bond sodium	74.34	25.66			
	Gas plenum	35.34	25.66			
Radial reflector		15.50	84.50			
Radial shield		17.10	29.68		53.23	
Absorber in control subassembly		28.83	20.77			50.40
Empty duct in control subassembly		90.74	9.26			

2.1.2.2 Material description for metallic core

The fuel compositions are obtained from the reference ABR core data at the beginning of equilibrium cycle (BOC). For the reference ABR core concept, the equilibrium cycle was determined by recycling all discharged TRU. For external make-up TRU feed, TRU recovered from LWR used nuclear fuel is assumed. At the equilibrium cycle, the TRU conversion ratio is ~0.7 and cycle length is 328.5 days with full power operation.

As for large core description, the variation of fuel composition in the irradiated core is simplified. The active core is axially divided into five zones and uniform fuel composition is assumed in each zone. Thus, ten different fuel compositions are provided in this benchmark: five each for the inner and outer cores, respectively. A simplified fission product model is also adopted with a pseudo fission product. Natural molybdenum is used to represent the fission products (pseudo fission product).

Table 2.21. Number densities of coolant and structural materials (atoms/barn-cm)

Material	Nuclide	Number density
Lower structure (homogeneous mixture of SS-316 and Sodium)	Na	1.5591E-02
	Fe	1.5878E-02
	Ni	3.2604E-03
	Cr	3.2355E-03
	^{55}Mn	5.0846E-04
	Mo	4.3524E-04
Coolant	Na	2.2272E-02
HT-9	Fe	6.9715E-02
	Ni	4.2984E-04
	Cr	1.0366E-02
	^{55}Mn	4.5921E-04
	Mo	4.9007E-04
Natural B$_4$C	C	1.9657E-02
	^{10}B	1.5018E-02
	^{11}B	6.3609E-02
Enriched B$_4$C	C	2.0632E-02
	^{10}B	5.3642E-02
	^{11}B	2.8884E-02

Table 2.21 provides the number densities of coolant and structural materials. The fuel pin compositions for the inner and outer cores at BOC are provided in Table 2.22 and Table 2.23, respectively. All data are obtained for the nominal operating condition by adjusting for the effects of thermal expansion and irradiation swelling. As mentioned in previous chapters, it is assumed that all subassemblies have the same lower structure, lower reflector and upper structure and the material volume fractions are provided in Table 2.20. It is noted that the homogenised number densities at the nominal operating condition can be calculated by using the volume fractions in Table 2.20 and the number densities provided in Tables 2.21 to 2.23.

Table 2.22. Number densities of inner core fuel pin, 1000 MWth metallic core, BOC (atoms/barn-cm)

Nuclide	Upper boundary from active core bottom (cm)				
	17.16	34.33	51.49	68.66	85.82
^{234}U	1.1369E-06	1.0856E-06	1.0727E-06	1.1028E-06	1.1759E-06
^{235}U	3.0421E-05	2.9338E-05	2.8961E-05	3.0070E-05	3.2571E-05
^{236}U	2.4896E-06	2.5117E-06	2.5536E-06	2.3779E-06	2.0226E-06
^{238}U	1.9613E-02	1.9474E-02	1.9433E-02	1.9550E-02	1.9801E-02
^{237}Np	4.6686E-05	4.6962E-05	4.6782E-05	4.7603E-05	4.8895E-05
^{236}Pu	4.9700E-10	5.5883E-10	5.6701E-10	5.5075E-10	4.8775E-10
^{238}Pu	1.1695E-04	1.1284E-04	1.1196E-04	1.1370E-04	1.1829E-04
^{239}Pu	2.2076E-03	2.1814E-03	2.1754E-03	2.1813E-03	2.2011E-03
^{240}Pu	1.3244E-03	1.2955E-03	1.2902E-03	1.2986E-03	1.3248E-03
^{241}Pu	1.9375E-04	1.8610E-04	1.8518E-04	1.8537E-04	1.8845E-04
^{242}Pu	2.9277E-04	2.8911E-04	2.8818E-04	2.9038E-04	2.9569E-04
^{241}Am	1.0791E-04	1.0465E-04	1.0353E-04	1.0686E-04	1.1421E-04
^{242m}Am	9.2989E-06	9.0848E-06	9.0224E-06	9.1756E-06	9.4890E-06
^{243}Am	1.0017E-04	9.8324E-05	9.7993E-05	9.8630E-05	1.0032E-04
^{242}Cm	5.6250E-06	5.8208E-06	5.9476E-06	5.4901E-06	4.5416E-06
^{243}Cm	5.4321E-07	5.0246E-07	5.0136E-07	4.8876E-07	4.8480E-07
^{244}Cm	6.7240E-05	6.5722E-05	6.5622E-05	6.5349E-05	6.5394E-05
^{245}Cm	1.7397E-05	1.6743E-05	1.6663E-05	1.6696E-05	1.7026E-05
^{246}Cm	9.2285E-06	9.1426E-06	9.1307E-06	9.1364E-06	9.1805E-06
Zr	7.2802E-03	7.2802E-03	7.2802E-03	7.2802E-03	7.2802E-03
^{a}Mo	9.2873E-04	1.1464E-03	1.2031E-03	1.0625E-03	7.4065E-04

a) representative for pseudo fission product

2.1.2.3 Medium-size oxide core (MOX-1000)

The medium size oxide benchmark core was also developed from the ABR oxide core concept, which was developed to allow the interchange of metal and oxide fuel subassemblies. Thus, the total number of driver subassemblies, the locations of the control subassemblies, and outer-dimensions of the oxide-fuel subassembly are identical to those of the metallic core. However, the internal subassembly design parameters such as fuel pin diameter, volume fractions, active fuel height, etc., and the arrangement of the driver subassemblies were determined to meet the ABR design goal of a compact core concept with medium TRU conversion ratio and one-year operation.

Figure 2.12 shows the radial layout of the 1000 MWth oxide benchmark core. The core consists of 180 driver, 114 radial reflector, 66 radial shield, and 19 control subassemblies. The core is divided into inner, middle, and outer core zones, which are composed of 30, 90, and 92 driver assemblies, respectively. A vacuum boundary condition is also imposed in the 1000 MWth oxide benchmark core.

**Table 2.23. Number densities of outer core fuel pin, 1000 MWth
metallic core, BOC (atoms/barn-cm)**

Nuclide	Upper boundary from active core bottom (cm)				
	17.16	34.33	51.49	68.66	85.82
^{234}U	1.6317E-06	1.5766E-06	1.5638E-06	1.5894E-06	1.6552E-06
^{235}U	3.0822E-05	2.9870E-05	2.9561E-05	3.0391E-05	3.2250E-05
^{236}U	1.7881E-06	1.8534E-06	1.8941E-06	1.7528E-06	1.4710E-06
^{238}U	1.8244E-02	1.8144E-02	1.8115E-02	1.8191E-02	1.8359E-02
^{237}Np	9.8244E-05	9.7300E-05	9.6775E-05	9.8481E-05	1.0175E-04
^{236}Pu	7.1175E-10	8.2505E-10	8.4282E-10	8.0703E-10	6.8053E-10
^{238}Pu	1.6436E-04	1.6026E-04	1.5949E-04	1.6063E-04	1.6416E-04
^{239}Pu	2.8147E-03	2.7664E-03	2.7538E-03	2.7786E-03	2.8416E-03
^{240}Pu	1.7467E-03	1.7191E-03	1.7135E-03	1.7231E-03	1.7508E-03
^{241}Pu	2.8976E-04	2.8138E-04	2.8012E-04	2.8135E-04	2.8697E-04
^{242}Pu	4.0754E-04	4.0412E-04	4.0321E-04	4.0530E-04	4.1028E-04
^{241}Am	1.8607E-04	1.8127E-04	1.7970E-04	1.8397E-04	1.9339E-04
^{242m}Am	1.2185E-05	1.2045E-05	1.2021E-05	1.2039E-05	1.2064E-05
^{243}Am	1.3234E-04	1.3019E-04	1.2985E-04	1.3036E-04	1.3206E-04
^{242}Cm	6.4688E-06	6.8630E-06	7.0553E-06	6.4446E-06	5.1976E-06
^{243}Cm	6.3471E-07	6.0893E-07	6.0901E-07	5.9753E-07	5.9372E-07
^{244}Cm	8.0107E-05	7.8889E-05	7.8847E-05	7.8479E-05	7.8359E-05
^{245}Cm	2.0200E-05	1.9678E-05	1.9613E-05	1.9635E-05	1.9913E-05
^{246}Cm	1.0443E-05	1.0371E-05	1.0361E-05	1.0367E-05	1.0410E-05
Zr	7.2802E-03	7.2802E-03	7.2802E-03	7.2802E-03	7.2802E-03
a)Mo	8.1524E-04	1.0174E-03	1.0697E-03	9.4870E-04	6.6172E-04

a) representative for pseudo fission product

The nominal power and temperatures of the oxide core are identical to those of the metallic core (see Table 2.15) except for the average fuel temperature. The average fuel temperature of the oxide fuel is assumed to be 1027°C. The design parameters of the driver, radial reflector, radial shield, and control subassemblies are provided in Tables 2.24 to 2.27, respectively. Data for the nominal operating condition are presented and were calculated by accounting for the effects of thermal expansion and irradiation swelling from the fuel fabrication state. At the fabrication state, the fuel pin and control rod are helically wrapped with wire for accommodating the coolant flow, but the wire-wrap has been smeared with the cladding in order to simplify the cladding geometry. Irradiation-induced swelling of the oxide fuel is ignored and it is assumed that the fuel pellet contacts the cladding with 85% theoretical density oxide fuel.

Figures 2.13 to 2.16 show the schematics of the driver, radial reflector, radial shield and control subassemblies, respectively, and the volume fractions at the nominal operating condition are provided in Table 2.28. For all subassemblies, the duct and cladding is made of HT-9.

Figure 2.12. Radial core layout of 1000 MWth oxide-fuel core
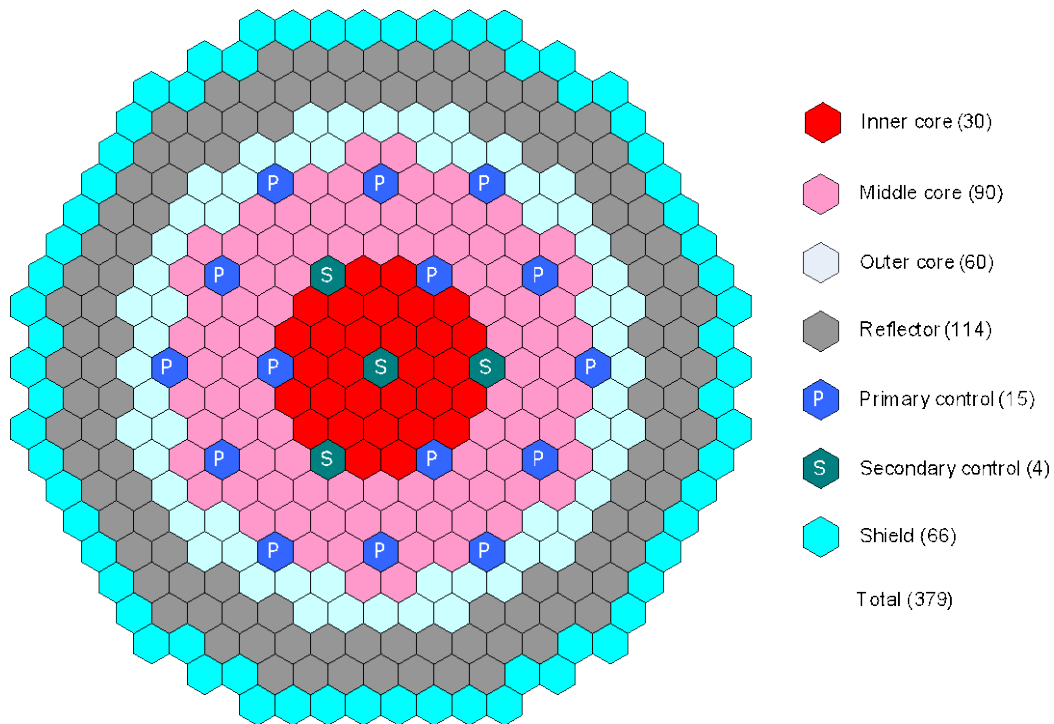
Table 2.24. Parameters for driver subassembly of 1000 MWth oxide core

	Unit	Operating state
Overall length of subassembly	cm	480.20
• Lower structure		35.76
• Lower reflector		112.39
• Active core height		114.94
• Gas plenum		172.41
• Upper structure		44.70
Subassembly pitch, cm	cm	16.2471
Subassembly duct outer flat-to-flat distance	cm	15.8123
Subassembly duct wall thickness	cm	0.3966
Number of fuel pins		271
Outer radius of cladding	cm	a) 0.3928
Inner radius of cladding	cm	0.3322
Fuel pellet radius	cm	0.3322

a) Cladding outer radius has been slightly increased to compensate
   for the smearing of the wire-wrap with the cladding.

Table 2.25. Parameters for radial reflector subassembly of 1000 MWth oxide core

	Unit	Operating state
Overall length of subassembly • Lower structure • Lower reflector • Radial reflector • Upper structure	cm	480.20 35.76 112.39 287.35 40.70
Subassembly pitch, cm	cm	16.2471
Subassembly duct outer flat-to-flat distance	cm	15.8123
Subassembly duct wall thickness	cm	0.3966
Number of fuel pins		91
Rod radius	cm	0.7756

Table 2.26. Parameters for shielding subassembly of 1000 MWth oxide core

	Unit	Operating state
Overall length of subassembly • Lower structure • Lower reflector • Radial shield • Upper structure	cm	480.20 35.76 112.39 287.35 40.70
Subassembly pitch, cm	cm	16.2471
Subassembly duct outer flat-to-flat distance	cm	15.8123
Subassembly duct wall thickness	cm	0.3966
Number of fuel pins		19
Outer radius of cladding	cm	1.6794
Inner radius of cladding	cm	1.4277
Absorber radius	cm	1.4277

Table 2.27. Parameters for control assembly of 1000 MWth oxide core

	Unit	Operating state
Overall length of subassembly • Lower structure • Lower reflector • Absorber • Empty duct	cm	480.20 35.76 112.39 119.97 212.08
Subassembly pitch, cm	cm	16.2471
Subassembly duct outer flat-to-flat distance	cm	15.8123
Subassembly duct wall thickness	cm	0.3966
Interior duct outer flat-to-flat distance	cm	14.2140
Interior duct wall thickness	cm	0.3966
Number of fuel pins		7
Outer radius of cladding	cm	[a] 2.3606
Inner radius of cladding	cm	2.2890
Absorber radius	cm	2.2890

a) Cladding outer radius is increased to compensate for the smearing of the wire-wrap.

Table 2.28. Volume fractions of 1000 MWth oxide core (%)

Region		Coolant	HT-9	Fuel	Natural B_4C	Enriched B_4C
Lower structure		Homogeneous mixture of 30% SS-316 and 70% Sodium				
Lower reflector		33.27	66.73			
Upper structure		33.27	66.73			
Driver	Active core	33.27	25.64	41.09		
	Gas plenum	33.27	25.64			
Radial reflector		15.50	84.50			
Radial shield		17.10	29.68		53.22	
Absorber in control subassembly		28.83	20.77			50.40
Empty duct in control subassembly		90.74	9.26			

Each driver subassembly contains 271 fuel pins arranged in a triangular pitch array. The fuel and coolant volume fractions are 41% and 33%, respectively. The lower structure is assumed to be a homogeneous mixture of sodium (70%) and SS-316 (30%), and the lower reflector consists of 271 solid HT-9 pins. For simplicity, the upper structure is assumed to be identical to the lower reflector.

The design parameters of the reflector, shield, and control subassemblies are identical to those of the metallic core except for the length of the reflector pin, shield pin and absorber pins: the lengths are increased because of the taller active core height of the oxide core compared to the metallic core height.

Figure 2.13. Schematics of driver subassembly of 1000 MWth oxide core
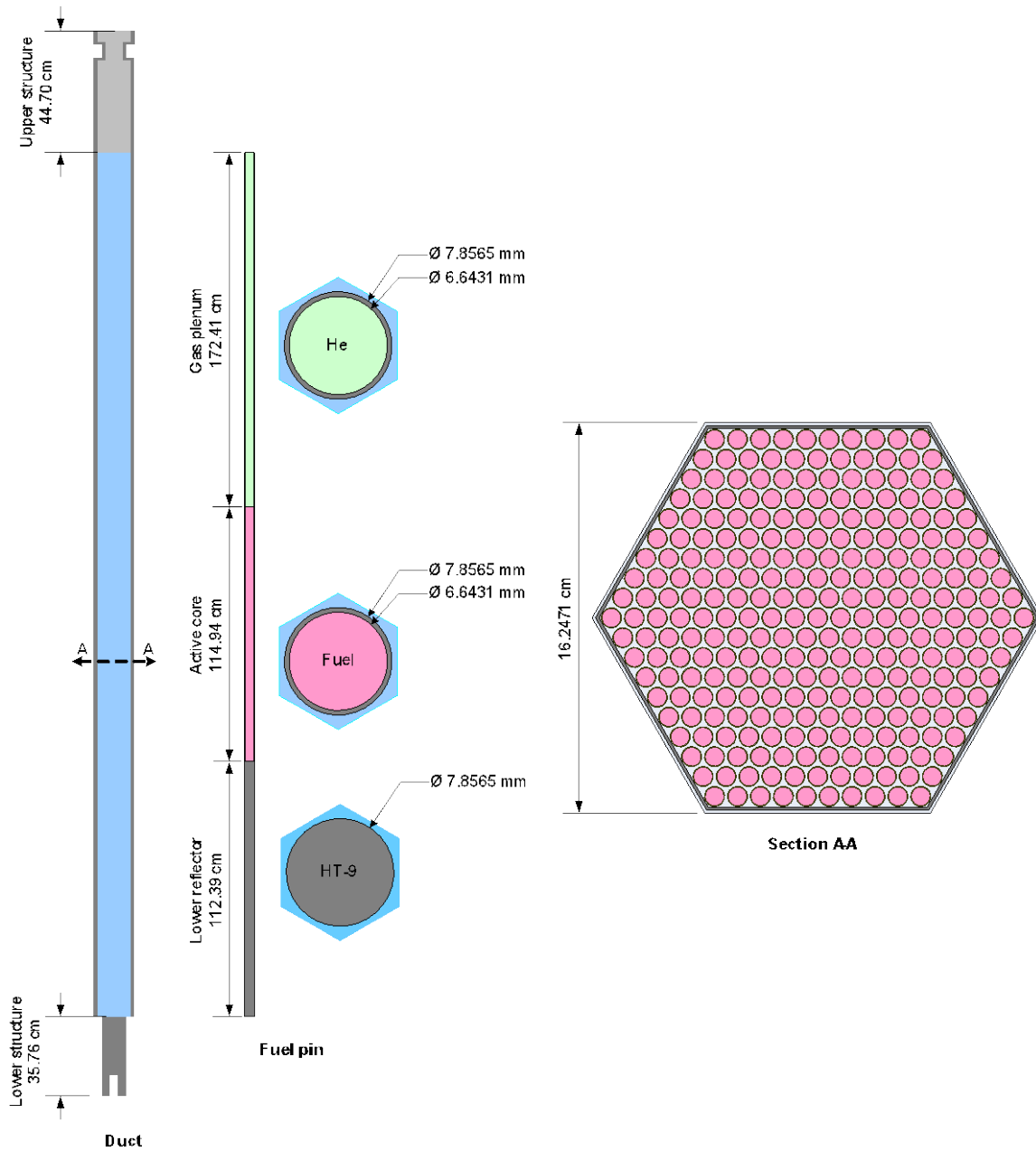
Figure 2.14. Schematics of radial reflector subassembly of 1000 MWth oxide core
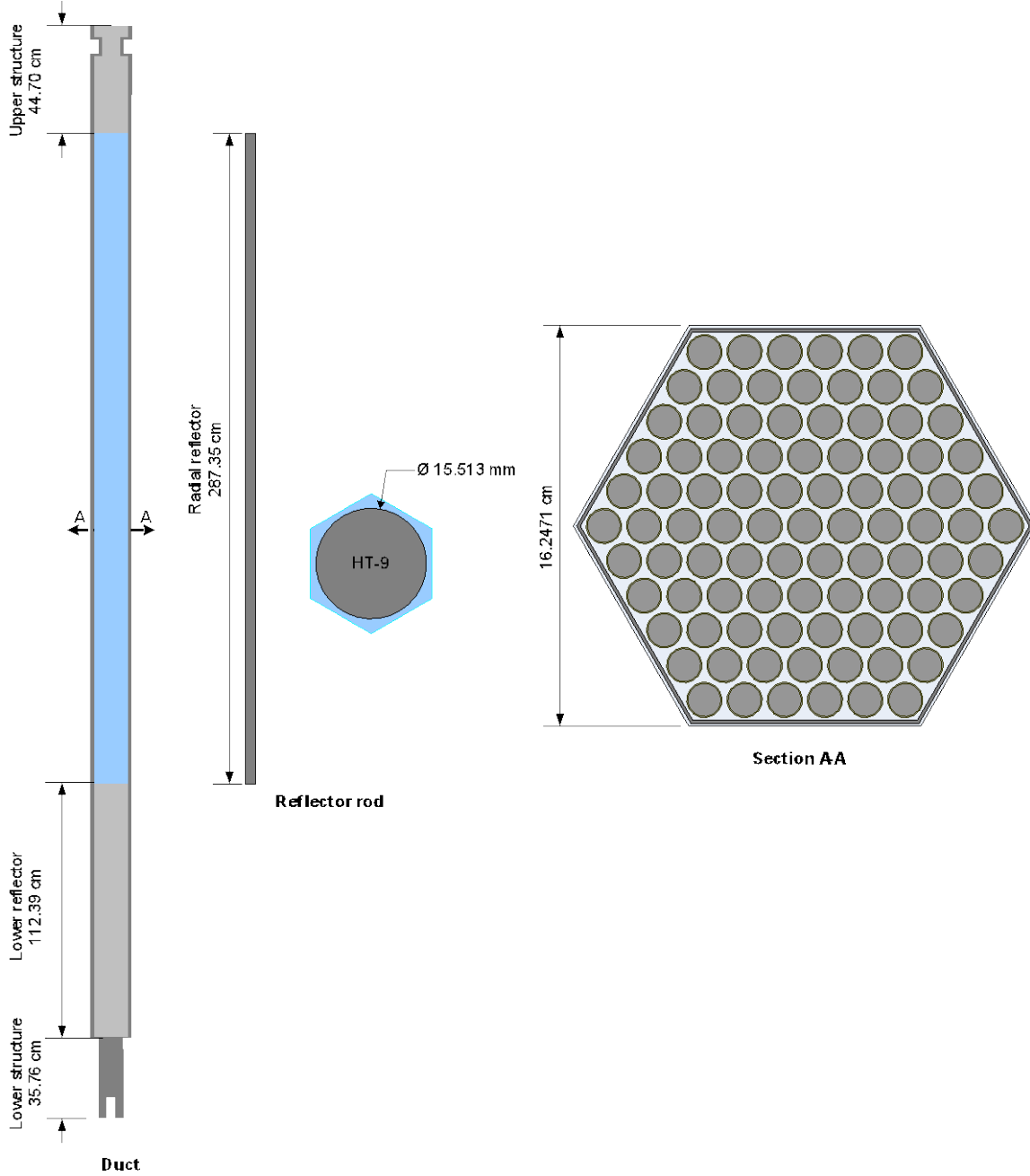
Figure 2.15. Schematics of radial shield subassembly of 1000 MWth oxide core
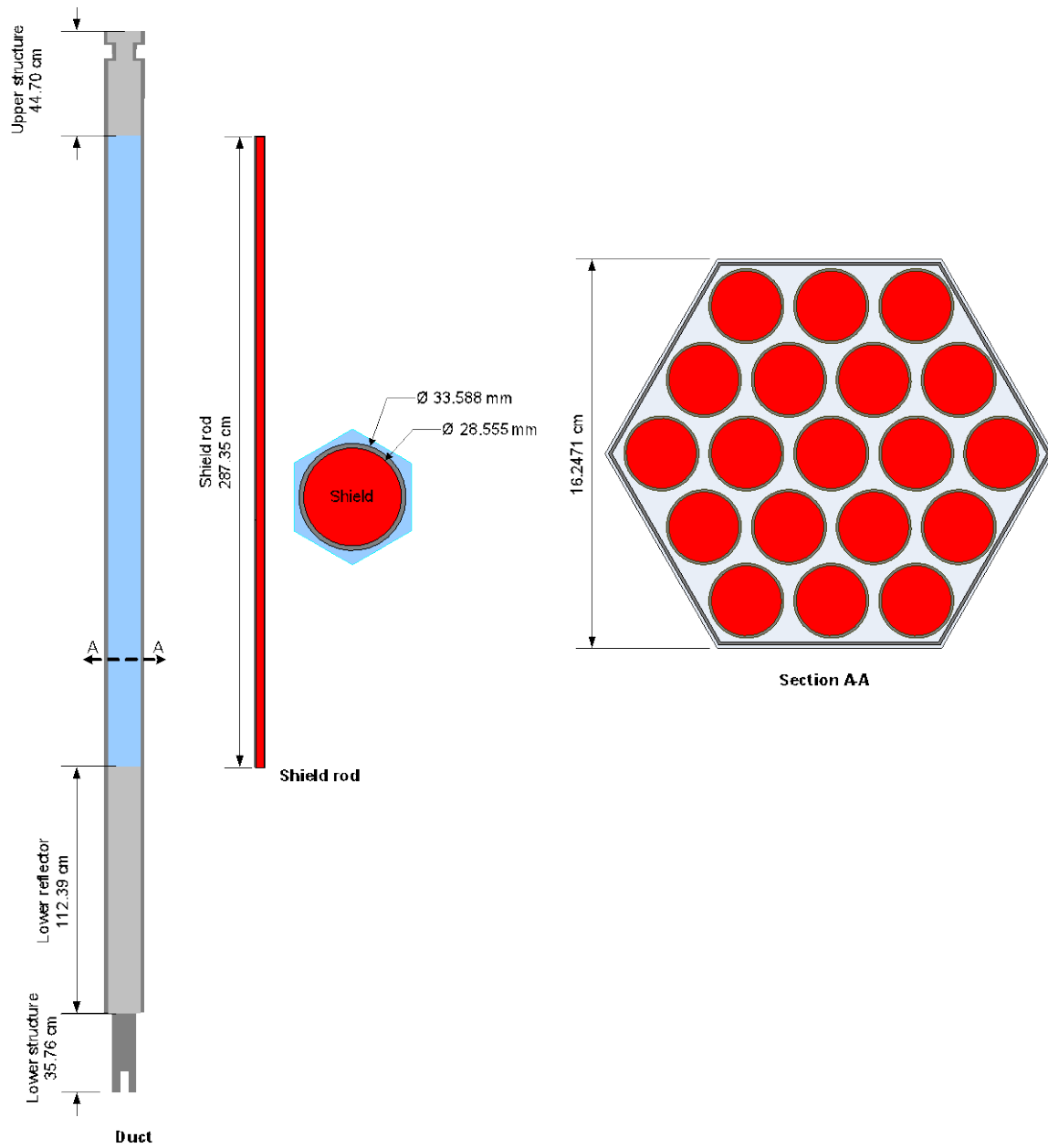
Figure 2.16. Schematics of control subassembly of 1000 MWth oxide core

Empty duct
97.14 cm

Control absorber
119.97 cm

Ø 47.2126 mm
Ø 45.7801 mm

Absorber

A   A

Empty duct
114.94 cm
(active core)

Lower reflector
112.39 cm

Lower structure
35.76 cm

**Control Rod Assembly
(when fully withdrawn)**

Subassembly duct
Interior duct

14.2140 cm

Section A-A
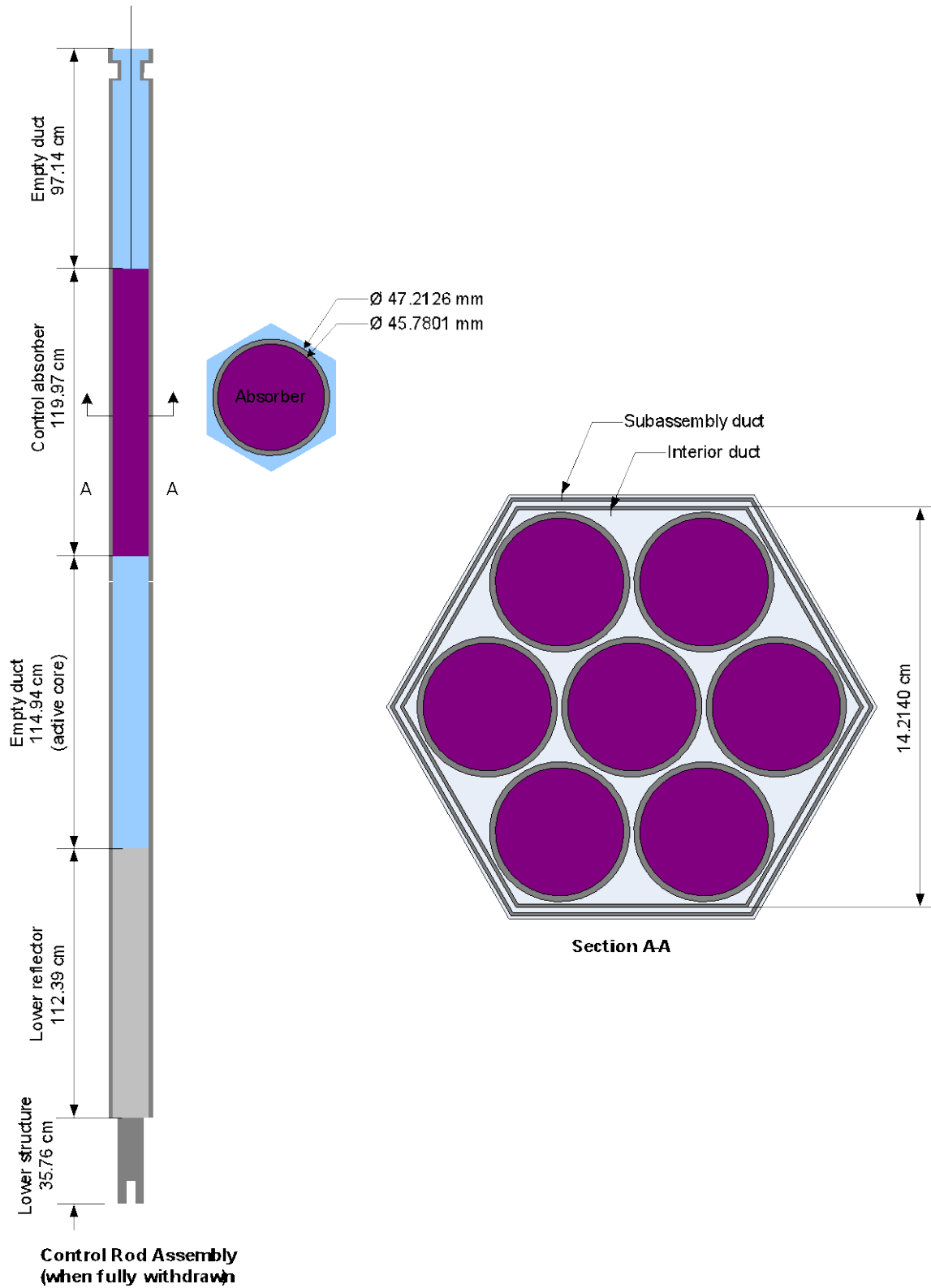
2.1.2.4 Material description of oxide core

The fuel compositions are obtained from the reference ABR oxide core data at the beginning of equilibrium cycle (BOC). For the reference ABR oxide core concept, the equilibrium cycle was determined by recycling all discharged TRU. For external make-up feed, TRU recovered from LWR used nuclear fuel is assumed. At the equilibrium cycle, the TRU conversion ratio is ~0.7 and cycle length is 328.5 days with full power operation.

The variation of fuel composition in the irradiated core is simplified. The active core is axially divided into five zones and uniform fuel composition is assumed in each zone. Thus, 15 different fuel compositions are provided in this benchmark: five each for the inner, middle, and outer cores, respectively. A simplified fission product model is also adopted with a pseudo fission product. Natural molybdenum is used to represent the fission products (pseudo fission product).

The number densities of coolant and structural materials are identical to those of the metallic core (see Table 2.21). The fuel pin compositions for the inner, middle and outer cores at BOC are provided in Tables 2.29 to 2.31, respectively. All data are obtained for the nominal operating condition by adjusting for the effects of thermal expansion.

Table 2.29. Number densities of inner core fuel pin, 1000 MWth oxide core, BOC (atoms/barn-cm)

Nuclide	Upper boundary from active core bottom (cm)				
	22.99	45.98	68.96	91.95	114.94
^{234}U	1.6447E-06	1.5173E-06	1.4786E-06	1.5459E-06	1.7187E-06
^{235}U	2.2148E-05	1.9773E-05	1.9063E-05	2.0326E-05	2.4028E-05
^{236}U	2.7420E-06	3.0518E-06	3.1560E-06	2.9636E-06	2.3408E-06
^{238}U	1.5602E-02	1.5263E-02	1.5155E-02	1.5342E-02	1.5804E-02
^{237}Np	2.8455E-05	2.7231E-05	2.6699E-05	2.7645E-05	3.0062E-05
^{236}Pu	2.6787E-10	3.0567E-10	3.1027E-10	3.0165E-10	2.6100E-10
^{238}Pu	1.0478E-04	9.9425E-05	9.7979E-05	1.0044E-04	1.0650E-04
^{239}Pu	1.7966E-03	1.7969E-03	1.7950E-03	1.7977E-03	1.7949E-03
^{240}Pu	1.2659E-03	1.2398E-03	1.2352E-03	1.2427E-03	1.2665E-03
^{241}Pu	2.0302E-04	2.0015E-04	2.0069E-04	1.9942E-04	1.9665E-04
^{242}Pu	2.7492E-04	2.6951E-04	2.6801E-04	2.7060E-04	2.7751E-04
^{241}Am	1.0157E-04	9.2311E-05	8.9477E-05	9.4499E-05	1.0862E-04
^{242m}Am	8.5597E-06	8.0757E-06	7.9066E-06	8.1989E-06	8.8286E-06
^{243}Am	9.0780E-05	8.8952E-05	8.8520E-05	8.9254E-05	9.1126E-05
^{242}Cm	5.2317E-06	6.0295E-06	6.2924E-06	5.8156E-06	4.3648E-06
^{243}Cm	6.2354E-07	6.5464E-07	6.7759E-07	6.3601E-07	5.5773E-07
^{244}Cm	6.8704E-05	6.9053E-05	6.9488E-05	6.8673E-05	6.6685E-05
^{245}Cm	2.0198E-05	1.9681E-05	1.9724E-05	1.9628E-05	1.9641E-05
^{246}Cm	1.2227E-05	1.2189E-05	1.2198E-05	1.2182E-05	1.2175E-05
^{16}O	4.1265E-02	4.1265E-02	4.1265E-02	4.1265E-02	4.1265E-02
$^{a)}Mo$	9.9952E-04	1.3906E-03	1.5100E-03	1.3041E-03	7.9560E-04

a) representative for fission product

**Table 2.30. Number densities of middle core fuel pin, 1000 MWth
oxide core, BOC (atoms/barn-cm)**

Nuclide	Upper boundary from active core bottom (cm)				
	22.99	45.98	68.96	91.95	114.94
^{234}U	2.0465E-06	1.9126E-06	1.8732E-06	1.9406E-06	2.1162E-06
^{235}U	2.2682E-05	2.0487E-05	1.9835E-05	2.0978E-05	2.4330E-05
^{236}U	2.3109E-06	2.6280E-06	2.7334E-06	2.5427E-06	1.9463E-06
^{238}U	1.4972E-02	1.4695E-02	1.4608E-02	1.4757E-02	1.5136E-02
^{237}Np	4.0907E-05	3.8847E-05	3.8073E-05	3.9439E-05	4.3081E-05
^{236}Pu	3.4311E-10	3.9750E-10	4.0506E-10	3.9131E-10	3.3031E-10
^{238}Pu	1.2787E-04	1.2257E-04	1.2120E-04	1.2349E-04	1.2912E-04
^{239}Pu	2.0192E-03	1.9884E-03	1.9789E-03	1.9948E-03	2.0350E-03
^{240}Pu	1.4917E-03	1.4584E-03	1.4514E-03	1.4629E-03	1.4962E-03
^{241}Pu	2.3846E-04	2.3537E-04	2.3568E-04	2.3481E-04	2.3280E-04
^{242}Pu	3.3130E-04	3.2522E-04	3.2358E-04	3.2638E-04	3.3390E-04
^{241}Am	1.3318E-04	1.2228E-04	1.1897E-04	1.2476E-04	1.4113E-04
^{242m}Am	1.0409E-05	9.9923E-06	9.8445E-06	1.0094E-05	1.0571E-05
^{243}Am	1.0795E-04	1.0617E-04	1.0574E-04	1.0646E-04	1.0836E-04
^{242}Cm	5.4312E-06	6.4340E-06	6.7599E-06	6.1780E-06	4.4316E-06
^{243}Cm	6.7016E-07	6.9834E-07	7.1920E-07	6.8204E-07	6.1805E-07
^{244}Cm	7.8031E-05	7.8523E-05	7.8991E-05	7.8125E-05	7.6004E-05
^{245}Cm	2.2913E-05	2.2393E-05	2.2414E-05	2.2359E-05	2.2485E-05
^{246}Cm	1.4005E-05	1.3948E-05	1.3949E-05	1.3946E-05	1.3968E-05
^{16}O	4.1265E-02	4.1265E-02	4.1265E-02	4.1265E-02	4.1265E-02
$^{a)}$Mo	9.4050E-04	1.3135E-03	1.4238E-03	1.2352E-03	7.4992E-04

a) representative for fission product

**Table 2.31. Number densities of outer core fuel pin, 1000 MWth
oxide core, BOC (atoms/barn-cm)**

Nuclide	Upper boundary from active core bottom (cm)				
	22.99	45.98	68.96	91.95	114.94
^{234}U	2.6988E-06	2.6165E-06	2.5937E-06	2.6318E-06	2.7258E-06
^{235}U	2.3608E-05	2.2094E-05	2.1619E-05	2.2437E-05	2.4556E-05
^{236}U	1.6709E-06	1.9238E-06	2.0136E-06	1.8557E-06	1.4522E-06
^{238}U	1.3148E-02	1.3003E-02	1.2957E-02	1.3036E-02	1.3226E-02
^{237}Np	9.2076E-05	8.8023E-05	8.6593E-05	8.9074E-05	9.5114E-05
^{236}Pu	4.5834E-10	5.6008E-10	5.7870E-10	5.4614E-10	4.2758E-10
^{238}Pu	1.6474E-04	1.6257E-04	1.6222E-04	1.6271E-04	1.6393E-04
^{239}Pu	2.4843E-03	2.4268E-03	2.4096E-03	2.4387E-03	2.5140E-03
^{240}Pu	1.7818E-03	1.7561E-03	1.7505E-03	1.7595E-03	1.7854E-03
^{241}Pu	3.1516E-04	3.1113E-04	3.1085E-04	3.1111E-04	3.1325E-04
^{242}Pu	4.1709E-04	4.1260E-04	4.1141E-04	4.1341E-04	4.1866E-04
^{241}Am	2.1009E-04	1.9871E-04	1.9509E-04	2.0133E-04	2.1720E-04
^{242m}Am	1.2218E-05	1.2292E-05	1.2303E-05	1.2272E-05	1.2020E-05
^{243}Am	1.2806E-04	1.2703E-04	1.2682E-04	1.2717E-04	1.2818E-04
^{242}Cm	5.2929E-06	6.4415E-06	6.8371E-06	6.1466E-06	4.3903E-06
^{243}Cm	6.9679E-07	7.1777E-07	7.3352E-07	7.0640E-07	6.7018E-07
^{244}Cm	8.1967E-05	8.2744E-05	8.3252E-05	8.2346E-05	8.0531E-05
^{245}Cm	2.3635E-05	2.3305E-05	2.3329E-05	2.3275E-05	2.3406E-05
^{246}Cm	1.3986E-05	1.3948E-05	1.3948E-05	1.3947E-05	1.3970E-05
^{16}O	4.1265E-02	4.1265E-02	4.1265E-02	4.1265E-02	4.1265E-02
$^{a)}$Mo	7.0138E-04	9.6980E-04	1.0490E-03	9.1486E-04	5.7735E-04

a) representative for fission product

2.2 Expected results

The following results are expected at the beginning and end of cycle:

- core multiplication factor;

- sodium void worth;

- Doppler constant;

- effective delayed neutron fraction (β_{eff});

- average nuclide masses per each core.

The expected heavy metal nuclides are identical to those listed in Table 2.9 or Table 2.23. The depletion of the structural materials including boron is ignored in this benchmark.

The end of cycle is defined by the core state after one cycle irradiation time, corresponding to:

- 410 days with full nominal power rating for large oxide core (MOX-3600);

- 500 days with full nominal power rating for large carbide core (CAR-3600);

- 328.5 days with full nominal power rating for medium metallic and oxide cores (MET-1000 and MOX-1000), which is equivalent to one-year cycle length with 90% capacity factor.

The sodium void worth is defined by the reactivity change between the sodium voided and nominal states such as:

$$\Delta\rho = \rho_{void} - \rho_{nominal} \text{ ,} \tag{1}$$

where the subscripts *void* and *nominal* indicate the sodium voided and nominal states, respectively. In this benchmark, the sodium voided state is defined by voiding all sodium in the active core, which contains the inner, middle (if defined), and outer cores radially and the axial locations are defined in Figures 2.2, 2.4, 2.8, and 2.13.

The Doppler constant is defined by:

$$K_D = \frac{\rho_{high} - \rho_{nominal}}{\ln 2} \text{ ,} \tag{2}$$

where the subscript *high* indicates the perturbed core state that the fuel temperature is a factor of two of that of the nominal fuel temperature.

3. Participants, codes and data

N.E. Stauff, L. Buiron

Eleven participants contributed to the benchmark, providing a total of 31 distinct calculation methodologies for the analysis of the four SFR cores proposed. The calculation methodologies employed by the participants are presented below and summarised in Table 3.1. A more complete description of the participants and methodologies is provided in Appendix A.

3.1 Participants

Eleven institutions from different countries (ANL, CEA of Cadarache, CEA of Saclay, CER-EK, ENEA, HZDR, IKE, JAEA, SCK•CEN, KIT, UIUC) provided 31 sets of results, including the core multiplication factor, isotopic composition evolution, kinetics parameters, reactivity feedbacks, and power distributions.

3.2 Calculation methodologies

Different nuclear data libraries were employed in this work. Fourteen (14) calculations used the JEFF-3.1 [7] library (or updated versions), nine used the ENDF/B-VII.0 [8,9] library (or updated versions), two used the ENDF/B-VI.8 [10] library and six used the JENDL-4.0 library [11]. Among the 31 methodologies employed, 14 used a stochastic (Monte Carlo) approach and 17 used a deterministic approach:

- Multi-group deterministic approach: this is a typical two-step process based on the fundamental mode approximation. The multi-group cross-sections are generated from lattice calculations using a representative super pin-cell, subassembly, or simplified core geometry and the whole-core analysis is followed by solving the neutron flux equations using the multi-group cross-sections that were obtained from the first step lattice calculations. There are several variations in the lattice calculations depending on the treatment of the self-shielding effect using a homogeneous and heterogeneous cell (which indicates subassembly in this study) models.

- Stochastic approach: this is known as the Monte Carlo method, which traces the individual neutron history from the birth to disappearance in the core and evaluates the core performance parameters by handling the numerous neutron histories stochastically. This approach allows the accurate representation of continuous-energy nuclear data and treatment of heterogeneity effects and complex geometries, but it requires the tracking of a lot of neutron histories in order to obtain results with rather low uncertainties.

For stochastic calculation, the uncertainty is typically lower than 10 pcm on k-effective and 15 pcm on reactivity effects. For deterministic calculation, the convergence criteria are typically less than 1 pcm. Such small uncertainty will not affect the comparison performed. This is why this information is not further detailed in this document.

It should be noted that the benchmark was intended to be performed with homogeneous cell (subassembly) models. However, both the homogeneous and heterogeneous cell models

were provided in the benchmark definition (see Chapter 2 or [1]). Seventeen (17) calculations used the heterogeneous cell model and 14 used the homogeneous cell model. Some participants provided both results from the stochastic approaches with the homogeneous and heterogeneous cell models. Some deterministic approaches adopted both cell models, for example, the broad-group cross-sections were generated from the heterogeneous cell model and the core calculations were conducted using the homogeneous cell model. Some deterministic approaches also employed the "heterogeneous equivalence method" [12] to take into account the very high coupling of the heterogeneous control rod structure to the surrounding core. For participants using a deterministic approach, the main lattice options are the following:

- Cell description:

  – Homogeneous cell model: in this model, each subassembly is divided into several axial cells and each cell is homogenised into a single medium and the average medium densities relative to their volume fractions are used in the lattice calculation to generate the broad-group cross-sections. It means that only energy-dependent self-shielding and buckling search (or source calculation), and cross-section group collapsing are conducted in the lattice calculation.

  – Heterogeneous cell model: in this model, the fuel pin, cladding, and structural materials in each subassembly are explicitly treated for self-shielding, buckling search (or source calculation) and flux resolution. The geometrical description in a heterogeneous cell model could be 1D cylindrical, 2D hexagonal or Cartesian or 2D RZ model of the subassembly or the whole core.

- Neutron energy group structure:

  – Fine group: the energy scheme used for Boltzmann resolution and self-shielding is composed of large number of groups for the purpose of describing resonance behaviour with energy for significant isotopes (heavy nuclei), typically some thousands of groups.

  – Broad group: the energy scheme used is reduced compared to the previous description, generally lower than one hundred groups.

  – Combination of broad and fine group schemes: this mixed approach leads to split self-shielding treatment using a fine-group description from other ones (buckling search and average flux) to speed up the overall process.

Participants used a very diverse combination of these main options for lattice calculation. For core calculation, the geometrical descriptions are divided into homogeneous ones for deterministic codes and full heterogeneous description for almost all probabilistic codes.

Core depletion between beginning of cycle (BOC) and end of cycle (EOC) used different depletion chain for either heavy nuclei (branching ratio) and associated fission products:

- Some used explicit fission products with relevant data from evaluated files or tuned data from experiments (HZDR, ENEA, UIUC, SCK•CEN)

- Some used pseudo-fission product based on the cross-section of natural Mo (ANL, CEA-6) or of ^{92}Mo (CER-EK, CEA-7, CEA-9). This model of pseudo-fission products based on Mo (natural) was suggested for this benchmark in order to avoid the ambiguity in depletion calculations between participants.

- Others used pseudo-fission products for which capture cross-sections are representative of the whole mass distribution according to their yield (CEA, KIT).

This variety of tools and approaches is responsible for variations in the results obtained. This is why several institutions performed calculations using several methodologies to explain and quantify some of the discrepancies observed. These additional analyses assess how changes in calculation methodologies influence the results. The conclusions of these analyses are reported in Chapter 5 together with the results obtained.

- nuclear data library: ANL, CEA, SCK•CEN and UIUC performed sensitivity analyses using several nuclear data libraries;

- code used: ANL and JAEA performed sensitivity analyses using different neutronics codes, using both stochastic and deterministic approaches;

- number of neutron energy groups: CEA performed sensitivity analyses using different number of energy groups for the self-shielding calculations;

- subassembly models: CEA, JAEA and IKE performed sensitivity analyses using homogeneous and heterogeneous cell models;

- model of fission products: CEA performed calculations based on different definitions of fission products.

These additional analyses that quantify the impact of different calculation options are combined with a cross-comparison between calculations from various institutions that use similar calculation tools and options. Such across-comparison allows checking the consistency of the models used by participants. Four groups of calculations using similar options are assembled and their results, which should theoretically be identical within the same group, are compared throughout Chapter 5:

- ANL-5 and CEA-4 employ the ECCO/ERANOS code with the JEFF-3.1 library and they use a homogeneous cell model to generate broad-group cross sections from fine-group lattice calculations (but they use a different model of fission products).

- ANL-3 and IKE-2 employ a homogeneous cell model using the MCNP5 code and the JEFF-3.1 nuclear data library.

- CEA-10, SCK•CEN-2, UIUC-1, and IKE-1 employ Monte Carlo codes (TRIPOLI-4, MCNPX/ALEPH2.5, SERPENT, and MCNP5) with the JEFF-3.1 nuclear data library and heterogeneous cell models.

- ENEA, HZDR, SCK•CEN-1 and UIUC-3 employ Monte Carlo codes (MCNPX, SERPENT, MCNPX/ALEPH2.5 and SERPENT) with the ENDF/B-VII nuclear data library and heterogeneous cell models.

The results of the various calculations are summarised in Chapter 4. For consistency purposes, only one calculation per participant is defined as their "reference" calculation and will be taken into account for the calculation of the average value. The reference calculation is the best-estimate solution, for which all the results were provided. For the UIUC and SCK•CEN calculations, results for ENDF/B-VII were defined as a reference to balance the number of calculations using JEFF-3.1 and ENDF/B-VII. For the CEA, both CEA-1 and CEA-10 are reference calculations since these were performed using the deterministic approach (Cadarache) and the stochastic one (Saclay). The other CEA, ANL and JAEA results are used to identify the major sources of bias between participants.

Table 3.1. Summary of the calculation methodologies employed by the participants (the "reference" calculations are in bold)

	Lattice calculation				Core calculation				
	Library	Code	No. energy group	Cell model	Control rod heterogeneityty	Code	No. energy group	Cell model	Reference
ANL-1	ENDFB7.0	MC²-3	2082	Homogeneous	No	DIF3D/REBUS-3	33	Homogeneous	8,15,16,17
ANL-2	ENDFB7.0					MCNP5	continuous	Homogeneous	8,18
ANL-3	JEFF3.1					MCNP5	continuous	Homogeneous	7,18
ANL-4	ENDFB7.0	ECCO	1968	Homogeneous	No	ERANOS	33	Homogeneous	8,12
ANL-5	JEFF3.1	ECCO	1968	Homogeneous	No	ERANOS	33	Homogeneous	7,12
CEA-1	JEFF3.1	ECCO	1968	Heterogeneous	Yes	ERANOS	33	Homogeneous	7,12
CEA-2	JEFF3.1	ECCO	33	Homogeneous	Yes	ERANOS	33	Homogeneous	7,12
CEA-3	JEFF3.1	ECCO	33	Heterogeneous	No	ERANOS	33	Homogeneous	7,12
CEA-4	JEFF3.1	ECCO	1968	Homogeneous	No	ERANOS	33	Homogeneous	7,12
CEA-5	JEFF3.1	ECCO	33	Homogeneous	No	ERANOS	33	Homogeneous	7,12
CEA-6	ENDFB6.8	ECCO	33	Homogeneous	No	ERANOS	33	Homogeneous	10,12
CEA-7	ENDFB7.0	ECCO	33	Homogeneous	No	ERANOS	33	Homogeneous	8,12
CEA-8	ENDFB7.1	ECCO	33	Homogeneous	No	ERANOS	33	Homogeneous	9,12
CEA-9	JENDL4.0	ECCO	33	Homogeneous	No	ERANOS	33	Homogeneous	11,12
CEA-10	JEFF-3.1.1					TRIPOLI-4	continuous	Heterogeneous	7,14
CER	JEFF3.1	ECCO	1968	Homogeneous	No	KIKO3DMG	9-17	Homogeneous	7,17
ENEA	ENDFB7.0					MCNPX	continuous	Heterogeneous	8,18
HZDR	ENDFB7.0					SERPENT	continuous	Heterogeneous	8,13
JAEA-1	JENDL4.0	SLAROM-UF	70	Homogeneous	No	TRITAC	70	Homogeneous	11,22
JAEA-2	JENDL4.0	SLAROM-UF	70	Heterogeneous	Yes	TRITAC	70	Homogeneous	11,22
JAEA-3	JENDL4.0					MVP	continuous	Heterogeneous	11,23
JAEA-4	JENDL4.0	SLAROM-UF	70	Heterogeneous	Yes	CITATION	70	Homogeneous	11,22
JAEA-5	JENDL4.0					MVP/Diff.	continuous	Heterogeneous	11,23
KIT	JEFF3.1	KANEXT	350	Homogeneous	No	KANEXT	33	Homogeneous	7,24
CEN-1	ENDFB7.1					MCNPX/ALEPH-2.5	continuous	Heterogeneous	9,20
CEN-2	JEFF3.1.2					MCNPX/ALEPH-2.5	continuous	Heterogeneous	7,20
UIUC-1	JEFF3.1.1					SERPENT	continuous	Heterogeneous	7,13
UIUC-2	ENDFB6.8					SERPENT	continuous	Heterogeneous	10,13
UIUC-3	ENDFB7.0					SERPENT	continuous	Heterogeneous	8,13
IKE-1	JEFF3.1					MCNP5	continuous	Heterogeneous	7,18,21
IKE-2	JEFF3.1					MCNP5	continuous	Homogeneous	7,18,21

4. Results of the benchmark

N.E. Stauff, L. Buiron

This chapter summarises the results obtained for the two large oxide and carbide SFR cores and for the two medium metallic and oxide SFR cores. A total of 25 different calculations were performed in this benchmark to model the MOX-3600 core by eight participants, while 11 calculations were performed to model the CAR-3600 by only four participants. For the medium cores, eight participants modelled the MET-1000 core using 20 different calculations and seven participants performed 16 calculations to model the MOX-1000 core. Results of the benchmark are summarised in Tables 4.1 and 4.2 for the large oxide and carbide cores (MOX-3600 and CAR-3600) and in Tables 4.3 and 4.4 for the medium metallic and oxide cores (MET-1000 and MOX-1000). These results are also displayed in Figures B.1 to B.6.

4.1 Results for the MOX-3600 core

4.1.1 Results for reactivity effects

For the large oxide core, 25 results have been received from eight institutions. Results are summarised in Table 4.1, in which bold values refer to best-estimate calculations. Reactivity effects and neutron delay fraction are expressed in pcm (the unit of pcm is defined as $10^5 \Delta k/k^2$). At the beginning of cycle (BOC), results for the multiplication factor exhibit apparent large discrepancies, while results for the sodium void worth and Doppler constant appear to be relatively consistent.

If we take into account the reference calculations provided, the average k-effective value of MOX-3600 is 1.0138 at BOC with a standard deviation of 405 pcm. The corresponding average reactivity swing is -312 pcm/cycle with a standard deviation of 542 pcm. There is a relatively good agreement in the delayed neutron fraction ($\beta_{Effective}$) and in the Doppler constant ($\Delta\rho_{Doppler}$). The average sodium void worth at BOC is 1 937 pcm with a standard deviation of 158 pcm. The average control rod worth is 6 041 pcm at BOC with a standard deviation of 941 pcm. As the complete set of calculation relies on very diverse hypothesis, these average values hide some significant deviations, which deserve in-depth attention. The sources of these deviations have been identified as coming from the choices in modelling, the computational tools and the nuclear data and will be investigated further in Chapter 5.

The comparison of the results obtained at different institutions while using similar tools demonstrates a relatively good agreement:

- The CEA-4 and ANL-5 calculations both employ the deterministic ERANOS code with similar homogeneous models, JEFF-3.1 library, and fine-mesh self-shielding calculations. These results show very satisfactory agreement at BOC, with 106 pcm difference in the k-effective and very similar Doppler, sodium void worth and control rod worth coefficients. The variations in the delayed neutron fraction observed will be explained in Chapter 5 by the different values of delayed neutron yields (ν_d) used. The ANL-5 and CEA-4 calculations display large differences in the reactivity swing with

~550 pcm/cycle of discrepancy, which will be explained in Chapter 5 by differences in the models of fission products employed.

- The ENEA, HZDR and UIUC-3 calculations employ a stochastic analysis (Monte Carlo approach) with a detailed heterogeneous description and the ENDF/B-VII.0 nuclear data library. There is a very satisfactory agreement observed between the ENEA and HZDR results with less than 40 pcm of discrepancy in the k-effective at BOC and consistent values of sodium void worth, Doppler coefficient and control rod worth. The reactivity swing estimated at ENEA is lower by 620 pcm/cycle when compared to the HZDR. There is a much larger discrepancy between these calculations and the UIUC-3 calculation where the reactivity estimated at BOC is larger by ~850 pcm, the sodium void worth estimated is lower by 300 pcm, and the control rod worth is lower by ~1 300 pcm (this is ~25% of variation). Surprisingly, the reactivity swing estimated by UIUC-3 is consistent with the one estimated by HZDR (both calculation employ the SERPENT code). In a consistent way, it is possible to compare results of CEA-10 and UIUC-1 that also employ a stochastic analysis with a detailed heterogeneous description and the JEFF-3.1 nuclear data library. Large discrepancies are observed for the sodium void worth (400 pcm), Doppler coefficient (180 pcm) and control rod worth (1 410 pcm).

4.1.2 Results for power distribution at BOC

The participants provided the values of fuel assembly powers over the core. As each participant used its own set of isotopic energy deposition and total core power normalisation, absolute values remain quite difficult to compare. Figure 4.1 shows the deviation from the average radial power distributions integrated over the z axis in the first subassembly of each row from centre to radial reflector edge. The first assemblies in rows 1 and 4 are control rod assemblies for which the power generated are identically zero in this benchmark. Reference results at BOC obtained by the participants are consistent with less than 4% of deviation from the average value.

Figure 4.1. Discrepancies of radial power distributions compared to averages values for the MOX-3600 core at BOC

47
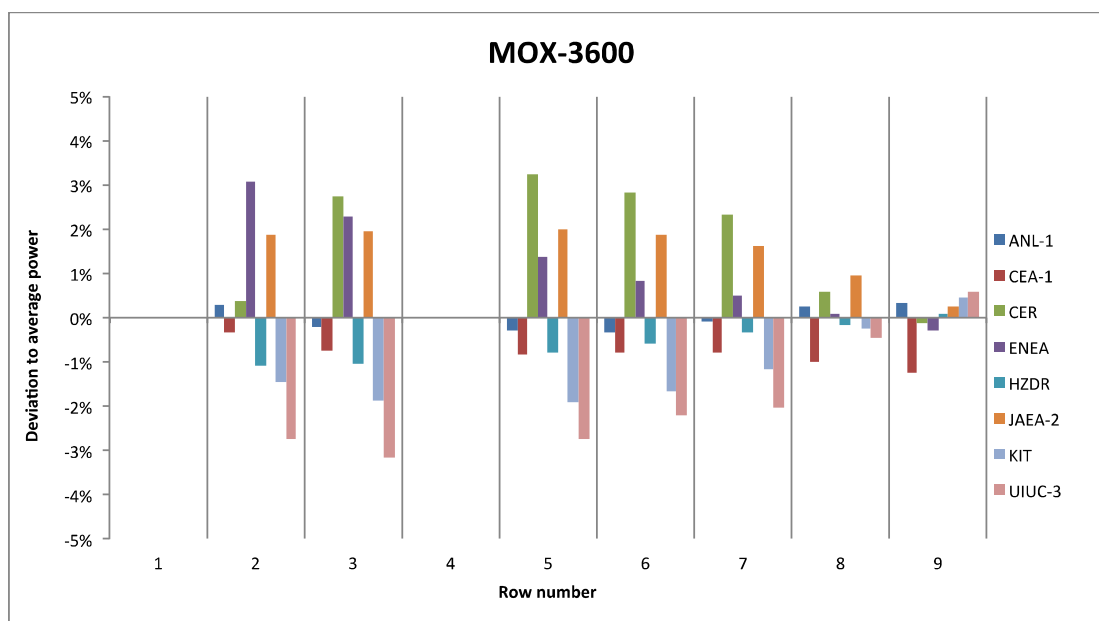
Table 4.1. Results for the MOX-3600 core

	BOC					EOC					EOC-BOC
	K_{eff}	$\beta_{Effective}$	$\Delta\rho_{Na}$	$\Delta\rho_{Doppler}$	$\Delta\rho_{CR}$	K_{eff}	$\beta_{Effective}$	$\Delta\rho_{Na}$	$\Delta\rho_{Doppler}$	$\Delta\rho_{CR}$	$\Delta\rho_{cycle}$
ANL-1	1.0077	360	2044	-915	7020	1.0144	351	2082	-866	7527	661
ANL-2	1.0075	360	2033		6952						
ANL-3	1.0137	354	2078		7045						
ANL-4	1.0050	365	2122	-988	7087	1.0143	356	2129	-943	7611	913
ANL-5	1.0104	362	2152	-975	7039	1.0152	354	2190	-937	7541	462
CEA-1	1.0162	381	1931	-971	6217	1.0136		2056	-887	6364	-253
CEA-2	1.0129	381	1831	-925		1.0119		1925	-854		-95
CEA-3	1.0172	381	1609	-909		1.0145		1723	-829		-262
CEA-4	1.0093	381	2159	-974	6882	1.0082		2265	-894	7242	-108
CEA-5	1.0118		1820	-918	6682	1.0107		1921	-839		-106
CEA-6	1.0148		1985	-856		1.0152		2033	-809		39
CEA-7	1.0064		1845	-939		1.0208		1843	-911		1406
CEA-8	1.0067		1858	-945		1.0099		1930	-859		315
CEA-9	1.0067		1978	-861		1.0215		1941	-839		1434
CEA-10	1.0197	370	1963	-982	5624	1.0170	362	2321	-834	5792	-256
CER	1.0122	392	2085	-977	7510	1.0268	384	2093	-939	8151	1400
ENEA	1.0108	352	1940	-866	5530	1.0170	353	2033	-798	5913	603
HZDR	1.0104	361	1860	-846	5831	1.0102	353				-16
JAEA-1	1.0072	362	2222	-869	6777	1.0145	355	2244	-831	7282	712
JAEA-2	1.0133	363	1948	-921	5974	1.0193	355	1977	-881	6325	574
JAEA-3	1.0139	363	2009	-904	5843						
JAEA-4	1.0104	363	1929	-923	5977	1.0164	355	1959	-883	6317	578
JAEA-5											
KIT	1.0145		2090	-863	6437	1.0148		2204	-781	6794	26
CEN-1											
CEN-2											
UIUC-1	1.0234	371	1559	-801	4214	1.0223	365	1700	-782	4176	-112
UIUC-2	1.0294	360	1696	-739	4149	1.0296	352	1824	-703	4097	15
UIUC-3	1.0193	358	1569	-803	4225	1.0201	351	1703	-765	4174	69
IKE-1											
IKE-2											
Average	**1.0138**	367	1937	-905	6041	**1.0170**	358	2059	-844	6380	312
(± SD)	0.00405	13	158	64	941	0.0047	12	179	60	1199	542

4.1.3 Results for mass balance at EOC

Figure 4.2 displays the deviation from the average total mass balance (integrated over z axis) at the end of cycle for the main actinide elements. The provided uranium and plutonium mass are quite consistent for all participants. For americium and curium elements, ANL and UIUC values are lower than for the rest of the participants. These values are strongly correlated to branching ratios and decay constant used in the depletion chain. For the MOX-3600, there is also ~25% difference in the Cm mass between the CEA-1,2,3,4,5 calculations that employ the JEFF-3.1 nuclear data library and the CEA-6,7,8,9 that employ the ENDF and JENDL libraries. This discrepancy is mostly explained by differences in the decay chain employed by the burn-up codes and by the cross-section library employed (comparing ANL-4 and ANL-5 and CEA-5 and CEA-7).

**Figure 4.2. Discrepancies of elements mass at EOC compared to
averages values for the MOX-3600 core**
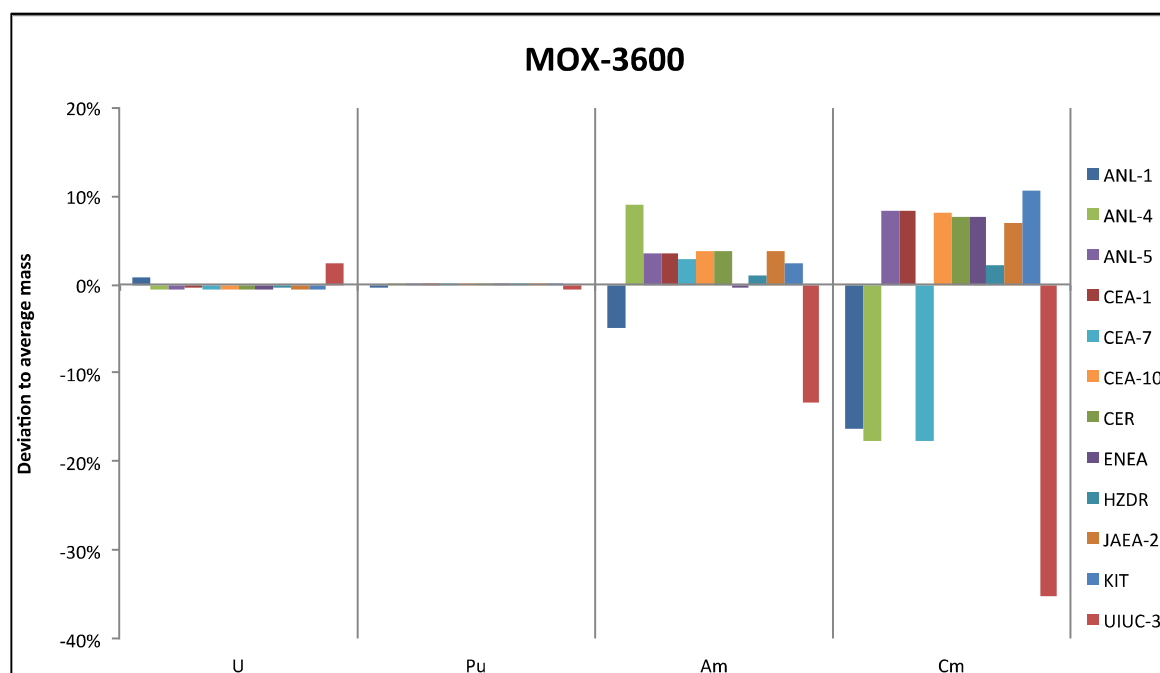
4.2 Results for the CAR-3600 core

4.2.1 Results for reactivity effects

For the large carbide core, 11 results have been received from only four institutions. Results are summarised in Table 4.2. At the beginning of cycle (BOC), results for the multiplication factor exhibit apparent large discrepancies, while results for the sodium void worth and Doppler constant appear to be relatively consistent.

The average k-effective value of CAR-3600 is 1.0090 at BOC with a standard deviation of 0.0062. There is a relatively good agreement in the delayed neutron fraction ($\beta_{Effective}$) and in the Doppler constant ($\Delta\rho_{Doppler}$). The average reactivity swing is -1 149 pcm/cycle with a standard deviation of 882 pcm. The average sodium void worth at BOC is 2 120 pcm with a 225 pcm standard deviation. The average control rod worth is 4 264 pcm at BOC with a 977 pcm standard deviation. Results UIUC (1,2,3) display large variations compared to the other participants, with much higher reactivity, lower Doppler coefficient, sodium void worth and control rod worth and this might come from an incorrect modelling of the core.

4.2.2 Results for power distribution at BOC

Figure 4.3 shows the deviation from the average radial power distributions integrated over the z axis in the first subassembly of each row from centre to radial reflector edge. The first assembly of the 5th row is a control rod for which the power generated is identically zero. Results at BOC display some significant discrepancies, especially with CER that estimate ~15% higher power than average in the centre of the reactor.

Table 4.2. Results for the CAR-3600 core

	BOC					EOC					EOC-BOC
	K_{eff}	$\beta_{Effective}$	$\Delta\rho_{Na}$	$\Delta\rho_{Doppler}$	$\Delta\rho_{CR}$	K_{eff}	$\beta_{Effective}$	$\Delta\rho_{Na}$	$\Delta\rho_{Doppler}$	$\Delta\rho_{CR}$	$\Delta\rho_{cycle}$
ANL-1	0.9991	369	2298	-990	4834	1.0145	359	2361	-928	5661	1519
ANL-2	0.9997	365	2289		4741						
ANL-3	1.0085	378	2312		4781						
ANL-4	0.9965	375	2365	-1079	4875	1.0144	364	2419	-1019	5675	1766
ANL-5	1.0043	372	2378	-1056	4853	1.0172	362	2475	-1005	5661	1270
CEA-1	1.0097	391	2122	-1048	4150	1.0147	381	2233	-949	4745	486
CEA-2											
CEA-3											
CEA-4											
CEA-5	1.0022	394	2076	-952	4715	1.0095	384	2127	-858	5477	724
CEA-6											
CEA-7											
CEA-8											
CEA-9											
CEA-10	1.0122	377	2122	-1037	3996	1.0172	368	2312	-885	4526	484
CER	1.0086	405	2306	-1121	5472	1.0351	395	2329	-1058	6401	2532
ENEA											
HZDR											
JAEA-1											
JAEA-2											
JAEA-3											
JAEA-4											
JAEA-5											
KIT											
CEN-1											
CEN-2											
UIUC-1	1.0210	382	1465	-847	2846	1.0261	371	1965	-783	2887	488
UIUC-2	1.0278	367	1911	-766	2801	1.0347	359	2135	-695	2864	652
UIUC-3	1.0156	368	1750	-841	2867	1.0231	358	1998	-796	2916	723
IKE-1											
IKE-2											
Average	**1.0090**	**382**	**2120**	**-1007**	**4264**	**1.0209**	**372**	**2247**	**-923**	**4850**	**1149**
(± SD)	**0.0062**	**16**	**225**	**104**	**977**	**0.0087**	**16**	**147**	**96**	**1315**	**882**

4.2.3 Results for mass balance at EOC

Figure 4.4 displays the deviation from the average total mass balance (integrated over the z axis) at the end of cycle for the main actinide elements. There is a very good agreement in the mass of uranium, plutonium, americium and curium elements estimated by the four institutions with less than 3% of deviation from the average value.

Figure 4.3. Discrepancies of radial power distributions compared to averages values for the CAR-3600 core at BOC
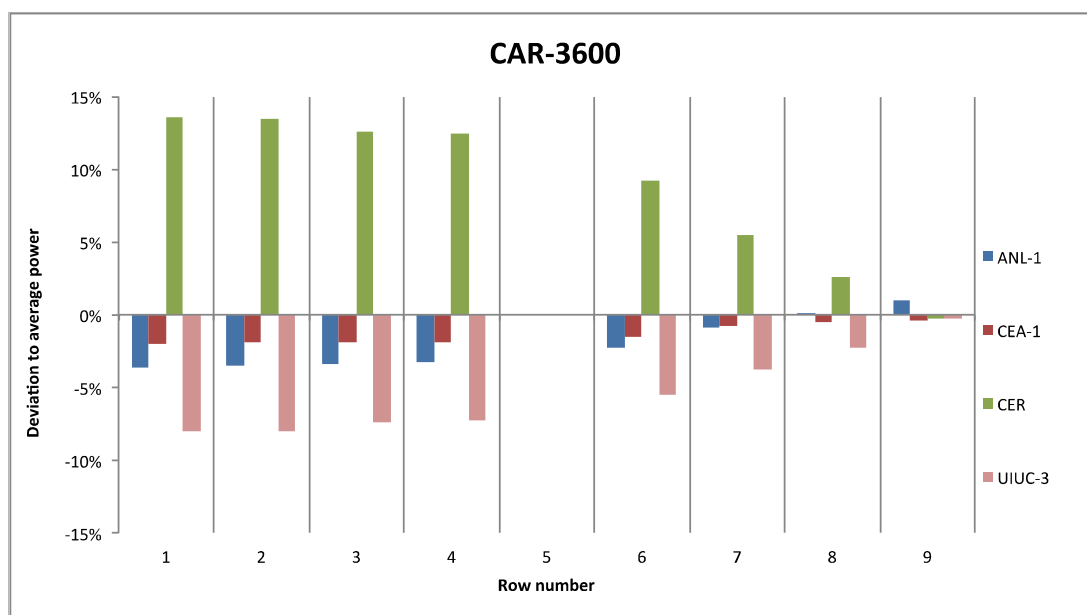
Figure 4.4. Discrepancies of elements mass at EOC compared to averages values for the CAR-3600 core
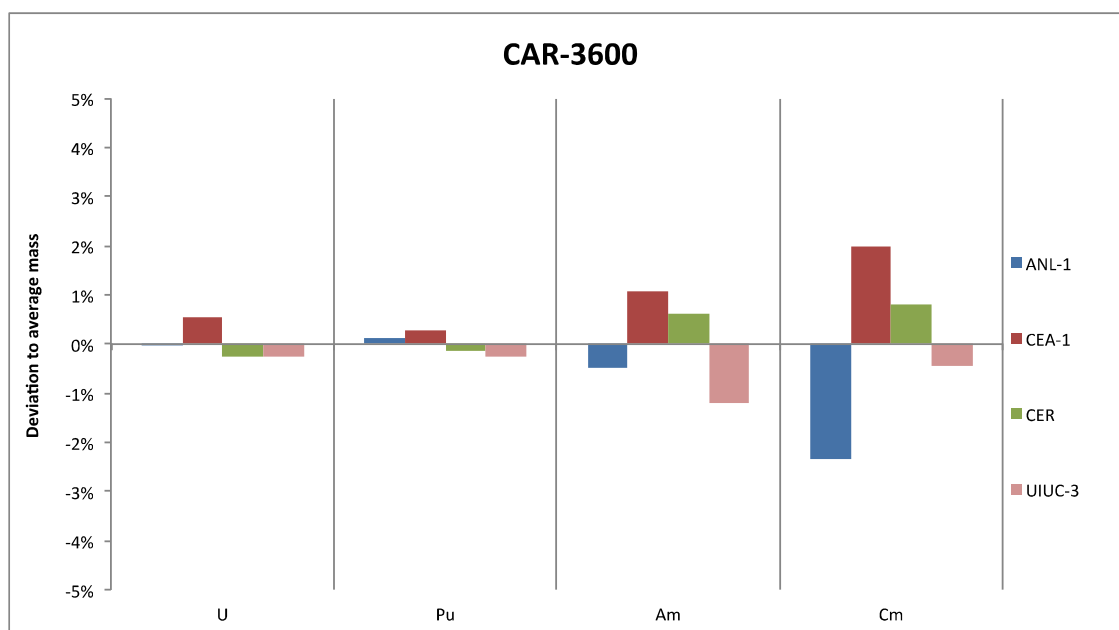
4.3 Results for the MET-1000 core

4.3.1 Results for reactivity effects

For the medium metallic core, 20 results have been received from eight institutions. Results are summarised in Table 4.3. At the beginning of cycle (BOC), results in the multiplication

factor exhibit apparent large discrepancies, while results for the sodium void worth and Doppler constant appear to be relatively consistent.

The average k-effective value of MET-1000 is 1.0355 at BOC with a 780 pcm standard deviation. There is a relatively good agreement in the delayed neutron fraction ($\beta_{Effective}$) and in the Doppler constant ($\Delta\rho_{Doppler}$). The average reactivity swing is 2 210 pcm/cycle with a 422 pcm standard deviation. The average sodium void worth is 2 024 pcm at BOC with a 406 pcm standard deviation. The average control rod worth is 19 697 pcm at BOC with a 2 087 pcm standard deviation

The comparison of the results obtained at different institutions while using similar tools demonstrates a relatively good agreement:

- The CEA-10, IKE-1 and UIUC-1 calculations employ a stochastic analysis (Monte Carlo approach) with a detailed heterogeneous description and the JEFF-3.1 nuclear data library. There is a very satisfactory agreement observed between the CEA-10 and IKE-1 results with 31 pcm of difference in the k-effective at BOC, very close values of Doppler and control rod worth, but a difference of 400 pcm in the sodium void worth. There is a much larger difference between these calculations and the UIUC-1 calculation where the reactivity estimated is lower by ~600 pcm, and the sodium void worth estimated is lower by 800 to 1 200 pcm when compared with the two other calculations. The Doppler coefficient estimated by UIUC-1 is also lower by ~100 pcm.

- The ANL-3 and IKE-2 calculations employ a stochastic analysis (Monte Carlo approach) with a simplified homogeneous description and the JEFF-3.1 nuclear data library. There is a satisfactory agreement between these two calculations, especially when comparing the k-effective at BOC, but there is ~12% (this is 250 pcm) of difference in the sodium void worth and 6% (this is 1 200 pcm) in the control rod worth.

Figure 4.5. Discrepancies of radial power distributions compared to averages values for the MET-1000 core at BOC
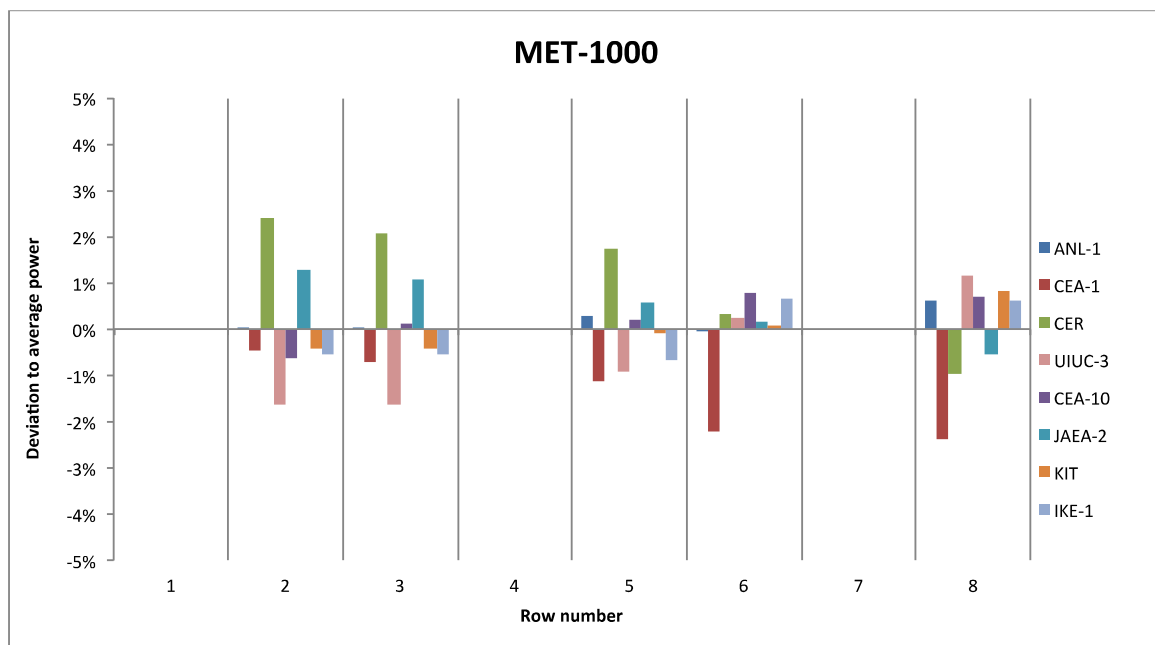
Table 4.3. Results for the MET-1000 core

	BOC					EOC					EOC-BOC
	K_{eff}	$\beta_{Effective}$	$\Delta\rho_{Na}$	$\Delta\rho_{Doppler}$	$\Delta\rho_{CR}$	K_{eff}	$\beta_{Effective}$	$\Delta\rho_{Na}$	$\Delta\rho_{Doppler}$	$\Delta\rho_{CR}$	$\Delta\rho_{cycle}$
ANL-1	1.0237	332	2267	-349	21367	1.0042	330	2348	-358	22274	-1897
ANL-2	1.0242	330	2238		21803						
ANL-3	1.0373	332	2273		22092						
ANL-4	1.0224	337	2358	-420	22384	1.0063	334	2409	-435	23296	-1561
ANL-5	1.0335	334	2356	-397	22120	1.0111	333	2471	-415	23077	-2148
CEA-1	1.0372	355	2190	-362	19335	1.0100	354	2385	-357	20063	-2594
CEA-2											
CEA-3											
CEA-4											
CEA-5	1.0310	355	2034	-383	22117	1.0055	354	2225	-362	22907	-2463
CEA-6											
CEA-7											
CEA-8											
CEA-9	1.0225		2172	-367		1.0104		2174	-388		-1173
CEA-10	1.0429	343	1858	-376	17997	1.0157	341	1995	-322	18640	-2572
CER	1.0419	357	1911	-386	23825	1.0262	366	1936	-407	24938	-1471
ENEA											
HZDR											
JAEA-1	1.0229	339	2392	-348	21554	1.0028	338	2483	-361	22357	-1955
JAEA-2	1.0289	339	2170	-375	18345	1.0081	338	2256	-389	19005	-2004
JAEA-3	1.0340	339	2164	-356	18386	1.0109	338	2309	-352	19132	-2207
JAEA-4											
JAEA-5	1.0340	339	2164	-356	18386	1.0120	338	2288	-362	19098	-2099
KIT	1.0395		2413	-339	20510	1.0150		2572	-335	21324	-2322
CEN-1											
CEN-2											
UIUC-1	1.0359	350	1032	-242	18063	1.0126	347	1118	-276	18782	-2218
UIUC-2	1.0380	335	1251	-229	17764	1.0154	333	1347	-240	18470	-2142
UIUC-3	1.0269	335	1128	-247	18224	1.0051	334	1215	-301	18944	-2103
IKE-1	1.0426	352	2257	-338	17970	1.0138	346	2461	-318	18788	-2719
IKE-2	1.0374	341	2520	-293	20856						
Average	**1.0355**	**345**	**2024**	**-347**	**19697**	**1.0123**	**344**	**2146**	**-348**	**20497**	**-2210**
(± SD)	**0.0078**	**10**	**407**	**44**	**2087**	**0.0071**	**12**	**435**	**36**	**2228**	**422**

4.3.2 Results for power distribution at BOC

Figure 4.5 shows the deviation from the average radial power distributions integrated over the z axis in the first subassembly of each row from centre to radial reflector edge. The first assemblies of row 1, 4, and 7 are control rod assemblies for which the power generated are identically zero. Results at BOC display relatively small discrepancies with less than 3% of variation between participants and the average value.

4.3.3 Results for mass balance at EOC

Figure 4.6 displays the deviation from the average total mass balance (integrated over the z axis) at the end of cycle for the main actinide elements. Results are consistent for all participants since the deviation from the average value is always lower than 1% even for americium and for curium.

**Figure 4.6. Discrepancies of elements mass at EOC compared to
averages values for the MET-1000 core**
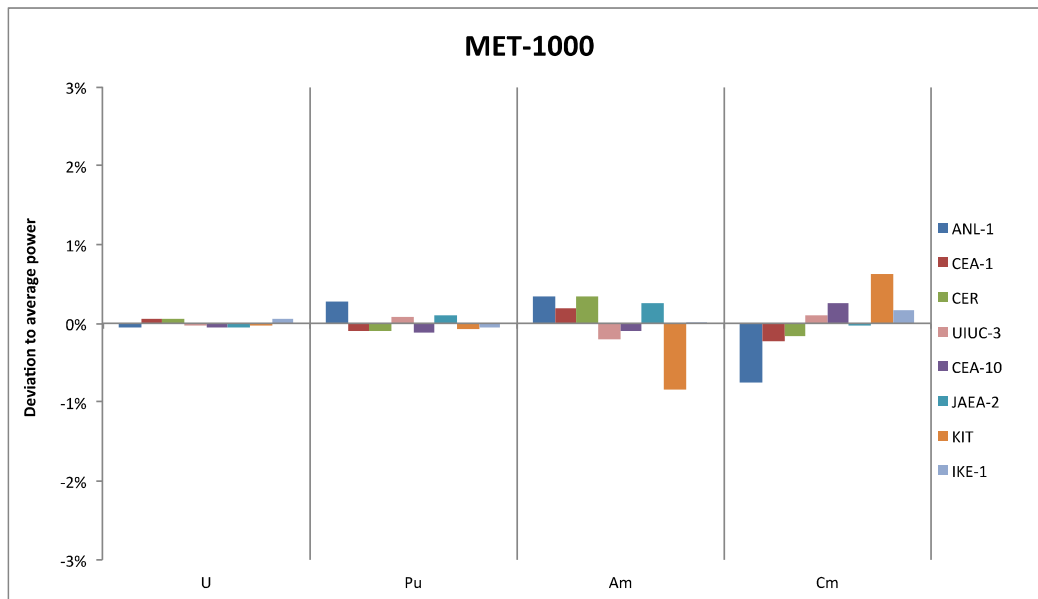
4.4 Results for the MOX-1000 core

4.4.1 Results for reactivity effects

For the medium oxide core, 16 results have been received from seven institutions. Results are summarised in Table 4.4. At the beginning of cycle (BOC), results for the multiplication factor exhibit apparent large discrepancies, while results for the sodium void worth and Doppler constant appear to be relatively consistent.

The average k-effective value of MOX-1000 is 1.0287 at BOC with a 620 pcm standard deviation. There is a relatively good agreement in the delayed neutron fraction ($\beta_{Effective}$) and in the Doppler constant ($\Delta\rho_{Doppler}$). The average reactivity swing is 1 443 pcm/cycle with a 483 pcm standard deviation. The average sodium void worth at BOC is 1 831 pcm with a 228 pcm standard deviation. The average control rod worth at BOC is 21 605 pcm with a 2 021 pcm standard deviation.

The comparison of the results obtained at different institutions while using similar tools demonstrates a relatively good agreement:

- The CEA-10, CEN-2 and UIUC-1 calculations employ a stochastic analysis (Monte Carlo approach) with a detailed heterogeneous description and the JEFF-3.1 nuclear data library. There is a very satisfactory agreement observed between the CEA-10 and CEN-2 results with 45 pcm of difference in the k-effective at BOC, very close values of Doppler and control rod worth, but a difference of 170 pcm in the sodium void worth. There is a much larger difference between these calculations and the UIUC-1 calculation where the reactivity estimated is lower by ~850 pcm. The values of sodium void worth and Doppler coefficient estimated by UIUC-1 are lower by ~110-280 pcm and 75-150 pcm, respectively.

- The UIUC-3 and CEN-1 calculations employ a stochastic analysis (Monte Carlo approach) with a detailed heterogeneous description and the ENDF/B-VII.0 nuclear

data library. There is a poor agreement between these two calculations, especially when comparing the k-effective at BOC with a difference of 542 pcm, and the sodium void worth with a difference of 234 pcm.

Table 4.4. Results for the MOX-1000 core

	BOC					EOC					EOC-BOC
	K_{eff}	$\beta_{Effective}$	$\Delta\rho_{Na}$	$\Delta\rho_{Doppler}$	$\Delta\rho_{CR}$	K_{eff}	$\beta_{Effective}$	$\Delta\rho_{Na}$	$\Delta\rho_{Doppler}$	$\Delta\rho_{CR}$	$\Delta\rho_{cycle}$
ANL-1	1.0218	323	2100	-716	23304	1.0114	321	2126	-720	24035	-1010
ANL-2	1.0223	326	2002		23106						
ANL-3	1.0303	335	2050		23428						
ANL-4	1.0197	327	2130	-858	24497	1.0139	324	2122	-868	25212	-565
ANL-5	1.0265	326	2159	-850	24217	1.0138	323	2206	-866	24987	-1225
CEA-1	1.0316	345	1922	-789	21462	1.0141	342	2060	-767	21995	-1672
CEA-2											
CEA-3											
CEA-4											
CEA-5	1.0263	345	1778	-838	24593	1.0085	342	1897	-734	25203	-1727
CEA-6											
CEA-7											
CEA-8	1.0190		1820	-783		1.0077		1889	-761		-1109
CEA-9											
CEA-10	1.0353	334	1621	-766	19431	1.0159	334	1745	-725	19904	-1847
CER	1.0346	357	1764	-819	24922	1.0288	355	1748	-844	25811	-537
ENEA											
HZDR											
JAEA-1											
JAEA-2											
JAEA-3											
JAEA-4											
JAEA-5											
KIT	1.0317		2121	-709	22209	1.0149		2243	-688	22823	-1598
CEN-1	1.0256	315	1760	-709	19795	1.0080	324	1849	-672	20317	-1703
CEN-2	1.0348	344	1789	-695	19505	1.0160	334	1932	-631	19983	-1787
UIUC-1	1.0258	337	1508	-620	19890	1.0073	335	1648	-640	20447	-1788
UIUC-2	1.0237	324	1642	-576	19834	1.0095	321	1770	-597	20308	-1382
UIUC-3	1.0200	326	1526	-606	20115	1.0023	325	1681	-610	20696	-1731
IKE-1											
IKE-2											
Average	1.0287	333	1831	-731	21605	1.0136	334	1922	-718	22226	-1443
(± SD)	0.0062	15	228	70	2021	0.0082	13	219	74	2157	483

4.4.2 Results for power distribution at BOC

Figure 4.7 shows the deviation from the average radial power distributions integrated over the z axis in the first subassembly of each row from centre to radial reflector edge. The first assemblies of row 1, 4, and 7 are control rod assemblies for which the power generated are identically zero. Results at BOC display relatively small discrepancies with less than 3% of variation between participants and the average value.

Figure 4.7. Discrepancies of radial power distributions compared to averages values for the MOX-1000 core at BOC
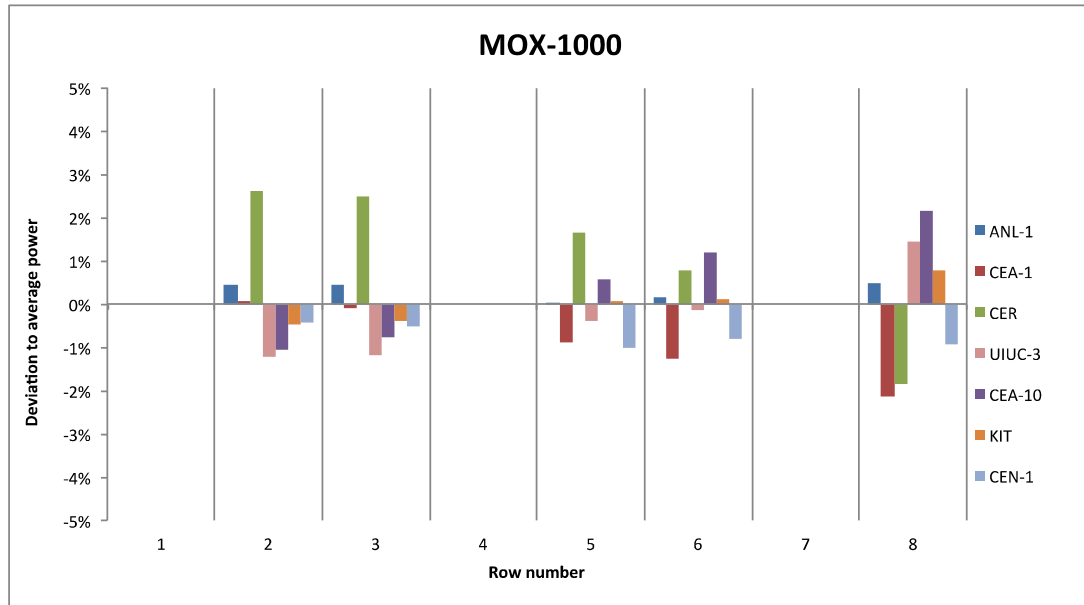
4.4.3 Results for mass balance at EOC

Figure 4.8 displays the deviation from the average total mass balance (integrated over the z axis) at the end of cycle for the main actinide elements. Results are consistent despite the ~3% of deviation observed with the UIUC calculation for the americium and curium and with the CEN calculation for the curium.

Figure 4.8. Discrepancies of elements mass at EOC compared to averages values for the MOX-1000 core
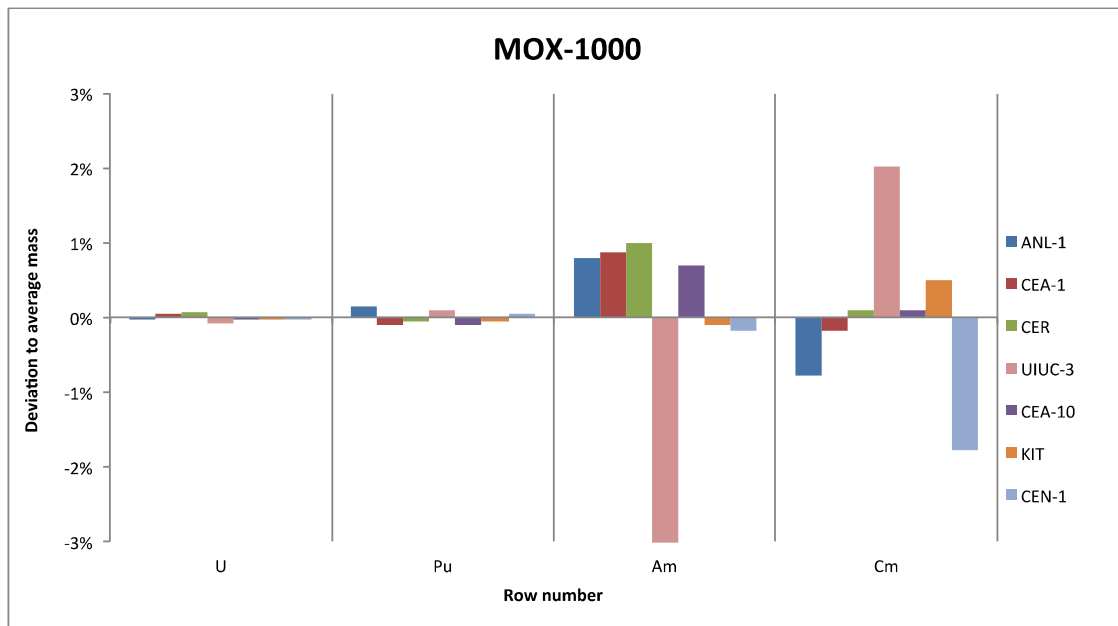
5. Analysis of the variations in the results

N.E. Stauff, L. Buiron

Relatively large variations in the results obtained were displayed in Chapter 4. While reactivity effects such as the sodium void worth coefficient, Doppler coefficient and delayed neutron fraction are observed to be in satisfactory agreement, a larger discrepancy is observed with the k-effective calculation. Some of the variations in the results observed are inconsistent within the participants and could be targeted as modelling errors. This chapter summarises the investigation of the discrepancies observed for the main reactivity effects calculated in the frame of this benchmark. This analysis uses all the 31 types of calculations, including the 11 reference calculations provided by the 11 participating institutions, and the additional calculations performed to explain differences in the results obtained. Most of the discrepancies observed are consistent and are analysed in this chapter. These are found to be mostly due to the different neutronic libraries employed (JEFF3.1, ENDF/B-VII.0 or JENDL-4.0) and to a lesser extent to the calculation methods.

5.1. Core effective multiplication factor at BOC

The calculated multiplication factors at BOC for the four cores studied are compared in Figure B.1. The average k-effective values of MOX-3600, CAR-3600, MET-1000, and MOX-1000 cores are 1.0131, 1.0082, 1.0354, and 1.0286, respectively. The k-effective values of the medium cores are higher than those of the large cores because the medium cores were designed as burner and hence have to cope with a larger reactivity swing. Since the benchmark problems were developed for the purpose of code-to-code comparison without any measurement data, it is difficult to state the accuracy of the average values; these just show the average trends of the participants' results. Thus, the discussions of this work focus on the variations of the results rather than the average values.

A significant dispersion can be observed in the results obtained. The eigenvalue estimated at BOC are apart by 2 363 pcm for the MOX-3600 core, 3 056 pcm for the CAR-3600 core, 1 926 pcm for the MET-1000 core and 1 541 pcm for the MOX-1000 core. The applied nuclear data libraries, evaluation tools (multi-group deterministic vs. continuous-energy stochastic) and core models (homogeneous vs. heterogeneous), etc. impact on the differences. Generally, the k-effective values obtained from the multi-group deterministic calculations with ENDF/B-VII for the homogeneous models are lower than the values obtained from the continuous energy stochastic calculations with ENDF/B-VI.8 for the heterogeneous models. In this chapter, the differences in the results are partly explained.

5.1.1 Impact of nuclear data libraries

Calculations performed at ANL, CEA, SCK•CEN and UIUC applied similar methodologies to different nuclear data libraries, providing information on the library-induced discrepancy over the eigenvalue estimation. Results are summarised in Table 5.1.

In general, for the BOC core state, the estimated k-effective values are consistently larger in the order of ENDF/B-VI.8, JEF-3.1, and ENDF/B-VII (or JENDL4.0).

- Calculations using the ENDF/B-VI.8 nuclear data library estimate a k-effective generally higher by 300 to 600 pcm compared to JEFF-3.1 (except for the MOX-100 core where a lower k-effective is obtained with ENDF/B-VI.8).

- Calculations using the JEFF-3.1 nuclear data library consistently lead to higher k-effective from ~500 pcm (for the MOX-3600 core) to ~1 200 pcm (for the MET-1000 core) compared to the calculations using the ENDF/B-VII.0 library [5,6].

- The k-effective results using ENDF/B-VII.0, ENDF/B-VII.1 and JENDL-4.0 nuclear data libraries are quite close, within 50 pcm of difference for the MOX-3600.

The variation calculated is not due to the energy-condensation step since a consistent discrepancy is observed using the 33-group ERANOS calculations (performed at CEA and ANL) and the continuous-energy group MCNP calculations (performed at ANL). This comparison also confirms that the observed discrepancy remains in the updated versions of JEFF-3.1 and ENDF/B-VII.

Perturbation analyses performed in [5] with ERANOS, using a consistent calculation scheme to compare the JEFF-3.1 and ENDF/B-VII.0 nuclear data libraries showed that plutonium and sodium are the two main contributors to the observed reactivity change as displayed in Table 5.2. The plutonium isotope fission cross-sections of ^{238}Pu and ^{240}Pu have a negative reactivity impact (the use of JEFF3.1 leads to larger k-effective values than ENDF/B-VII.0), while ^{239}Pu has a positive impact. The inelastic cross-section of ^{23}Na also has a significant negative impact. These results are consistent with the one based on a TRIPOLI analysis in [6]. An error cancellation of the reactivity effect was observed among the different isotopes, which partly explains the smaller k-effective change observed for the MOX-3600 when compared to the MET-1000 core.

As a partial conclusion to this chapter, it appears that nuclear data are the major source of differences in the calculation of the k-effective. The apparent differences hide significant compensations with the different plutonium isotopes being at the origin of the major differences while Na has a non-negligible impact.

Table 5.1. Nuclear data library effect on BOC k-effective values (pcm)

Calculations	Libraries	Code	MOX-3600	CAR-3600	MET-1000	MOX-1000
ANL-3 - ANL-2	JEFF3.1 - ENDFB7.0	MCNP5	610	869	1232	757
ANL-5 - ANL-4	JEFF3.1 - ENDFB7.0	ERANOS	538	774	1058	646
CEA-5 - CEA-6	JEFF3.1 - ENDFB6.8	ERANOS	-292			
CEA-5 - CEA-7	JEFF3.1 - ENDFB7.0	ERANOS	530			
CEA-5 - CEA-8	JEFF3.1 - ENDFB7.1	ERANOS	503			696
CEA-5 - CEA-9	JEFF3.1 - JENDL4.0	ERANOS	495		808	
CEN-2 - CEN-1	JEFF3.1.2 - ENDFB7.1	MCNPX/ALEPH-2.5				867
UIUC-1 - UIUC-2	JEFF3.1.1 - ENDFB6.8	SERPENT	-568	-650	-191	198
UIUC-1 - UIUC-3	JEFF3.1.1 - ENDFB7.0	SERPENT	391	525	851	561

**Table 5.2. Main isotope contribution to the reactivity discrepancy
(ENDF/B-VII.0 minus JEFF3.1)**

[pcm]	MOX-3600	CAR-3600	MET-1000	MOX-1000
^{238}U	4.1	29.2	-58.6	4.3
^{238}Pu	-258.1	-269.1	-196.5	-308.1
^{239}Pu	326.6	284.5	126.2	312.4
^{240}Pu	-177.4	-199.3	-259.7	-221.2
^{241}Pu	-80.1	-86.5	-78.6	-66.2
^{242}Pu	-22.5	-29.8	-43.7	-21.1
^{241}Am	-12.4	-13.51	-34.4	-40.5
^{243}Am	14.3	9.95	48.4	50.4
^{242}Cm	-18.4	-6.85	-38.6	-40.6
^{244}Cm	2.81	0.90	31.1	46.5
^{56}Fe	-103.4	-121.8	-72.6	-120.0
^{23}Na	-237.3	-260.0	-395.5	-278.2
^{16}O	120.1	0.3	0	101.6
Sum of discrepancies	-502	-734	-1035	-605

5.1.2 Impact of the main calculation hypothesis used in deterministic approaches

Deterministic approaches are based on some assumptions or specific hypotheses in the calculation scheme used. The main approaches are the following:

- energy group structure (number of energy-groups) for cell and core treatment such as buckling search, self-shielding and cross-section collapsing;

- geometrical description for both cell and core level. It has a significant impact on reactivity and rod worth calculations in fast reactors.

In order to quantify the impact of these modelling hypotheses at the beginning of equilibrium cycle multiplication factor and reactivity effects, CEA reviewed available cell calculation configurations (for fuel only) within the ECCO/ERANOS code package. This analysis is performed for the large oxide core (MOX-3600) and is based on the JEFF-3.1 nuclear data library (from CEA-1 to CEA-5 configurations). The associated configurations and results are described in Table 5.3.

Configuration CEA-1 gathers all modelling options corresponding to the "best estimate" (in terms of ERANOS capabilities) calculation that should give an answer close to the Monte Carlo value. Other options introduce some discrepancies because of the natural "degradation" of the quality of treatment.

For k-effective, the direct estimations of the biases associated to each fuel cell calculation approximation are the following:

- rod heterogeneity effects: 107 pcm (CEA-5 vs CEA-2);

- cell geometry description: 524 pcm (CEA-5 vs CEA-3);

- energy group: -238 pcm (CEA-5 vs CEA-4).

**Table 5.3. Impact of models and methods on large oxide core (MOX-3600)
multiplication factor using the JEFF-3.1 cross-section library**

Configuration	CEA-1	CEA-2	CEA-3	CEA-4	CEA-5
Cell geometry	Heterogeneous	Homogeneous	Heterogeneous	Homogeneous	Homogeneous
Energy group in lattice calculation	Fine group	Broad group	Broad group	Fine group	Broad group
Control rod model	Heterogeneous	Heterogeneous	Homogeneous	Homogeneous	Homogeneous
k-effective	1.01616	1.01287	1.01716	1.00934	1.01177
□ (pcm)	1590	1271	1687	925	1163

The direct difference of CEA-5 (full homogeneous and broad group solution: i.e. broad-group lattice calculation was conducted with the homogeneous cell and control rod models) to CEA-1 (full heterogeneous and fine group solution: i.e. fine-group lattice calculation was conducted with the heterogeneous cell and control rod models) gives 427 pcm (CEA-5 vs CEA-1) while the sum of individual effects gives 393 pcm (107+524-238), which leads us to conclude that potential correlations between corrections are quite limited.

The treatment of the cross-section employed also leads to significant difference in k-effective: for the MOX-3600 core, ERANOS estimates a 238 pcm higher k-effective when using a broad-group calculation compared to a fine-group calculation (CEA-4 minus CEA-5). The broad-group calculation employs direct self-shielding of cross-sections at 33 groups without a self-shielding step with high number of energy groups (1968 groups used for the fine mesh step) followed by a group condensation.

The same kind of raw analysis can be performed for energy group assumptions and for other core configurations (calculation tools and core size). Calculations performed at CEA, JAEA and IKE show the reactivity impact between the homogeneous and heterogeneous models proposed in the benchmark definition. Results of the comparison are summarised in Table 5.4.

Calculations from CEA (CEA-1 minus CEA-4), JAEA and IKE consistently show that using a heterogeneous model leads to estimating a higher k-effective by 480 pcm to 743 pcm compared to the homogeneous model. There is a good agreement between these three estimations. This difference was investigated at CEA with calculations 2, 3 and 5, and the results show that it is mainly due to the fuel cells heterogeneous treatment, while only 107 pcm is due to the control rods heterogeneity effect.

Table 5.4. Heterogeneity effect on BOC k-effective values (pcm)

Calculations	Code	Cell	CR correc.	MOX-3600	CAR-3600	MET-1000	MOX-1000
CEA-1 - CEA-4	ERANOS	hete - homo	Yes - No	665			
CEA-2 - CEA-5	ERANOS	homo - homo	Yes - No	107			
CEA-3 - CEA-5	ERANOS	hete - homo	No - No	524			
JAEA-2 - JAEA-1	MARBLE (TRITAC)	hete - homo	Yes - No	601		573	
IKE-1 - IKE-2	MCNP5	hete - homo	Yes - No			480	

Calculations performed at ANL and JAEA indicate the difference of reactivity that can be caused by the different neutronic codes used. Results are summarised in Table 5.5.

For homogeneous calculations, the results obtained with MC^2-3/DIF3D and with MCNP reach a good agreement as the difference in reactivity is within 100 pcm. The k-effective values obtained with ERANOS are consistently lower than the ones obtained with MC^2-3/DIF3D (from 130 to 270 pcm) and MCNP (from 320 to 420 pcm), with all three codes using the same nuclear data library.

The cell description impact (2D-RZ with MC^2-3 vs homogeneous with ECCO) on cross-section self-shielding is around ~200 pcm for ENDF/B-7.0 based on multiplication factor calculations (ANL-1 vs ANL-4).

For heterogeneous calculations, the k-effective values from the deterministic calculations with the MARBLE (TRIRAC) or ERANOS are lower than those from the Monte Carlo calculations with the MVP and TRIPOLI-4. Results for the metallic core exhibit larger differences (up to 531 pcm for criticality), possibly because of the harder spectrum. For the MOX-3600 core, the diffusion approximation employed in MARBLE (CITATION) leads to a lower k-effective compared to the Monte Carlo solution from the MVP calculation.

Table 5.5. Effect of evaluation methods on BOC k-effective values (pcm)

Calculations	Codes	Heterogeneous	MOX-3600	CAR-3600	MET-1000	MOX-1000
ANL-2 - ANL-1	MCNP5 - MC^2-3/DIF3D	No	-19	65	44	50
ANL-2 - ANL-4	MCNP5 - ERANOS	No	249	323	172	248
ANL-3 - ANL-5	MCNP5 - ERANOS	No	321	419	346	358
ANL-1 - ANL-4	MC^2-3/DIF3D - ERANOS	No	268	258	128	198
CEA-10 - CEA-1	TRIPOLI-4 - ERANOS	Yes	338	246	531	347
JAEA-3 - JAEA-2	MVP - MARBLE (TRITAC)	Yes	56		475	
JAEA-3 - JAEA-4	MVP - MARBLE (CITATION)	Yes	339			

5.1.3 Summary

The differences in the k-effective values obtained from each participant are indeed explained by the nuclear data library used, by the type of geometry modelled, the stochastic or deterministic approach used or the number of energy groups and the impacts are summarised below:

- higher k-effective using JEFF-3.1 rather than ENDF/B-VII.0 or JENDL-4.0 by ~600 pcm for the MOX-3600 and ~1 200 pcm for the MET-1000;

- difference between fine- and broad-mesh cell calculation (with ERANOS): broad mesh estimates higher k-effective ~240 pcm than fine mesh, estimated for the MOX-3600;

- difference between homogeneous and heterogeneous models: higher k-effective between 400 pcm and 650 pcm is estimated with heterogeneous models when compared to homogeneous models, estimated for the MOX-3600 and MET-1000. This difference (~500 pcm) is mainly due to the heterogeneous treatment of the fuel cells, while only ~100 pcm appears to be due to the control rod heterogeneity effect;

- difference between deterministic and stochastic (homogeneous): there is no noticeable difference between the results of deterministic and stochastic approaches estimated for all four cases.

As a conclusion, deterministic approaches require features to handle heterogeneity of cells and control rods correctly. Also, the slowing down process should be handled accurately with a significant number of groups (~2000 groups) in order to compare reasonably well with results obtained with stochastic methods (TRIPOLI4, MCNP5, MVP). However, a bias remains between the detailed stochastic and deterministic calculations and reaches ~531 pcm in the case of the metallic core MET-1000, which might be due to its harder spectrum that challenges the deterministic codes.

The k-effective values at BOC obtained from the multi-group deterministic calculations with ENDF/B-VII for the homogeneous core models (ANL-4) are consistently within the lowest and the results obtained from the continuous-energy stochastic calculations with JEFF-3.1 for the heterogeneous core models (CEA-10, IKE-1 or CEN-2) are within the highest values. For instance, there is a 1 926 pcm difference between two results for the MET-1000 core from ANL-4 and CEA-10. The CEA-10 calculation employs the JEFF-3.1 nuclear data library, which estimates a ~+1 100 pcm higher k-effective (displayed in Table 5.1) compared to the ENDF/B-VII.0 library employed by the ANL-4 calculation. The CEA-10 calculation also uses a heterogeneous description of the fuel assemblies, which leads to a ~+500 pcm higher k-effective (displayed in Table 5.4) compared to the ANL-4 that employs a simplified homogeneous model. Finally, the CEA-10 calculation employs a Monte Carlo code (TRIPOLI-4) that estimates between +200 and +500 pcm higher k-effective than the ERANOS code employed for the ANL-4 calculation (displayed in Table 5.5).

Table 5.6. Comparison of the discrepancies in reactivity at BOC between some CEA, JAEA and ANL calculations

		Original reactivity	Adjustment				Adjusted reactivity
			Library	Heterogeneous	Code	Bias	
MOX-3600	ANL-1	761	+538	+665	-268		1697
	JAEA-2	1314	+495				1809
	CEA-1	1590					1590
CAR-3600	ANL-1	-92	+774	+743	-258		1166
	CEA-1	964					964
MET-1000	ANL-4	2187	+1058	+665		+531	4440
	ANL-1	2315	+1058	+665	-128	+531	4440
	CEA-1	3582				+531	4113
	JAEA-3	3284	+808				4093
	CEA-10	4113					4113
MOX-1000	ANL-1	2133	+646	+665	-198	+347	3594
	CEA-1	3063				+347	3410
	CEA-10	3410					3410

For consistent comparison, the impacts of the nuclear data library, geometry model, evaluation tools on the k-effective values were adjusted and compared in Table 5.6. In this table, the adjusted values by different nuclear library (library), geometry modelling (heterogeneous), and evaluation tools (code) were obtained from Tables 5.1, 5.4, and 5.5, respectively. The (bias) value adjusts the results of the deterministic code using heterogeneous treatment to the detailed heterogeneous stochastic calculation.

The adjustment was performed by assuming that the correction factors are not correlated. Results are compared for large cores with the CEA-1 calculations and for medium cores with CEA-10 calculations. This table shows that, using consistent correction values estimated earlier, a very satisfactory agreement with less than 300 pcm of discrepancy between the ANL, the JAEA and the CEA calculations is obtained.

5.2. Burn-up evolution of the core effective multiplication factor

Figure B.1 displays a large variation in the values of k-effective at the EOC. A part of this variation is directly linked to the variation in the k-effective at BOC (already explained in the previous chapter) and another part is linked to variation in the burn-up reactivity swing[1], (difference in k-effective between the BOC and the EOC) on which this chapter focuses. For the MOX-3600 core, for instance, the average reactivity swing is 383 pcm/cycle and the reactivity varies from 1 434 pcm/cycle (CEA-9) to -262 pcm/cycle (CEA-3) depending on the assumptions used for the fission products description.

5.2.1 Impact of nuclear data libraries

The ANL-4 and ANL-5 calculations estimate a 450 to 660 pcm/cycle higher burn-up reactivity swing with ENDF/B-VII.0 compared to JEFF-3.1. These calculations employ the same code, decay chains, and models of fission products (Mo natural) but different nuclear data. Comparison of UIUC-1 and UIUC-3 displays a similar trend but with only 60 to 230 pcm/cycle of difference between the two libraries.

Different cross-section generation procedures using homogeneous/heterogeneous models also affect the reactivity swing. Calculations CEA-1, 2, 3, 4, 5 and JAEA-1 and 2, show that the homogeneous models tend to overestimate the burn-up reactivity swing by 50 to 330 pcm/cycle. The broad-mesh calculation performed at CEA-5 (compared to CEA-4) does not affect the reactivity swing in the case of the MOX-3600 core.

5.2.2 Impact of fission product models

In the case of the MOX-3600 core, the CEA estimates both the lowest (using its model of pseudo fission products) and largest (using ^{92}Mo to model the fission products) values of reactivity swing. In order to quantify the impact of the pseudo fission products (psFP) vs natural Mo on the reactivity swing, the averaged group-wise cross-section level has been compared with the JEFF-3.1 library. Figure 5.1 displays the energy dependence of the capture cross-section ratio $\sigma_{psFP}/\sigma_{Mo}$ as well as the typical flux (in arbitrary units) obtained on the inner core zone of the MOX-3600 core. This ratio is roughly equal to 2 in the relevant energy range. At BOC, the averaged one-group capture cross-section is 0.153 barns for natural Mo compared to 0.302 for pseudo fission product used by ERANOS in the CEA-1 to 5 configurations and compared to 0.050 barn for the ^{92}Mo used in the CEA-9 and CER calculations. It is no surprise then that models with ^{92}Mo have a significantly more positive reactivity drop than models using Mo and pseudo fission products. This explains why CER and CEA-9 consistently provide the lowest values of burn-up reactivity swing.

---

[1] The reactivity swing is defined as $\delta\rho cycle=(1/KeffBOC-1/K_{eff}EOC)*105$.

**Figure 5.1. Energy dependence of the capture cross-section of
pseudo fission products vs. natural Mo**
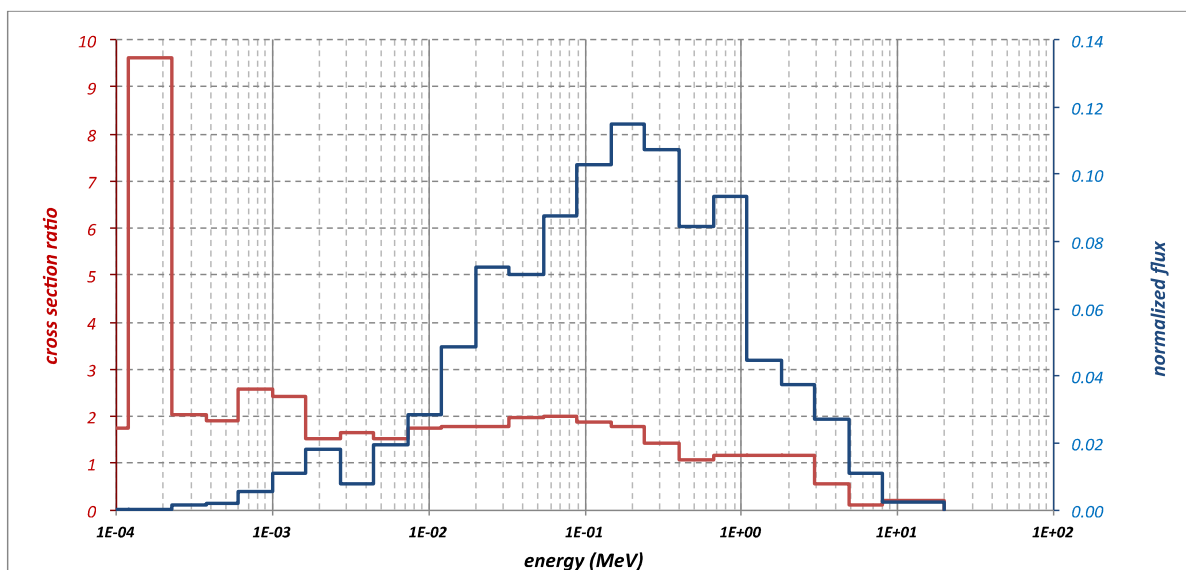
Starting from the CEA-5 configuration, two additional analyses were performed:

- The lumped fission products were replaced by natural Mo with 200% yields for all heavy nuclei (one fission is supposed to produce 2 natural Mo). This configuration aims at retrieving the reactivity swing of the ANL-5 result since it used natural Mo as lumped fission product (the impact on the reactivity swing of the fine mesh cell calculation performed with ANL-5 and not with CEA-5 can be neglected, as demonstrated by the comparison of CEA-4 and CEA-5 calculations).

This first configuration displays a cycle reactivity swing of 443 pcm, which is close to the ANL-5 result (462 pcm) using the JEFF3.1 library.

- The relative yields of the pseudo fission product in CEA-5 were changed to account for the observed capture ratio of ~2 between the Mo and the psFP (as explained with the one-group capture cross-section and displayed in Figure 5.1). This configuration aims at validating the neutronic equivalence between 1 psFP and 2 natural Mo.

The second configuration with modified psFP yields displays a reactivity swing over the fuel cycle of 587 pcm, which is ~150 pcm higher than that expected with the natural Mo model (~443 pcm in configuration 1.). As a consequence, the assumption that one psFP is equivalent to 2 natural Mo, which comes from the observation of their one-group capture cross-section, leads to a small error. For complementary information, the breakdown of the main isotopic contributors to the reactivity swing is obtained with the Standard Perturbation Theory tools available with the ERANOS code system. It can be seen that the heavy nuclei contributions are almost not impacted by the modification of the psFP yield performed to match the Mo capture cross-section. On the other hand, the contribution from the pseudo fission products is greatly impacted by the change in their yield (their contribution is divided by ~2).

Table 5.7. Isotopic breakdown of the burn-up reactivity swing

Isotopic breakdown [pcm]	CEA-5 Reference	CEA-5 with modified psFP (analysis 2)
^{235}U	-122	-121
^{238}U	696	702
^{238}Pu	-157	-145
^{239}Pu	1618	1607
^{240}Pu	21	20
^{241}Pu	-706	-700
^{242}Pu	-17	-16
^{241}Am	-10	-10
^{242m}Am	26	46
^{243}Am	-44	-65
^{242}Cm	3	-45
^{244}Cm	12	5
^{245}Cm	21	11
Sfp^{238}U	-192	-96
Sfp^{237}Np	0	0
Sfp^{238}Pu	-27	-14
Sfp^{239}Pu	-939	-473
Sfp^{240}Pu	-108	-54
Sfp^{241}Pu	-153	-77
Sfp^{242}Pu	-26	-13
Total	-106	563
HN	1340	1290
FP	-1445	-728

Variations in the reactivity drop are also caused by differences in the code used and, more specifically, the decay chain employed. First, it was verified that the heavy nuclide mass such as U, Pu, Am and Cm in the core is similar at EOC, as displayed in Figure B.5, which shows that there is no great difference in the decay chain employed. Comparison of ANL-1 and ANL-4 calculations, using similar nuclear data libraries and similar models of fission products and the different codes REBUS and ERANOS with their specific decay chain, displays a difference of 250 to 450 pcm/cycle in the reactivity swing.

5.3. Effective delayed neutron fraction

The values of delayed neutron fraction β_{eff} are displayed in Figure B.2. The averaged fraction of delayed neutron is 367 pcm for the MOX-3600 core, 383 pcm for the CAR-3600 core, 345 pcm for the MET-1000 core and 333 pcm for the MOX-1000 core. There is a reasonably good agreement within the participants in the values of delayed neutron faction since the difference observed between the maximum and minimum values for each core is lower than 40 pcm. The delayed neutron fractions generally do not change much through the irradiation cycle (reduction by ~10 pcm over the cycle). The values obtained at CEA (1 to 9) and at CER are constantly larger by ~10-25 pcm than the average values. The lowest values are obtained by ANL, CEN, JAEA, UIUC, ENEA and HZDR that all display a satisfactory agreement within 20 pcm.

The delayed neutron fraction β_{eff} obtained at CEA with ERANOS and by CER is always larger compared with the calculations at ANL. A main cause of this discrepancy comes from

different isotopic values of delayed neutron yields (ν_D) and decay constant (λ) that were used by the participants, as displayed in Table 5.8. This table reveals that the fraction of delayed neutron ($\beta_{isotope}$) significantly varies especially for the ^{238}U. The different neutron spectra of the delayed neutron play only a relatively small part in the value of β_{eff}. To demonstrate this, a calculation was performed at ANL where the different values of ν_D and λ used at ANL, CEA and CER-EK were applied to the β_{eff} calculation of the MOX-3600 core using the ERANOS core. Results in Table 5.9 confirm that most of the total difference in the β_{eff} estimated by ANL and by CEA and CER-EK is due to the ^{238}U delayed neutron yield.

Table 5.8. Values of ν_D and λ used by different participants

Delayed neutron yields, ν_Δ [pcm]									
CEA/ERANOS	1	2	3	4	5	6	7	8	**SUM**
^{238}U	4.00E+01	5.00E+02	1.80E+02	6.50E+02	1.40E+03	9.50E+02	6.10E+02	4.50E+02	**4780**
^{239}Pu	1.90E+01	1.50E+02	6.20E+01	9.70E+01	2.30E+02	2.40E+01	6.40E+01	1.10E+01	657
^{240}Pu	2.00E+01	1.90E+02	7.20E+01	1.40E+02	2.80E+02	9.40E+01	7.10E+01	2.90E+01	896
^{241}Pu	2.50E+01	2.80E+02	8.90E+01	2.70E+02	4.50E+02	2.70E+02	1.80E+02	3.90E+01	1603
ANL	1	2	3	4	5	6			**SUM**
^{238}U	6.10E+01	5.00E+02	5.80E+02	1.70E+03	1.10E+03	4.50E+02			**4391**
^{239}Pu	2.30E+01	1.50E+02	1.20E+02	2.10E+02	1.10E+02	3.30E+01			646
^{240}Pu	2.90E+01	2.30E+02	1.40E+02	3.00E+02	1.60E+02	4.90E+01			908
^{241}Pu	2.90E+01	3.60E+02	2.30E+02	5.70E+02	3.20E+02	1.10E+02			1619
CER	1	2	3	4	5	6			**SUM**
^{238}U	6.79E+01	5.49E+02	6.38E+02	1.88E+03	1.24E+03	5.02E+02			**4870**
^{239}Pu	2.38E+01	1.55E+02	1.18E+02	2.15E+02	1.12E+02	3.38E+01			657
^{240}Pu	2.98E+01	2.36E+02	1.41E+02	3.08E+02	1.68E+02	5.11E+01			933
^{241}Pu	2.95E+01	3.66E+02	2.33E+02	5.71E+02	3.23E+02	1.11E+02			1634
Decay constant, λ [s^{-1}]									
CEA/ERANOS	1	2	3	4	5	6	7	8	
All isotopes	1.20E-02	2.80E-02	4.30E-02	1.30E-01	2.90E-01	6.70E-01	1.60E+00	3.60E+00	
ANL	1	2	3	4	5	6			
^{238}U	1.40E-02	3.10E-02	1.20E-01	3.20E-01	9.10E-01	3.10E+00			
^{239}Pu	1.30E-02	3.10E-02	1.10E-01	2.90E-01	8.60E-01	2.70E+00			
^{240}Pu	1.30E-02	3.10E-02	1.20E-01	3.00E-01	8.50E-01	2.90E+00			
^{241}Pu	1.40E-02	3.00E-02	1.20E-01	3.10E-01	8.70E-01	3.00E+00			

Table 5.9. Impact of the different values of ν_D and λ used at ANL, CEA and CER-EK on the β_{eff} calculation of the MOX-3600 (at BOC) using ERANOS

β_i from	β_{eff} [pcm]		
	ANL	CEA	CER
^{235}U	5.2	5.0	5.0
^{238}U	**171.8**	**186.4**	**190.6**
^{237}Np	0.1	0.1	0.1
^{238}Pu	2.3	2.5	2.6
^{239}Pu	112.8	114.1	114.9
^{240}Pu	17.9	17.8	18.5
^{241}Pu	46.5	45.9	46.9
^{242}Pu	7.8	10.2	6.9
^{241}Am	0.2	0.2	0.3
TOTAL	364.7	382.3	385.7

5.4. Sodium void worth

The sodium void worth is defined as the reactivity change between the nominal state of the core and the voided state. In this benchmark, the voided state is obtained by voiding 100% of the sodium in the active core, including the sodium layer between the assemblies [1]. This study focuses on the comparison of the BOC values of the sodium void worth. The EOC values are consistently slightly larger than at BOC.

The values of sodium void worth calculated by the various institutions for the four SFR cores studied are compared in Figure B.3. The average values for all cores are between 5.3\$ and 5.9\$. Variations from 660 to 1 500 pcm are observed among participants. This represents a variation from 1.7\$ to 4.4\$. Large values of sodium void worth are usually observed with ANL-5, JAEA-1 and IKE-2 calculations while low values are observed by UIUC (1, 2 and 3). In this work, the values in pcm are compared instead of the values in \$ to decorrelate the variations in the sodium void worth to the variations in the delayed neutron fraction.

5.4.1 Impact of nuclear data libraries

Calculations performed at ANL, CEA, SCK•CEN and UIUC show the relative impact of the neutron data libraries used in the k-effective estimation. Employing the JEFF-3.1 or the ENDF/B-VII.0 nuclear data cross-sections leads to a similar sodium void worth (variations are within 50 pcm). The CEA and UIUC calculations show that a larger difference is obtained with the ENDF/B-VI.8 and JENDL-4.0 data libraries that leads to a sodium void worth higher by ~160 pcm compared to the JEFF-3.1 library. CEA calculations show also a large underestimation of 340 pcm of the sodium void worth value when using a broad-mesh cross-section calculation methodology (CEA-5) rather than a fine-mesh methodology (CEA-4).

5.4.2 Impact of homogeneous/heterogeneous models

Calculations performed at CEA, JAEA and IKE show that homogeneous calculations tend to overestimate the value of the sodium void worth by 200 pcm to 300 pcm. This difference is observed in the heterogeneous cross-section cell calculation step performed with ERANOS (difference between CEA-1 and CEA-4) rather than in the control rod heterogeneous treatment, which only leads to 11 pcm of difference.

5.4.3 Impact of evaluation tools

Calculations performed at ANL, JAEA and CEA show that a relatively low difference in the sodium void worth values could be explained by the use of different calculation tools. ANL estimates a variation lower than 130 pcm in the sodium void worth coefficient obtained using the MCNP5, the MC^2-3/DIF3D and the ERANOS codes, all using a homogeneous core model. For medium cores, the CEA displays a larger difference of ~300 pcm in their TRIPOLI-4 (CEA-10) and best-estimate ERANOS calculations (CEA-1).

5.4.4 Summary

Comparing results displayed in Figure B.3, it should be noted that all the heterogeneous calculations (CEA-1,3,10, ENEA, HZDR, JAEA-2,3,4,5, CEN and UIUC) provide lower values of sodium void worth, compared with the homogeneous calculations. CEA calculations employing a broad-mesh cross-section calculation (CEA-2,3,5,6,7,8,9) also provide lower values of sodium void worth. The UIUC values of sodium void worth are consistently significantly lower than the values estimated by the other participants. The difference is especially important in the case of the MET-1000 core.

5.5. Doppler constant

The values of the Doppler constant are displayed in Figure B.4. The average value of the Doppler constant calculated at BOC is -895 pcm for the MOX-3600, -1 000 pcm for the CAR-3600, -346 pcm for the MET-1000, and -730 pcm for the MOX-1000. Variations in the BOC results obtained by the participants are lower than 0.9$.

The largest values of the Doppler constant (more negative) are always obtained with the ANL-4 and ANL-5 calculations, some CEA (Cadarache) calculations, and the CER calculations. The lowest values of the Doppler constant are always obtained with the UIUC calculations (1, 2 and 3) but also with the ANL-1, HZDR, IKE and SCK•CEN calculations. Among the values of the Doppler coefficient calculated by the CEA of Cadarache with the ECCO/ERANOS code, a difference up to 120 pcm was observed for the large cores (MOX-3600 and CAR-3600). This difference was investigated for the large oxide core (MOX-3600), using perturbation calculations performed with ERANOS in order to obtain the isotopic breakdown to the Doppler reactivity effect. These isotopic contributions are compared in Table 5.10 for different cell models and neutron group structures. Table 5.10 gathers the main isotopic contribution to the reactivity breakdown integrated over space and energy domains obtained by standard perturbation theory.

The cell modelling does not affect the Doppler coefficients of most nuclides, except for ^{56}Fe and ^{238}U. Compared to the heterogeneous cell models (CEA-1 or CEA-3), the homogeneous cell models (CEA-4 or CEA-5) overestimate ^{56}Fe Doppler (more negative), but underestimate ^{238}U Doppler (less negative). Because of error cancellation between ^{56}Fe and ^{238}U, the total Doppler coefficients of the homogeneous models are comparable to the heterogeneous models.

Figure 5.2 presents the energy distribution of the ^{238}U contribution to the Doppler effect. All configurations show the same trend. The main difference for the ^{238}U contribution to the Doppler effect as a function of energy occurred around 1 keV, which corresponds to large capture resonances.

**Table 5.10. Isotopic breakdown of the Doppler reactivity effect (integral) integrated
over spatial and energy domain for parametric model and methods
using JEFF-3.1 cross-section library for the MOX-3600**

	CEA-1	CEA-3	CEA-4	CEA-5
Cell geometry	2D Heterogeneous	2D Heterogeneous	Homogeneous	Homogeneous
Energy Mesh	Fine mesh	Broad mesh	Fine mesh	Broad mesh
Contribution (pcm)				
^{23}Na	-1	0	-1	0
^{56}Fe	-8	-1	-50	-41
^{16}O	-5	0	-5	0
^{238}U	-615	-596	-583	-565
^{238}Pu	0	-1	0	0
^{239}Pu	-4	8	-2	10
^{240}Pu	-16	-19	-14	-17
^{241}Pu	-13	-14	-13	-13
^{242}Pu	-2	-2	-2	-2
Total	-666	-624	-670	-628

Figure 5.2. Energy distribution of the ^{238}U contribution to the Doppler effect for the MOX-3600
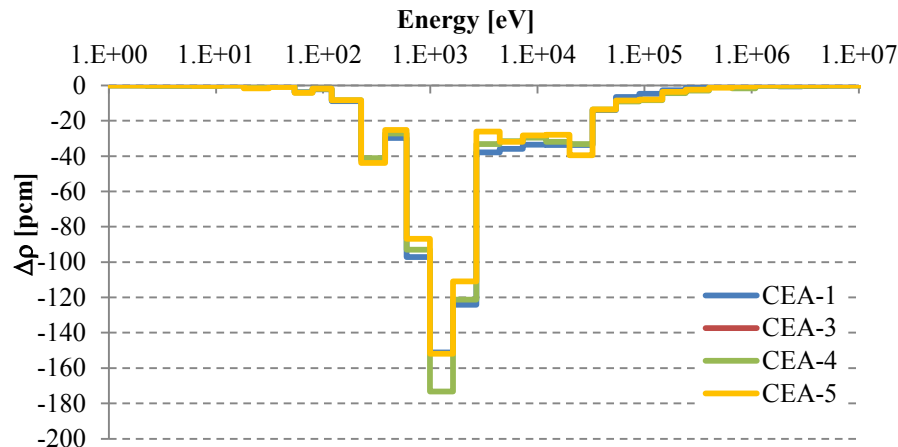
Differences in nuclear data libraries, homogeneous or heterogeneous cross-section treatment, fine- or broad-mesh cross-section calculations, all have a relatively small impact (<60 pcm) on the Doppler constant value estimated. Larger differences between 70 to 150 pcm were observed when comparing results from the ECCO/ERANOS code (ANL-4, 5) to the MC^2-3/DIF3D code (ANL-1). These discrepancies are explained by the difference in the Doppler coefficient calculation methodologies used for homogeneous medium in ECCO and in MC^2-3: only the cross-sections of the fuel elements are perturbed in the MC^2-3 calculations while both the fuel and structure cross-sections are perturbed in the ECCO calculation (for homogeneous calculations). Temperatures are given per subassembly region in ECCO/ERANOS and hence results given by heterogeneous description of the subassembly are more reliable (CEA-1).

5.6. Control rod worth

The control rod worth is calculated by inserting all the primary and secondary control rods completely in the core. The results obtained by the participants are displayed and compared in Figure B.6. The EOC values are slightly higher than the BOC values. Variations across the cycle are relatively similar, which justifies focusing only on the BOC values. The average control rod worth of the large cores is 16.6$ for the MOX-3600 and 11.3$ for the CAR-3600, respectively. The average control rod worth of the medium cores is 57.1$ for the MET-1000 and 64.8$ for the MOX-1000, respectively.

Calculations performed at ANL, CEA, SCK•CEN and UIUC display a small variation, less than 1.5%, in the control rod worth relative to the nuclear data library used. This variation is not further investigated.

Different calculation codes, on the other hand, can lead to larger differences in the results. This is demonstrated by ANL and CEA where up to 9.8% of difference in the control rod worth is obtained when comparing the ERANOS calculation (ANL-4, ANL-5, CEA-1) with MCNP (ANL-2, ANL-3) or TRIPOLI (CEA-10). Calculations employing a stochastic (Monte Carlo) approach tend to estimate lower values of control rod worth than those using a deterministic approach. This trend was also confirmed by JAEA for the MOX-3600 core.

However, the largest differences in the control rod worth are connected to the homogeneous or heterogeneous description of the cell and of the control rods. This is demonstrated by CEA calculations 1 and 4, JAEA calculations 2 and 1 and IKE calculations 1 and 2, where heterogeneous calculations provide consistently lower control rod worth by ~10-17%. The CEA-1 calculation was performed with rod heterogeneity correction using an equivalence method [25]. Macroscopic cross-sections are corrected by group-dependent factors resulting from a heterogeneous/homogeneous reactivity equivalence procedure based on perturbation tools available in the ERANOS code system [12]. As an example, Figure 5.3 displays the macroscopic cross-section for the homogeneous description of the CSD control rod medium of the MOX-3600 core and the corresponding one obtained using the equivalence procedure. The spatial screening effect of outer absorber rods leads to a reduced effective cross-section in the "low" energy domain (typically lower than 1 keV).

Figure 5.3. 33-energy group distribution of the macroscopic cross-sections of the control rods
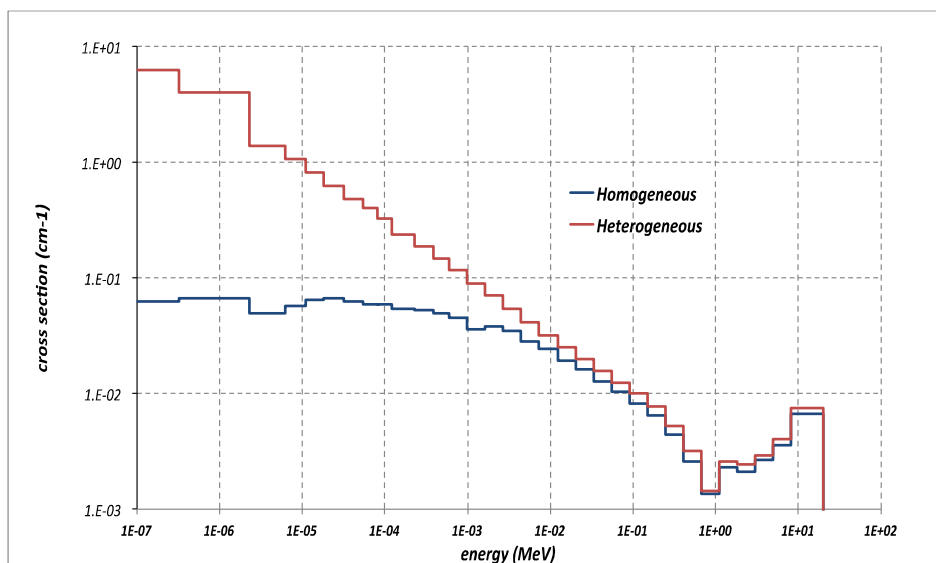
This analysis explains why heterogeneous calculations such as UIUC, CEA-1, CEA-10, JAEA-2, JAEA-3, JAEA-4, JAEA-5, SCK•CEN, ENEA, HZDR, IKE-1 values of control rod worth are consistently lower than homogeneous calculations such as ANL, CER, CEA-4, JAEA-1 and KIT. Variations between codes were also observed but are of a lower order of magnitude. However, the much lower control rod worth obtained by UIUC for the large cores MOX-3600 and CAR-3600 cannot yet be explained.

6. Conclusion

Within the activities of the Working Party on Scientific Issues of Reactor Systems (WPRS), an international collaboration was conducted to assess the core performance characteristics and reactivity feedback coefficients of several Sodium-cooled Fast Reactor (SFR) concepts with various fuel forms such as oxide, carbide and metal alloy. Four numerical benchmark cases were initially developed with large and medium core sizes in order to perform:

- neutronic characterisation of global parameters (k-effective, power and flux distributions, sodium void effect, Doppler, etc.);

- feedback coefficients evaluation, based on a common calculation methodology;

- transient calculations, with the use of previous feedback coefficient, on a few selected cases for the principal unprotected transients: unprotected transient overpower (UTOP), unprotected loss of flow (ULOF), unprotected loss of heat sink (ULOHS) and the core behaviours characterised using a matrix classification.

Eleven institutions from different countries (ANL, CEA of Cadarache, CEA of Saclay, CER-EK, ENEA, HZDR, IKE, JAEA, SCK•CEN, KIT, UIUC) provided 31 sets of results, including the core multiplication factor, isotopic composition evolution, kinetics parameters, reactivity feedbacks and power distributions.

Despite the clearly defined benchmark specifications, the apparent discrepancies between the numerical results observed were due to the use of different methodologies, evaluation neutron data library files, computation codes, and applied approximations by the different participants. Hence, the main work has focused on the analysis of these apparent discrepancies before reaching the next stages of the benchmark and finally the transient evaluation. In the present study, differences in the results obtained between participants using different methodologies and tools were systematically analysed and the origins of the discrepancies were identified:

- The nuclear data library used has a large impact on the k-effective calculation since the JEFF-3.1 library tends to estimate a higher k-effective by 500 to 1 200 pcm compared to the ENDF/B-VII and JENDL-4.0 libraries.

- The cell and control rod models (heterogeneous vs. homogeneous) employed for the lattice and core calculations impact on the k-effective, sodium void worth and control rod worth calculations: the homogeneous model underestimates the core reactivity by 400-650 pcm, overestimates sodium void worth by 200-300 pcm, and control rod worth by 10 - 17%.

- The methodology and the computation codes impact the k-effective, sodium void worth and Doppler constant. For the same cell model and neutron data library, Monte Carlo codes estimate the core k-effective higher up to ~500 pcm, as observed for the metallic core; sodium void worth obtained with stochastic calculations exhibits slightly lower values compared to deterministic codes.

- The Doppler constant estimations are similar when using the same modelling. The Doppler of the structures should not be taken into account.

- The model used for the fission products has a major impact on the k-effective burn-up evolution. The simplified models based on the ^{92}Mo cross-sections lead to much lower reactivity swing compared to more realistic models based on detailed description of the fission products or on lumped fission products.

- Different values of delayed neutron fraction ν_D per isotope used by the participants are primarily responsible for variations in the effective delayed neutron fraction calculated.

As a consequence, differences in the nuclear data libraries employed can explain a large part of the discrepancies obtained. The remaining part of the differences is explained by the different computation methodologies, cell modelling, treatment of fission products, and the neutron energy group structure employed by the participants. Some remaining inconsistencies could not be investigated within the framework of this benchmark and still need to be understood, in particular the lower Doppler coefficient, sodium void worth, and control rods worth estimated by UIUC, and the higher power in the centre of the CAR-3600 estimated at CER-EK. Even though the discrepancy of UIUC is still under investigation, the comparison was conducted including all results.

Discrepancies between "best estimate" deterministic and Monte-Carlo results need to be investigated in depth in order to identify remaining bias. Beyond this important task, the detailed review of modelling effects that can be found in the present report paves the way for important recommendations on general neutronic schemes to be adopted for accurate reactivity effect (feedback coefficients) evaluation using deterministic codes:

- heterogeneous spatial description of subassembly for cross-section generation;

- fine-group (few thousand group) energy description for self-shielding effects;

- specific treatment in order to take into account spatial self-shielding effect on control rod cross-section (labelled as "heterogeneity correction" in previous chapters).

Despite apparent discrepancies on BOC and EOC k-effective, calculating feedback coefficients and kinetic constants for performing transient analyses look rather satisfactory for the four investigated cores and anticipate limited bias on transient studies for these cores.

For all cores, uncertainties on reactivity feedback coefficients should be evaluated and possibly checked against integral experiments. Uncertainties evaluations are being performed within the LWR-UAM "Uncertainty Analysis in Modeling" up to and including the transient analysis and such evaluation should also be launched for the SFR.

References

[1] NEA (2011), *Sodium Fast Reactor Core Definition*, Version 1.2. (https://www.oecd-nea.org/science/wprs/sfr-taskforce/WPRS-AEN-SFR-Cores-V1.2.pdf).

[2] P. Sciora et al. (2009), "A break even oxide fuel core for an innovative French sodium-cooled fast reactor: Neutronic studies results", *Proceedings of Global*, 9528, Paris, France.

[3] F. Varaine et al. (2009), "Comparative review on different fuels for GEN IV sodium fast reactors: Merits and drawbacks", *Proceedings of FR'09*, Kyoto, Japan.

[4] T.K. Kim, W.S. Yang, C. Grandy, R.N. Hill (2009), "Core design studies for a 1000 MWth advanced burner reactor", *Annals of Nuclear Energy*.

[5] N.E. Stauff et al. (2013), "Evaluation of sodium-cooled fast reactor neutronic benchmarks", *Proceedings of FR'13*, paper CN-199-254, Paris, France.

[6] Y.K. Lee, E. Brun (2013), "Investigation of nuclear data libraries with TRIPOLI-4 Monte Carlo Code for sodium-cooled fast reactors", *International Conference on Nuclear Data for Science and Technology*, (ND2013), New York, US.

[7] A. Koning et al. (2006), "The JEFF-3.1 Nuclear Data Library", Nuclear Energy Agency Data Bank, *JEFF Report 21*.

[8] M.B. Chadwick et al. (2006), "ENDF/B-VII.0: Next Generation Evaluated Nuclear Data Library for Nuclear Science and Technology", *Nuclear Data Sheets*.

[9] M.B. Chadwick et al. (2011), "ENDF/B-VII.1 Nuclear Data for Science and Technology: Cross Sections, Covariances, Fission Product Yields and Decay data", *Nuclear Data Sheets*.

[10] CSEWG-Collaboration (2001), "Evaluated Nuclear Data File ENDF/B-VI.8." www.nndc.bnl.gov/endf.

[11] K. Shibata et al. (2011), "JENDL-4.0: A new library for nuclear science and engineering", *Journal of Nuclear Science and Technology*, Vol. 48, No. 1, pp.1-30.

[12] G. Rimpault et al. (2002), "The ERANOS code and data system for fast reactor neutronic analyses", *Proceedings of PHYSOR 2002*, Seoul, Korea.

[13] J. Leppanen (2012), "Serpent: A Continuous-energy Monte Carlo Reactor Physics Burn-up Calculation Code", User's Manual, VTT Technical Research Centre of Finland, Espoo, Finland.

[14] TRIPOLI-4 Project Team (2013), "TRIPOLI-4 Version 8 User Guide", Report CEA-R-6169 (2008), CEA-R-6316 (2013), Commissariat à l'Energie Atomique et aux Energies Alternatives.

[15] C.H. Lee, W.S. Yang (2011), "MC2-3: Multi-group Cross Section Generation Code for Fast Reactor Analysis", ANL/ NE-11-41.

[16] B.J. Toppel (1983), *A User's Guide for the REBUS-3 Fuel Cycle Analysis Capability*, ANL-83-2.

[17] M.A. Smith, W.S. Yang, A. Mohamed, E.E. Lewis (2012), "Perturbation and sensitivity tool based on the VARIANT option of DIF3D", *American Nuclear Society Transactions 107*, San Diego, US.

[18] Monte Carlo Code Group, LANL, MCNP5 online documentation.

[19] I. Pataki, A. Kereszturi (2013), "Development and verification of new nodal methods in the KIKO3DMG code", *Proceedings of the 23nd AER Symposium*, Strbske Pleso, Slovakia.

[20] A. Stankovskiy, G. Van Den Eynde (2012), "Advanced method for calculations of core burn-up, activation of structural materials, and spallation products accumulation in accelerator-driven systems", *Science and Technology of Nuclear Installations*.

[21] W. Bernnat, M. Mattes, N. Guilliard, J. Lapins, W. Zwermann, I. Pasichnyk, K. Velkov (2013), "Monte Carlo neutronics and thermal hydraulics analysis of reactor cores with multilevel grids", *Joint International Conference on Supercomputing in Nuclear Applications and Monte Carlo*, Paris, France.

[22] K. Yokoyama, T. Hazama, K. Numata, T. Jin (2013), "Development of comprehensive and versatile framework for reactor analysis, MARBLE", *Annals of Nuclear Energy*.

[23] Y. Nagaya, K. Okumura, T. Mori, M. Nakagawa (2005), *MVP/GMVP II: General Purpose Monte Carlo Codes for Neutron and Photon Transport Calculations based on Continuous Energy and Multi-group Methods,* JAERI 1348, Japan Atomic Energy Research Institute, Japan.

[24] C.H.M. Broeders, R. Dagan, V. Sanchez, A. Travleev (2004), "KAPROS-E: Modular program system for nuclear reactor analysis, status and results of selected applications", Jahrestagung Kerntechnik, http://inrwww.webarchiv.kit.edu/, Düsseldorf, Germany.

[25] M. Carta, G. Granget, G. Palmioti, M. Salvatores, R. Soule (1988), "Control rod heterogeneity effects in liquid-metal fast breeder reactors: Method developments and experimental validation", *Nuclear Science and Engineering*.

Appendix A. List of participants and calculation methodologies

1. ANL, US
 Participants: N. E. Stauff, T.K. Kim, T. A. Taiwo
 Basic Library: ENDL/B-VII.0 and JEFF-3.1
 Lattice calculation: MC^2-3, and ECCO
 Core Calculation: DIF3D/REBUS, ERANOS, and MCNP5

2. CEA, Cadarache, France
 Participants: L. Buiron, G. Rimpault
 Basic Library: JEFF-3.1, ENDL/B-VII.0, ENDL/B-VI.8, and JENDL-4.0
 Lattice calculation: ECCO
 Core Calculation: ERANOS

3. CEA, Saclay, France
 Participants: E. Brun, Y.K. Lee
 Basic Library: JEFF-3.1.1
 Lattice calculation:
 Core Calculation: TRIPOLI-4.0

4. CER-EK, Hungary
 Participants: I. Pataki, A. Kereszturi, A. Tota
 Basic Library: JEFF-3.1
 Lattice calculation: ECCO
 Core Calculation: KIKO3DMG

5. ENEA, Italy
 Participants: C. Parisi
 Basic Library: ENDF/B-VII.0
 Lattice calculation:
 Core Calculation: MCNPX

6. HZDR, Germany
 Participants: E. Fridman
 Basic Library: ENDF/B-VII.0
 Lattice calculation:
 Core Calculation: SERPENT

7. IKE, Germany

Participants: N. Guilliard
Basic Library: JEFF-3.1
Lattice calculation:
Core Calculation: MCNP5

8. JAEA, Japan

Participants: T. Kugo, K. Sugino, M.M. Uematsu
Basic Library: JENDL-4.0
Lattice calculation: MARBLE (SLAROM-UF)
Core Calculation: MARBLE (TRITAC), MVP

9. KIT, Germany

Participants: A. Ponomarev
Basic Library: JEFF-3.1.1
Lattice calculation: KANEXT
Core Calculation: KANEXT

10. SCK•CEN, Belgium

Participants: N. Messaoudi
Basic Library: JEFF-3.1.2 and ENDF/B-VII.1
Lattice calculation:
Core Calculation: MCNPX/ALEPH-2.5

11. UIUC, US

Participants: R. Lin Tan, T. Kozlowski
Basic Library: JEFF-3.1.1, ENDF/B-VI.8 and ENDF/B-VII.0
Lattice calculation:
Core Calculation: SERPENT

Table A.1. Core calculation methodologies

	Core Code	Lattice geometry	Core geometry	Approximation	Rod Heterogeneous Correction	Depletion chain
ANL-1	VARIANT11	Homogeneous	Homogeneous	Transport SP3	No	Mo
ANL-2	MCNP5	Homogeneous	Homogeneous	Monte Carlo	No	
ANL-3	MCNP5	Homogeneous	Homogeneous	Monte Carlo	No	
ANL-4	ERANOS VARIANT8	Homogeneous	Homogeneous	Transport SP3	No	Mo
ANL-5	ERANOS VARIANT8	Homogeneous	Homogeneous	Transport SP3	No	Mo
CEA-1	ERANOS VARIANT8	Heterogeneous	Homogeneous	Transport SP3	Yes	pseudo FP
CEA-2	ERANOS VARIANT8	Homogeneous	Homogeneous	Transport SP3	Yes	pseudo FP
CEA-3	ERANOS VARIANT8	Heterogeneous	Homogeneous	Transport SP3	No	pseudo FP
CEA-4	ERANOS VARIANT8	Homogeneous	Homogeneous	Transport SP3	No	pseudo FP
CEA-5	ERANOS VARIANT8	Homogeneous	Homogeneous	Transport SP3	No	pseudo FP
CEA-6	ERANOS VARIANT8	Homogeneous	Homogeneous	Transport SP3	No	Mo
CEA-7	ERANOS VARIANT8	Homogeneous	Homogeneous	Transport SP3	No	^{92}Mo
CEA-8	ERANOS VARIANT8	Homogeneous	Homogeneous	Transport SP3	No	pseudo FP
CEA-9	ERANOS VARIANT8	Homogeneous	Homogeneous	Transport SP3	No	^{92}Mo
CEA-10	TRIPOLI-4	Heterogeneous MC	Heterogeneous	Monte Carlo	Yes	Detailed
CER-EK	KIKO3DMG	Homogeneous	Homogeneous	Transport/ Diffusion (Lattice / Core)	No	^{92}Mo
ENEA	MCNPX	Heterogeneous MC	Heterogeneous	Monte Carlo	Yes	
HZDR	SERPENT	Heterogeneous MC	Heterogeneous	Monte Carlo	Yes	
JAEA-1	MARBLE (TRITAC)	Homogeneous	Homogeneous	Diffusion (Transport Correction)	No	
JAEA-2	MARBLE (TRITAC)	Heterogeneous	Homogeneous	Diffusion (Transport Correction)	Yes	
JAEA-3	MVP	Heterogeneous MC	Heterogeneous	Monte Carlo	Yes	
JAEA-4	MARBLE (CITATION)	Heterogeneous	Homogeneous	Diffusion	Yes	
JAEA-5	MVP/Diffusion for depletion calculation	Heterogeneous MC	Heterogeneous	Monte Carlo	Yes	Lumped FP
KIT	KANEXT	Homogeneous	Homogeneous	Transport SP3	No	
SCK•CEN-1	MCNPX/ALEPH-2.5	Heterogeneous MC	Heterogeneous	Monte Carlo	Yes	Detailed
SCK•CEN-2	MCNPX/ALEPH-2.5	Heterogeneous MC	Heterogeneous	Monte Carlo	Yes	Detailed
UIUC-1	SERPENT	Heterogeneous MC	Heterogeneous	Monte Carlo	Yes	
UIUC-2	SERPENT	Heterogeneous MC	Heterogeneous	Monte Carlo	Yes	
UIUC-3	SERPENT	Heterogeneous MC	Heterogeneous	Monte Carlo	Yes	
IKE-1	MCNP5	Heterogeneous MC	Heterogeneous	Monte Carlo	Yes	
IKE-2	MCNP5	Homogeneous	Homogeneous	Monte Carlo	No	

Table A.2. Lattice calculation methodologies

	Library	Lattice code	Rod heterogeneous correction	Fuel S/A	Subcritical S/A	CR S/A
ANL-1	ENDFB7.0	MC^2-3	No	RZ model of the core, 2082g-33g	RZ model of the core, 2082g-33g	RZ model of the core, 2082g-33g
ANL-2	ENDFB7.0		No	Homogeneous	Homogeneous	Homogeneous
ANL-3	JEFF3.1		No	Homogeneous	Homogeneous	Homogeneous
ANL-4	ENDFB7.0	ECCO	No	Homogeneous, Bsearch, 1968g-33g	Homogeneous, src calc 33g-33g	Homogeneous, src calc 33g-33g
ANL-5	JEFF3.1	ECCO	No	Homogeneous, Bsearch, 1968g-33g	Homogeneous, src calc 33g-33g	Homogeneous, src calc 33g-33g
CEA-1	JEFF3.1	ECCO	Yes	2D Hexagonal, Bsearch, 1968g-33g	Homogeneous, src calc 33g-33g	XY Heterogeneous, Equivalence method, 33g-33g
CEA-2	JEFF3.1	ECCO	Yes	Homogeneous, Bsearch, 33g-33g	Homogeneous, src calc 33g-33g	XY Heterogeneous, Equivalence method, 33g-33g
CEA-3	JEFF3.1	ECCO	No	2D Hexagonal, Bsearch, 33g-33g	Homogeneous, src calc 33g-33g	XY Heterogeneous, Equivalence method, 33g-33g
CEA-4	JEFF3.1	ECCO	No	Homogeneous, Bsearch, 1968g-33g	Homogeneous, src calc 33g-33g	XY Hete, Equivalence method, 33g-33g
CEA-5	JEFF3.1	ECCO	No	Homogeneous, Bsearch, 33g-33g	Homogeneous, src calc 33g-33g	Homogeneous, src calc 33g-33g
CEA-6	ENDFB6.8	ECCO	No	Homogeneous, Bsearch, 33g-33g	Homogeneous, src calc 33g-33g	Homogeneous, src calc 33g-33g
CEA-7	ENDFB7.0	ECCO	No	Homogeneous, Bsearch, 33g-33g	Homogeneous, src calc 33g-33g	Homogeneous, src calc 33g-33g
CEA-8	ENDFB7.1	ECCO	No	Homogeneous, Bsearch, 33g-33g	Homogeneous, src calc 33g-33g	Homogeneous, src calc 33g-33g
CEA-9	JENDL4.0	ECCO	No	Homogeneous, Bsearch, 33g-33g	Homogeneous, src calc 33g-33g	Homogeneous, src calc 33g-33g
CEA-10	JEFF3.1.1		Yes	Heterogeneous	Heterogeneous	Heterogeneous
CER	JEFF3.1	ECCO	No	2D Hexagonal, Bsearch, 1968g-9/17g	Homogeneous, src calc 1968g-9/17g	Homogeneous, src calc 1968g-9/17g
ENEA	ENDFB7.0		Yes	Heterogeneous	Heterogeneous	Heterogeneous
HZDR	ENDFB7.0		Yes	Heterogeneous	Heterogeneous	Heterogeneous
JAEA-1	JENDL4.0	MARBLE (SLAROM-UF)	No	Homogeneous, Bsearch, 70g-70g	Homogeneous, src calc, 70g-70g	Homogeneous, Equivalence method, 70g-70g
JAEA-2	JENDL4.0	MARBLE (SLAROM-UF)	Yes	Heterogeneous-1D multi-ring, Bsearch, 70g-70g	Homogeneous, src calc, 70g-70g	Heterogeneous Equivalence method, 70g-70g
JAEA-3	JENDL4.0		Yes	Heterogeneous	Heterogeneous	Heterogeneous
JAEA-4	JENDL4.0	MARBLE (SLAROM-UF)	Yes	Heterogeneous-1D multi-ring, search, 70g-70g	Homo, src calc, 70g-70g	Heterogeneous Equivalence method, 70g-70g
JAEA-5	JENDL4.0		Yes	Heterogeneous	Heterogeneous	Heterogeneous
KIT	JEFF3.1	KANEXT	Yes	Homogeneous, 350g-33g	Homogeneous	Homogeneous
SCK•CEN-1	ENDFB7.1		Yes	Heterogeneous	Heterogeneous	Heterogeneous
SCK•CEN-2	JEFF3.1.2		Yes	Heterogeneous	Heterogeneous	Heterogeneous
UIUC-1	JEFF3.1.1		Yes	Heterogeneous	Heterogeneous	Heterogeneous
UIUC-2	ENDFB6.8		Yes	Heterogeneous	Heterogeneous	Heterogeneous
UIUC-3	ENDFB7.0		Yes	Heterogeneous	Heterogeneous	Heterogeneous
IKE-1	JEFF3.1		Yes	Heterogeneous	Heterogeneous	Heterogeneous
IKE-2	JEFF3.1		No	Homo	Homo	Homo

Appendix B. Figures of the results

**Figure B.1. Effective multiplication factor comparison**
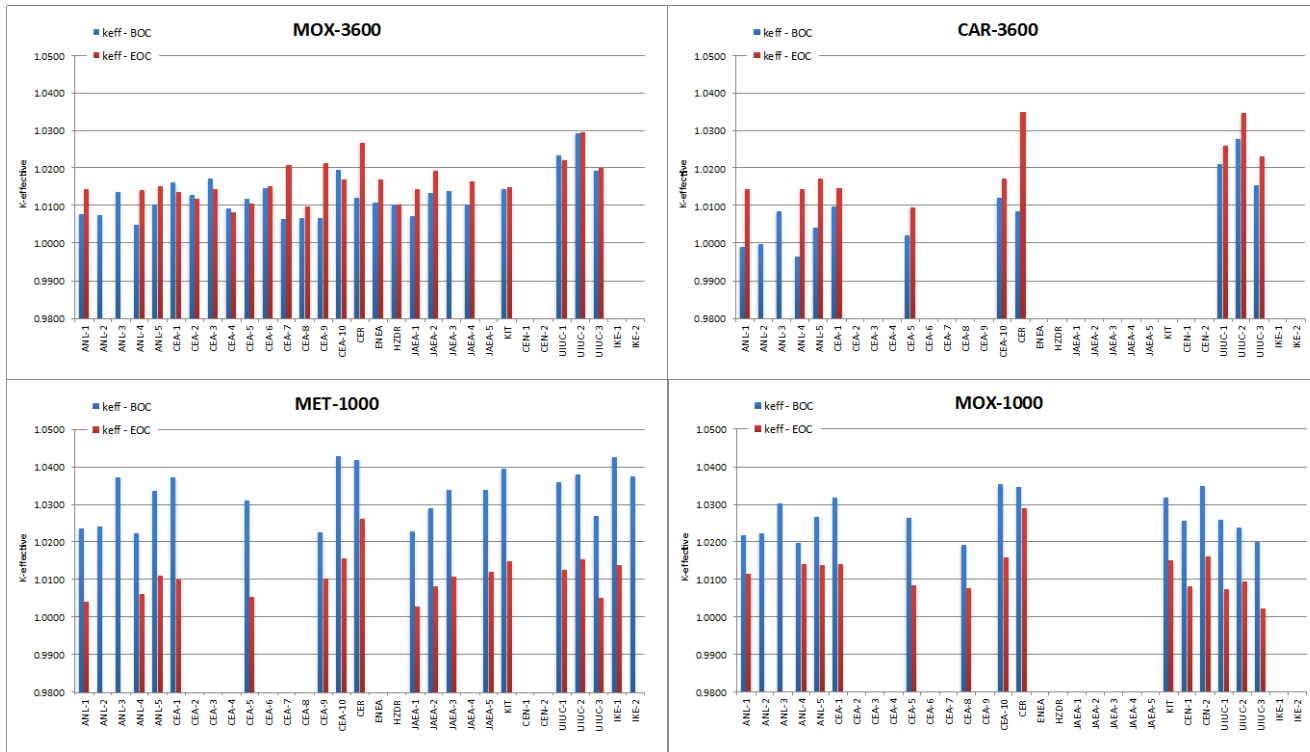
**Figure B.2. Effective delayed neutron fraction comparison**
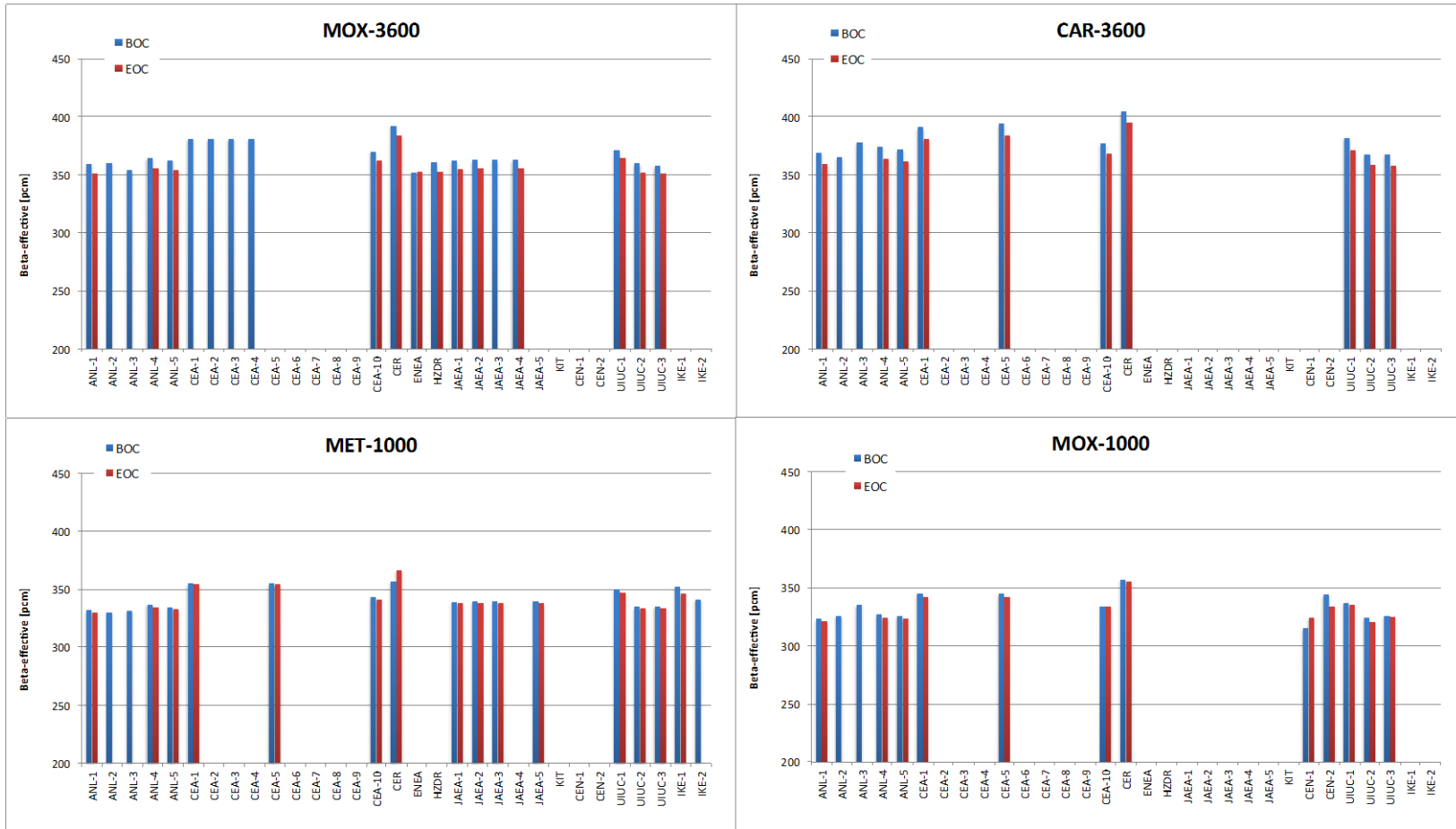
Figure B.3. Sodium void worth comparison
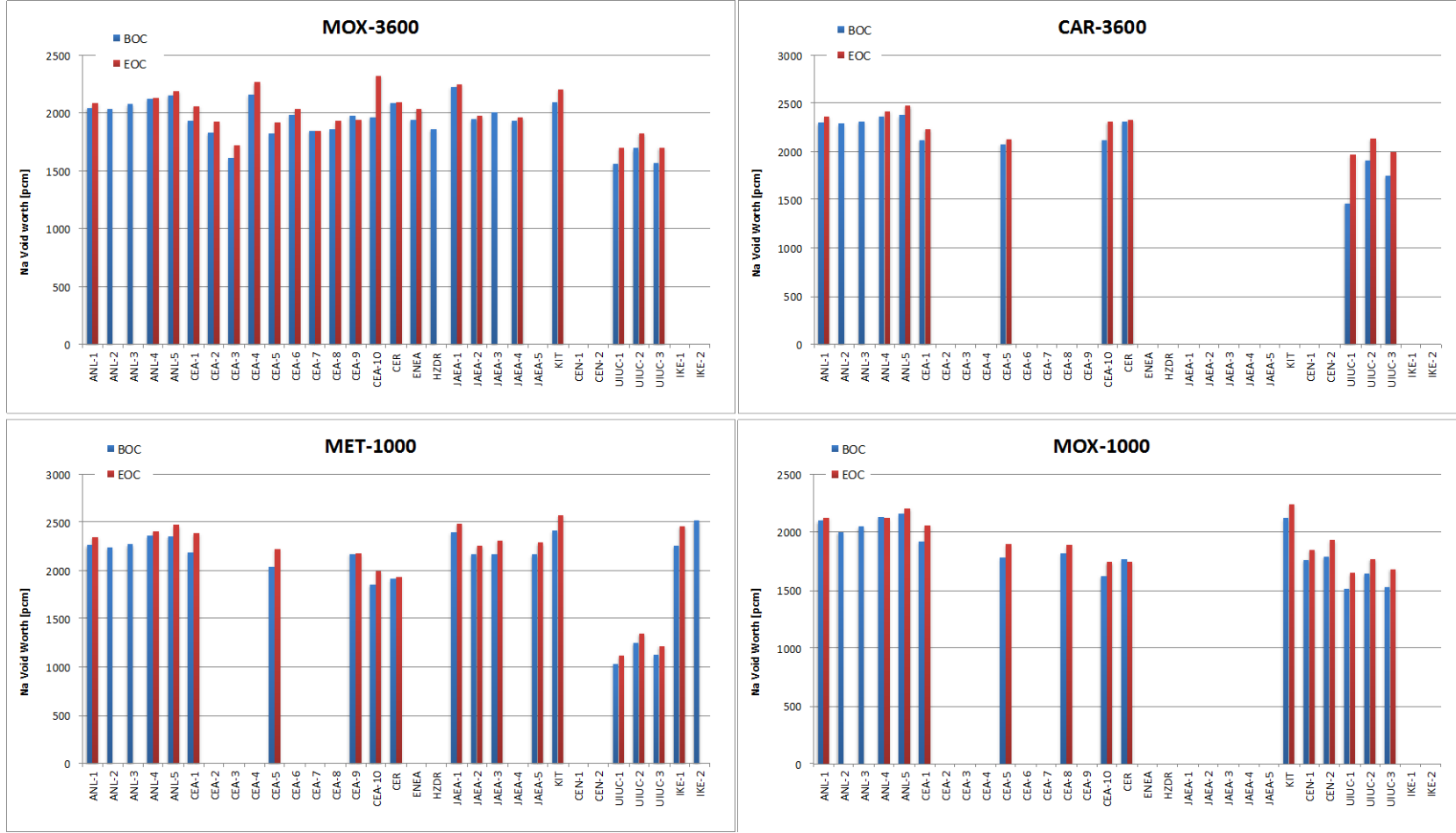
Figure B.4. Doppler coefficient comparison
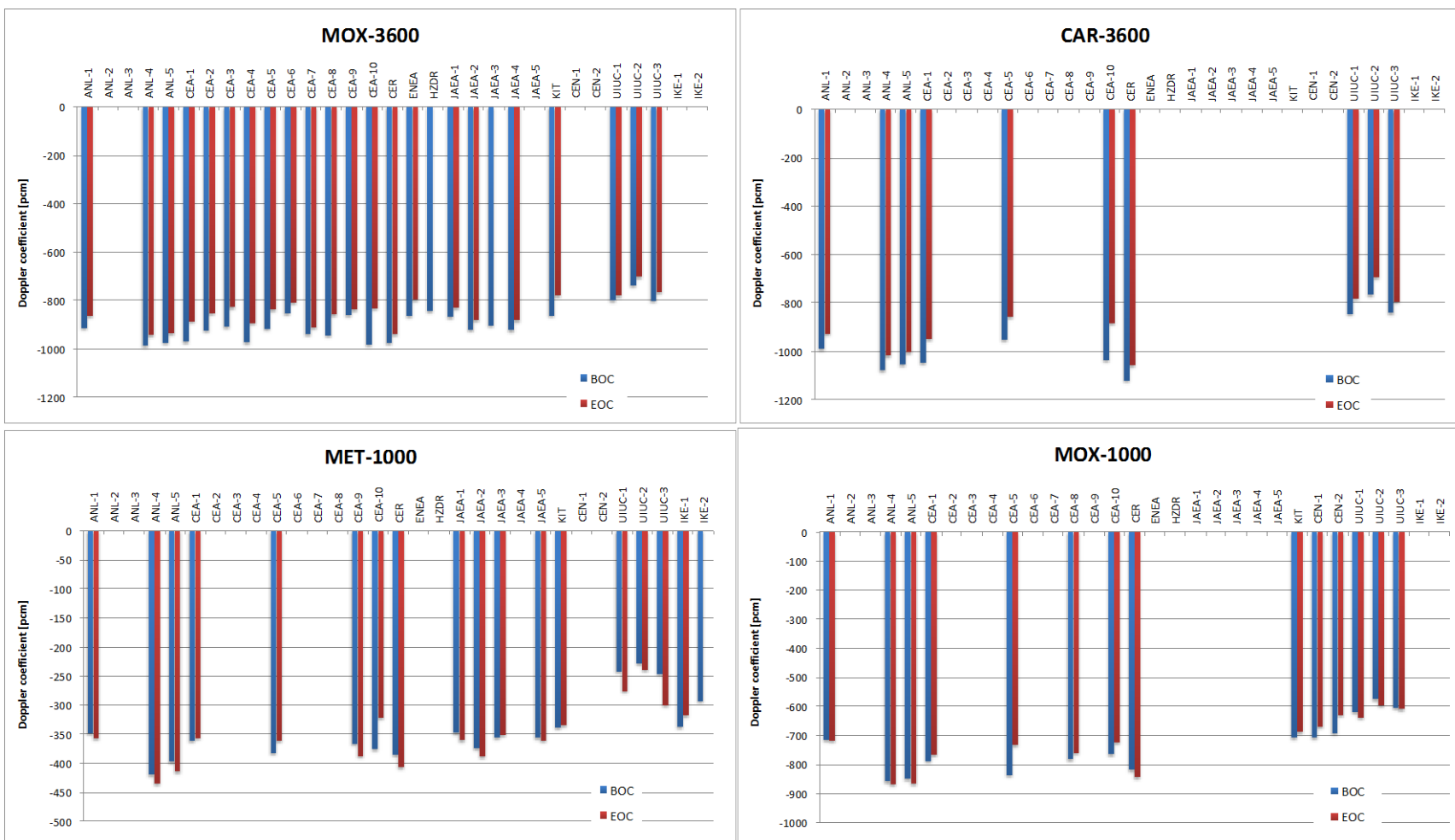
**Figure B.5. Nuclide masses comparison at EOC**
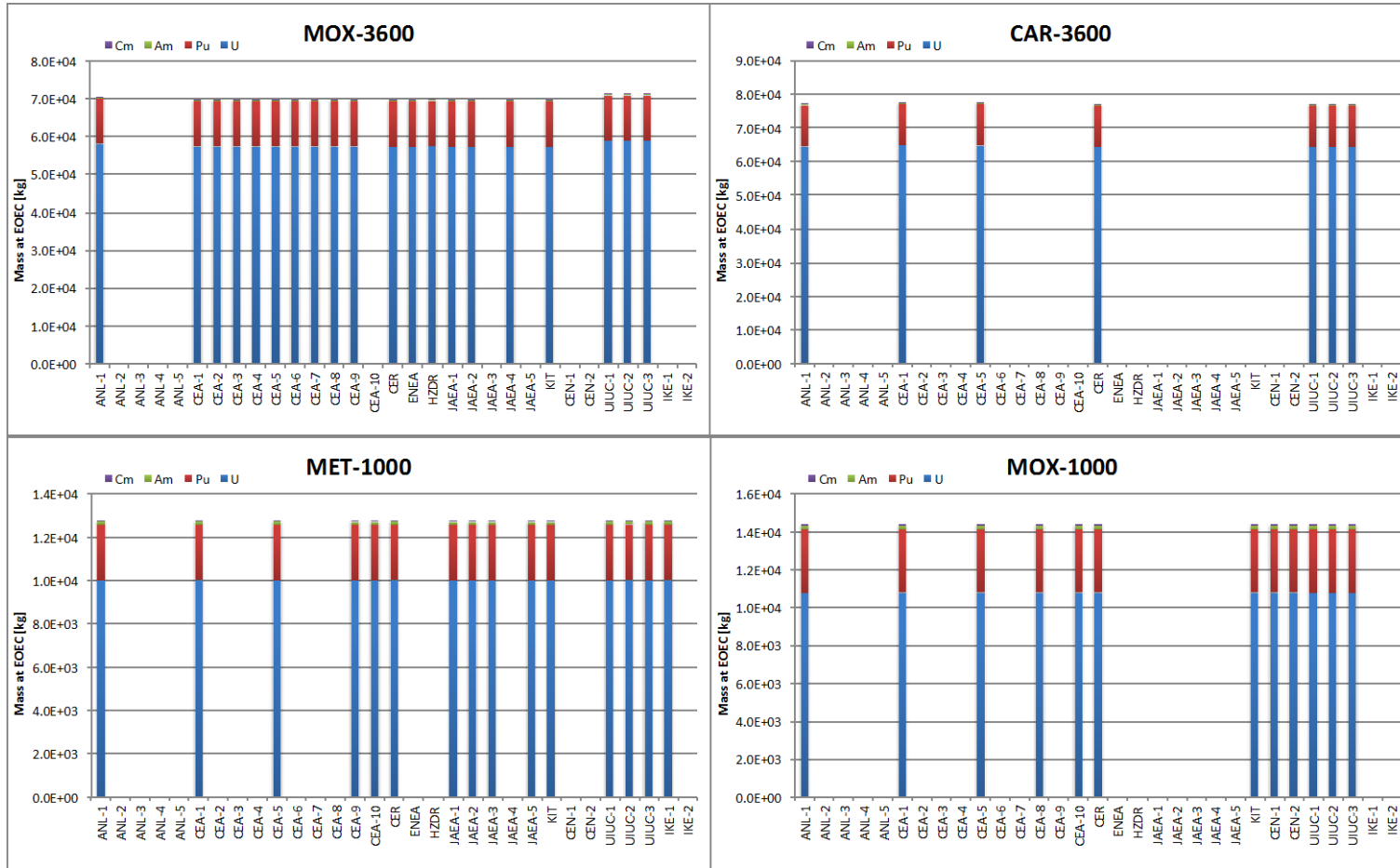
Figure B.6. Control rod worth comparison